Developing Spectral Diffusion as a Nonlinear Optical Measurement of Interfacial Water

By

Derek Glenn Osborne

A dissertation submitted in partial fulfillment
of the requirements for the degree of
Doctor of Philosophy
(Biophysics)
in the University of Michigan
2013

Dissertation Committee:

Associate Professor Kevin J. Kubarych
Professor Ari Gafni
Professor Eitan Geva
Associate Professor Jennifer P. Ogilvie
Professor Ayyalasamy Ramamoorthy
Assistant Professor Sarah L. Veatch

To Janel
The love of my life

Acknowledgments

The work of this dissertation could not have been completed without the help of numerous people during my time at the University of Michigan and though out my life.

With the guidance and kindness of Kevin Kubarych the work of this thesis was possible. Much of my understanding of science comes from his ability to understand a concept and then carefully explain it. Many past and present members of the Kubarych Group have been integral part of my research. Among those, Robert (Bobby) McCanne, Josef Dunbar, and Aaron White have played a particularly important role.

During my undergraduate education, it was Ryan Sargeant that helped me appreciate the beauty of science and the opportunities of research. If not for him, I would not have began my graduate studies.

My family has played an important role in my life. My parents, Kevin and Karen Osborne, always believed in my abilities no matter my production. Without the confidence they gave me, I do not know where I would be today. My brother Matt Osborne deserves particular thanks for demonstrating the power of curiosity.

Last of all, I must acknowledge my wonderful wife Janel. Through all of the challenges of my research, it was Janel that stood with me and encouraged me to always preserver.

Table of Contents

List of Figures

List of Tables

List of Abbreviations

ATR: attenuated total reflectance

1D: one dimensional

2D: two dimensional

2DIR: two dimensional infrared spectroscopy

B3LYP: Becke's three-parameter/ Lee Yang Parr

BCT: (Benzyl) chromium tricarbonyl

BBO: beta-barium borate

BP86: Becke 1989 /Perdew 1986 (functional)

CCD: charged coupled device

CLS: centerline slope

cdCMT: β-cyclodextrin cyclopentadienyl tricarbonyl

CMT: cyclopentadienyl manganese tricarbonyl

CORM: carbon monoxide releasing molecule

CORM-2: dichloro ruthenium(II) dimer

CPU: chirped pulse upconversion

chol-BCT: (cholesteryl benzoate) chromium tricarbonyl

cooh-BCT: (benzoic acid) chromium tricarbonyl

DFG: difference frequency generation

DFT: density functional theory

DHPC: 1,2-Dihexanoyl-*sn*-Glycero-3-Phosphocholine

DMDC: dimanganese decacarbonyl

DMPC: 1,2-Dimyristoyl-*sn*-Glycero-3-Phosphocholine

et-BCT: (ethyl benzoate) chromium tricarbonyl

FID: free induction decay

FT: Fourier transform

FTIR: Fourier transform infrared (spectroscopy)

FWHM: full-width at half maximum

HEWL: hen egg white lysozyme

IR: infrared

IVR: intramolecular vibrational redistribution

MD: molecular dynamics

NLS: nodal line slope

NOE: nuclear Overhauser effect

NMR: nuclear magnetic resonance

NPT: number of particles, pressure, temperature (conserved)

OD: optical density

ODNP: Overhauser effect dynamic nuclear polarization

OPA: optical parametric amplifier

PC: phosphatidylcholine

PG: phosphatidylglycerol

POPC: 1-palmitoyl-2-oleoyl-sn-glycero-3-phosphocholine

POPG: 1-palmitoyl-2-oleoyl-sn-glycero-3-phosphoglycerol

RASD: rapidly acquired spectral diffusion

PI-CORM: ([CO]Fe[$N_5C_{22}H_{21}$])

RDC: acetilacetonato rhodium dicarbonyl

UV: ultraviolet

VIS: visible

Chapter One

Introduction

1.1 Interfacial Water

The rates of chemical reactions in the aqueous phase are often influenced by the dynamics of the solvent surrounding the reactants making the study of solvent dynamics of particular interest[1]. For biological reactions and processes, the rates and dynamics of a reaction *in vitro* will differ from those *in vivo*[2-4] due to the cytosol of a living cell being crowded with biological macromolecules (*e.g.* proteins, lipid membranes, RNA, and fibrils) that account for more than 300 mg/ml[5]. Hydrated biological macromolecules induce a restructuring of water's hydrogen bonding network leading to lost hydrogen bonds as well as constraints on the dynamics of water at the interface of biological macromolecules[6]. Understanding the influence biomacromolecules have on the dynamics of interfacial water are therefore of an interest in biophysical research, but are difficult to measure experimentally[2], where one

requires both the capability of measuring subpicosecond dynamics and the ability to probe the interfacial water selectively.

In recent years, multiple experimental techniques have been developed to measure the dynamics at the biomacromolecule-water interface. Probing tryptophan residues, time resolved fluorescence up-conversion can site specifically measure the dynamics of interfacial water neighboring the tryptophan[7, 8]. NMR spectroscopy, using nuclear Overhauser effect (NOE), can measure the interfacial water of a protein encapsulated within reverse micelles[9], while the recently developed Overhauser effect dynamic nuclear polarization (ODNP) technique can be used to measure the dynamics of water within 1.5 nm of a nitroxide radical moiety bound to the lipid membrane[10]. Additionally, molecular dynamics simulations have been used to model the interfacial water of a lipid membrane, finding the choline lipid head groups and the interfacial water to form a "clathrate" shell[11]. Additionally, these studies found the choline head group to be as important as the phosphate group for absorbing water[12]. Vibrational spectroscopy is a promising experimental technique capable of measuring the subpicosecond dynamics of water due to its ultrafast capabilities and the inherent relationship between spectral dynamics and solvent dynamics (*vide infra*).

Vibrational spectroscopy has long been used to study the dynamics of bulk water by measuring the spectral diffusion of the OH and OD stretches of HOD in D_2O and H_2O respectively, which found the spectral diffusion time constant of OH and OD to be 1.6 and 1.1 ps respectively[13-15]. These spectral diffusion time constants are thought to represent the time scales of the hydrogen bond network reorganization for D_2O and

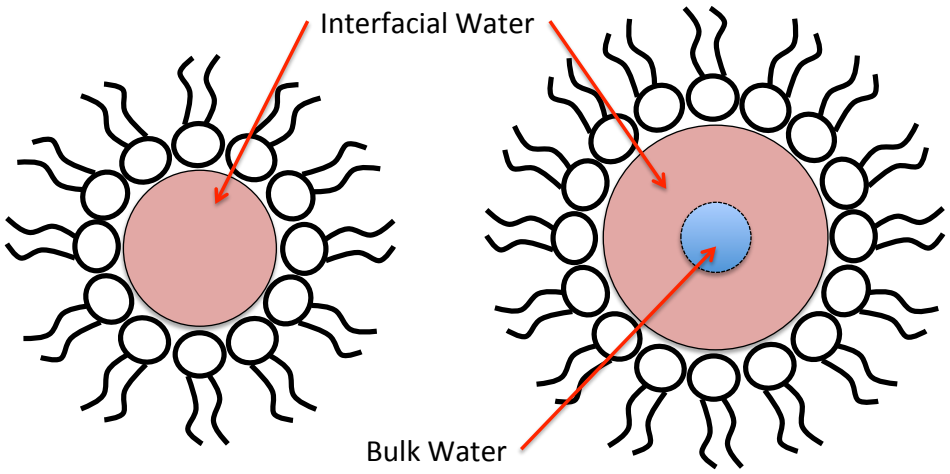

Figure 1.1. Using the OH stretch of water to study the dynamics of interfacial water requires the removal of the majority of bulk water, which can be accomplished through the use of reverse micelles.

H_2O. Although these methods are capable of studying the bulk dynamics of water, measuring the reorganization of the hydrogen bond network at the interface of a biological macromolecule requires an experiment capable of exclusively probing the interfacial water. One method of accomplishing this task is by eliminating the bulk altogether such as water confined in a reverse micelle.

A reverse micelle has three primary component parts – a nonpolar solvent and water separated by a surfactant (**Fig. 1.1**) – where the size of the micelle is determined by the ratio of surfactant to water. Generally, the size of the micelle is small enough, 1-6 nm in diameter, such that the majority of the water molecules encapsulated by the surfactant are at the interface of the surfactant. Both the Elsaesser and Fayer groups have taken this approach in studying the interfacial water dynamics of a membrane with ultrafast vibrational spectroscopy. The work of Costard *et al.* of the Elsaesser group found the vibrational lifetime of the OH stretch, which the authors attribute to the spectral diffusion of the OH stretch, is dependent on the size of the micelle[16]. Fenn *et al.*

of the Fayer group also studied the OH stretch of HOD in D_2O in reverse micelles, but rather than studying the lifetime, they directly measured the spectral diffusion through lineshape analysis of 2DIR spectra[17-19]. Similar to the findings of Costard, as micelle size increased, the spectral diffusion accelerated. These findings suggest that as the size of micelle decreases, the hydrogen bond network of the interfacial water spans the length of the of the micelle.

1.2 Site Specific Labeling

An alternative to eliminating the bulk water is to site specifically label the interface of a biological macromolecule with a vibrational probe sensitive to the dynamics of water. The phosphate group is capable of probing the dynamics of the interfacial water[20], but is located in a cluttered region of the spectrum. Metal carbonyls are excellent vibrational labels due to their exceptionally large transition dipole moment that is located in a relatively uncluttered region of the spectrum (~2000 cm^{-1}) and their high sensitivity to solvent fluctuations. King and Kubarych labeled the interface of hen egg white lysozyme (HEWL) with the ruthenium dicarbonyl at the structured α-domain[21, 22]. These studies first measured the spectral diffusion time constant of CORM-2 and PI-CORM ($[CO]Fe[N_5C_{22}H_{21}]$)[21] in bulk D_2O (denoted CORM due to their carbon monoxide releasing abilities) and found the spectral diffusion time constants to be nearly identical to the spectral diffusion time constant of the OH stretch of HOD in D_2O, 1.5 ± 0.3 ps and 1.6 ± 0.4 ps respectively indicating that the spectral diffusion of a metal carbonyl is a direct measure of the hydrogen bond network restructuring. The spectral

diffusion time constant of the ruthenium dicarbonyl coordinated at the interface of HEWL, in comparison, is roughly a factor of two slower, 2.7 ± 0.4 ps, indicating that constraining effects of HEWL slow the dynamics of the interfacial water. Additionally, the authors measured the spectral diffusion of coordinated ruthenium dicarbonyl in a series of glycerol mixtures (0-80%) and found that despite a 100 fold increase in viscosity, the spectral diffusion of the interfacial water only exhibits a three fold slow down, which suggests a weak coupling between the hydration water and the bulk solution.

Although the work of King and Kubarych demonstrate that ruthenium dicarbonyl adequately probes the ultrafast dynamics of the interfacial water of HEWL, the utility of ruthenium dicarbonyl as an interfacial probe is limited to proteins with a surface histidine. In chapter four of this thesis we demonstrate how the interfacial water of a lipid membrane can be probed with a metal carbonyl label. We accomplish this by first synthesizing the novel probe, (cholesteryl benzoate) chromium tricarbonyl (chol-BCT), through the use of a simple esterification with hydroxyl group of cholesterol, which we subsequently embed into a lipid bilayer. A full characterization of chol-BCT and its orientation can be found in chapter four. Additionally, we find this esterification to be capable of labeling multiple biologically relevant hydroxyl groups suggesting that it may be used as a universal labeling method.

1.3 Nanoconfinement

In chapter five, we directly test how confinement alters the spectral diffusion

time constant with the model system of cyclopentadienyl manganese tricarbonyl (CMT) motif confined in the simple β-cyclodextrin ring. Measuring the spectral diffusion time constant in a series linear alcohols, we found the spectral diffusion of confined CMT always to be faster than that of CMT in neat alcohol, which was surprising because molecular dynamics (MD) simulations of β-cyclodextrin in methanol measured the reorientation correlation function near β-cyclodextrin to decay slower than that of neat methanol. We propose that the faster spectral diffusion time constants of CMT complexed with β-cyclodextrin arise from the β-cyclodextrin excluding solvent molecules, which in turn reduces the size of the conformational space. To test the dependence of the spectral diffusion time constant on the number of solvating alcohol molecules, we compared the spectral time constants of CMT and CMT in β-cyclodextrin to dimanganese decacarbonyl (DMDC) and implemented a simple Monte Carlo simulation finding that both tests support the hypothesis that the spectral diffusion time constant is dependent on the size of the conformational space. Because the size of the conformational space is related to entropy, it is possible that the spectral diffusion time constant could be related to the entropy of its surroundings but further work is required to make this connection rigorous. It is not uncommon to relate conformational dynamics to the conformational entropy. For biological macromolecules, the NMR relaxation constant is related to the interaction vector autocorrelation function through the Lipari and Szabo model-free formalism, which then can be related to the conformational entropy.

1.4 Accelerated Data Acquisition

If the spectral diffusion time constant were to be used to measure dynamics as a function of thermodynamic properties, it would be advantageous to rapidly measure the spectral diffusion so that a series of measurement can be made scanning a single variable (*e.g.* temperature) while holding all other variables constant. Currently, the most accurate method of measuring spectral diffusion is with two-dimensional infrared (2DIR) spectroscopy. Although 2DIR is a powerful spectroscopic technique, 2DIR requires measurements along two spectroscopic dimensions making data acquisition time consuming. In the Kubarych group data acquisition and processing of a single spectral diffusion measurement requires ~3 hrs, while others in the field require multiple days to acquire a single spectral diffusion measurement. In chapter two we demonstrate how the pulse sequence of 2DIR can be altered to rapidly acquire the spectral diffusion (RASD) and process the data in less than 3 min. A full tutorial of how to use RASD in the laboratory can be found in chapter seven. In chapter six we demonstrate the ability of RASD by measuring the internal rotation of BCT and find that the internal rotation does not have a solvent dependence. Although RASD is capable of accelerating the data acquisition time, it also loses the ability to measure other physical phenomena such as intramolecular vibrational redistribution (IVR) and chemical exchange. In chapter three, we demonstrate how compressed sensing (CS) is capable of reducing the data acquisition time while maintaining the ability to measure all of the experimental observables of a 2DIR spectrum including IVR and chemical exchange.

In summary, this thesis describes in detail the methods needed to site specifically measure the dynamics of the interface between a biological macromolecule and its hydration water. Chapters two and three describe novel spectroscopic techniques to accelerate the data acquisition time while in Chapter four, we demonstrate how a simple esterification can be used to label the membrane-water interface of a lipid bilayer. In chapter five we explore how the spectral diffusion time constant is potentially related to entropy. Lastly, chapter six is an implementation of the RASD technique and chapter seven is a tutorial of how RASD is implemented in the Kubarych group.

1.5 Vibrational Spectroscopy

Vibrational spectroscopy has proven to be a powerful tool in the study of biological phenomena. A simple linear FTIR spectrum of a chromophore in the condensed phase can offer insightful information on the environment experienced by the chromophore. For instance, the analysis of the spectral width can measure the distribution of the chromophore's local environments[23, 24] while the location of the peak can be a measure of the magnitude of the electric field at the chromophore[25, 26]. Adding complexity to a linear vibrational spectroscopy can help extract additional information from a chromophore; the measure of polarized attenuated total reflectance (ATR) is used to determine the orientation of a peptide at the surface of a lipid[27, 28], adding an ultraviolet pulse allows measurements of the bonding at a protein's active site[29-31], and chemical triggering a protein reaction with a denaturant can probe its structural changes

Similar to NMR spectroscopy, the introduction of multiple interactions to

vibrational spectroscopic techniques correlates frequencies over spectral dimensions[32]. Specific to vibrational spectroscopy, multiple dimensional vibrational spectroscopy is used in experiments such as chemical exchange[33-36], intramolecular vibrational energy redistribution (IVR)[37], and spectral diffusion[13, 38]. The work presented in this thesis focuses on the use of spectral diffusion and in the remainder of this chapter, I will give an overview of the theoretical and historical developments of spectral diffusion.

1.6 Spectral Diffusion

Vibrational modes have finite spectral widths that arise from homogeneous and inhomogeneous broadening. All chromophores experience some amount of homogeneous broadening that arises from the Fourier transform limit of the chromophore's free induction decay (FID) whose dephasing arises from the random phase kicks of the environment. Generally, the variance in homogeneous width of a given vibrational mode from solvent to solvent is small. Conversely, a chromophore only experiences inhomogeneous broadening when exposed to a multiplicity of complex environments. Therefore, not all spectral widths exhibit inhomogeneous broadening and those that do are highly dependent on the solvent.

Consider an ensemble of chromophores in the condensed phase; at any given moment this ensemble will have a distribution of transition frequencies due to differences in their local microenvironments. As these microenvironments fluctuate due to the dynamics of their surroundings, the transition frequency will also fluctuate. If the microenvironment fluctuations are much slower than the homogeneous dephasing time,

the line shape will simply represent the distribution of microenvironments available to the ensemble of chromophores. At the other limit, where the microenvironment fluctuations are much faster than the homogeneous dephasing such that all chromophores experience all of the microenvironments available within homogeneous dephasing time, the spectral width will be "motionally narrowed" and will only exhibit homogeneous broadening in the linear spectrum. This process of the transition frequency diffusing with the fluctuations of the surrounding solvent molecules is known as spectral diffusion, and its inherent correlation to dynamics of the solvents allows spectral information to report on solvent dynamics.

Consider the O-H stretch of water as an example; because the frequency of a hydrogen bonded water molecule will be red-shifted relative to a water molecule lacking a hydrogen bond, the O-H stretch is inhomogeneously broadened. Because each water molecule is continuously breaking and forming hydrogen bonds with its neighbors, the instantaneous frequency will constantly fluctuate, leading to spectral diffusion.

Spectral diffusion is quantified through the normalized frequency-frequency correlation function (FFCF):

$$\bar{C}(t) = \langle \delta\omega(0)\delta\omega(t)\rangle / \langle \delta\omega^2 \rangle \qquad (1)$$

Where $\delta\omega(t)$ are the frequency's fluctuations from the average, $\delta\omega(t) = \omega(t) - \langle\omega\rangle$, and because $\bar{C}(t)$ is normalized, it will range from 1 to -1 and is unitless. A sum of exponentials is often used to describe the FFCF giving the form[21, 39, 40]:

$$\bar{C}(t) = \frac{\delta(t)}{T_2} + \sum_i \Delta_i^2 e^{-t/\tau_i} \quad (2)$$

Where T_2 represents the pure homogeneous dephasing time, Δ_i^2 is the amplitude of the frequency fluctuations, τ_i is the spectral diffusion time constant, and the delta function represents the motional narrowing. In the work presented here, it is often the spectral diffusion time constant, τ_i, that is of highest interest because it reflects the dynamics of the solvent.

1.7 Measuring Spectral Diffusion

1.7.1 Spectral hole burning. Utilizing a chromophore's transition dipole moment's ability to diffuse due to its fluctuating microenvironment has long been a tool in measuring the solvent dynamics with spectral hole burning experiments[41]. Because of the role that water dynamics play in many biological reactions, one system of particular interest is the OH stretch of water. Water has an exceptionally broad width of 235 cm^{-1} at the full width half maximum (FWHM) and is centered at 3400 cm^{-1}. More than 20 years ago, Graener *et al.* used spectral hole burning to measure the spectral dynamics of water by first burning a hole in the OH width with a narrow bandwidth, ~20 cm^{-1} FWHM and 11 ps in duration, and then probing with a second broad band pulse delayed by t_D. By measuring the peak shape of the probe as a function of t_d, the OH spectral dynamics were measured on the picosecond time scale[42]. Because the pump pulse requires a spectrally narrow bandwidth, and is therefore long in duration, the time scales that the spectral hole burning experiment is capable of measuring is limited by the inverse of the pump linewidth, which is narrower than the inhomogeneous

width of the transition frequency.Four wave-mixing techniques and their use of sub-picosecond pulses allowed for the measurement of spectral diffusion with sub-picosecond resolution.

1.7.2 Four wave-mixing techniques. Multiple third order experiments are capable of measuring the spectral diffusion of a chromophore, all of which require interaction with three infrared pulses E_1, E_2, and E_3 separated by the three time delays t_1, t_2, and t_3 (**Fig. 1.2**). These fields induce a nonlinear polarization in the chromophore represented as:

$$P^{(3)}(t) = \int_{-\infty}^{\infty} dt_3 \int_{-\infty}^{\infty} dt_2 \int_{-\infty}^{\infty} dt_1 R^{(3)}(t_1, t_2, t_3) E(t)^3 \qquad (3)$$

Where $R^{(3)}$ represents the third order response function and E(t) the laser generated fields. Typically, infrared spectroscopy is modeled through the use of response functions that assumes the second-order cumulant approximation, where the bath potential surface is assumed to be harmonic, and under the short time approximation, a commonly used approximation in vibrational spectroscopy, where the dephasing times, t_1, t_3, are assumed to be short relative to the t_2 dependent correlation function. The laser generated pulses in the experiments of this manuscript are ~100 fs. Hence, it is common to invoke the impulsive limit, and take the signal to be proportional to the response function. The signal generated by the nonlinear polarization after interacting with the three fields is the experimentally observed measurement, $E_s(t_3)$, in all third order experiments. A large difference between the various third order experiments that measure spectral diffusion are the time delays t_1, t_2, and t_3 that are scanned during the experiment.

The chromophore begins every experiment in the ground state population, $\rho_{0,0}$,

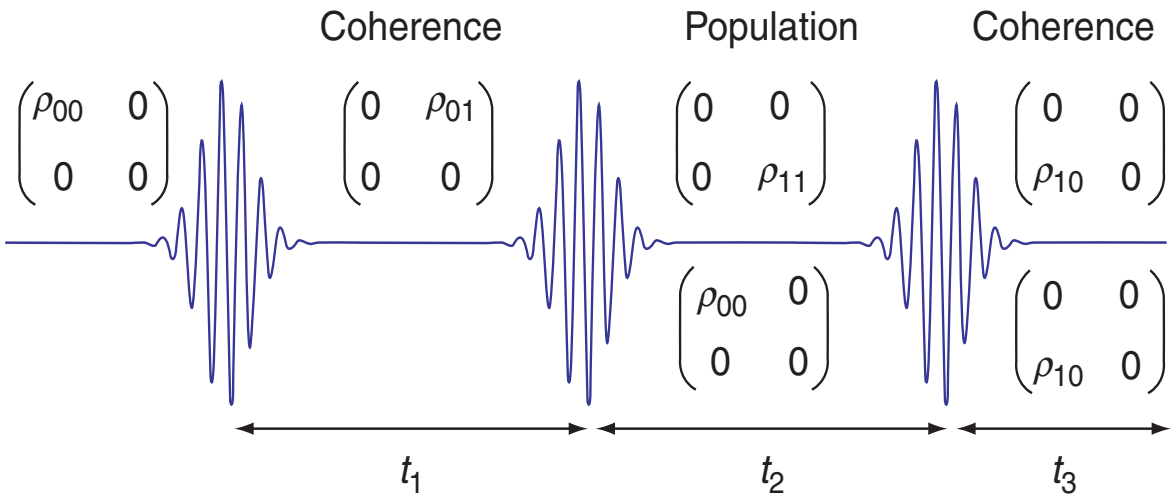

Figure 1.2 The experiment consists of three fields that are separated by the time delays t_1, t_2, and t_3. Beginning in the ground $\rho_{0,0}$, and will alternate between a coherence and population after each interaction with a field (J. Olgilvie and K. Kubarych 2009).

and each interaction with a field will cause the chromophore to evolve alternatively between a coherence, $\rho_{i,j}$, and a population, $\rho_{i,I}$ (**Fig 1.2**)[43]. Assuming a two level system, four pathways are available to the chromophore that are separated into two possible phase matching conditions, rephasing ($\mathbf{k}_R = -\mathbf{k}_1 + \mathbf{k}_2 + \mathbf{k}_3$) and nonrephasing ($\mathbf{k}_N = \mathbf{k}_1 - \mathbf{k}_2 + \mathbf{k}_3$) (**Fig. 1.2**). For rephasing, the t_1 and t_3 coherences evolve with conjugate phases allowing the t_3 coherence to undo the dephasing acquired during t_1 (hence the name rephasing), while the nonrephasing coherences evolve with the same frequency which causes the t_3 coherence to increase the dephasing acquired during the t_1 coherence. The ability of the rephasing to reverse the dephasing will increase the magnitude of the rephasing signal relative to the nonrephasing signal when the vibrational mode is inhomogeneously broadened. This phenomena allows the difference between the rephasing and nonrephasing signal amplitude to be a measure of the inhomogeneous broadening. If the chromophore experiences spectral diffusion during t_2 it will lose its ability to rephase and therefore the t_2 dependence of the signal amplitude can be used

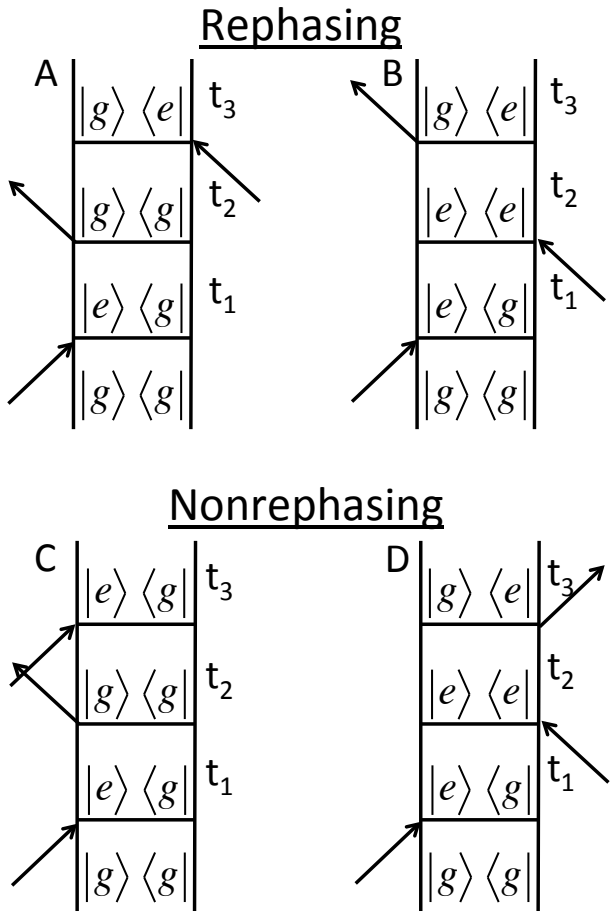

Figure 1.3 The double sided Feynman diagram representing the Louisville pathways available to a two level system. A and B represent the "rephasing" pathways while C and D represent the non rephasing pathways.

as a measure of spectral diffusion.

1.7.3 Stimulated photon echo. The inhomogeneous dephasing time of a chromophore can be measured using the stimulated photon echo (PE) experimental technique that measures the amplitude of the rephasing signal at a series of t_1 delays while the t_2 delay remains at zero throughout the experiment (**Fig 1.4A**)[44]. When a vibrational mode is inhomogeneously broadened, the chromophore's ability to rephase will shift the maximum amplitude of the rephasing signal to a positive t_1 delay (**Fig. 1.5**). When the vibrational mode does not experience any inhomogeneous broadening, the maximum

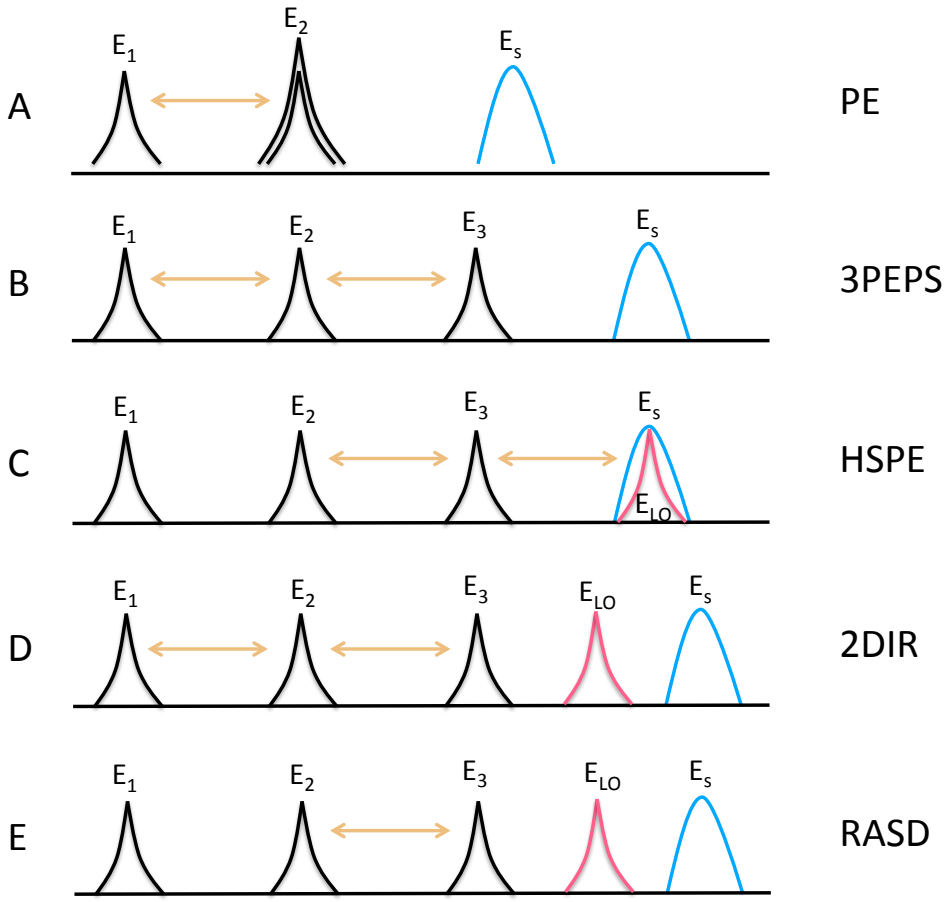

Figure 1.4 All third order experiments require the chromophore to interact with three fields (represented in black) that will then generate the measured signal (represented in blue), which, when heterodyne detected, is interfered with the local oscillator (represented in pink). What differentiates these experiments are the time delays that are scanned during the measurement. For each experiment, the scanned time delayed is demarked by the bronze arrow. The stimulated photon echo (PE) and three-pulse photon echo peak shift (3PEPS) experiments are homodyne detected while the heterodyne detected stimulated photon echo (HSPE), two-dimensional infrared spectroscopy (2DIR), and rapidly acquired spectral diffusion (RASD) experiments are heterodyne detected. (Adapted from Mukamel 1995)

amplitude of the rephasing signal will be at t_1 = 0 fs. Plotting the log of the rephasing signal amplitude against the t_1 delay, the slope of the decay of the rephasing signal amplitude can be used as a measure of the dephasing time constant. Using the PE experiment to study the O-H stretch of HOD in D_2O, the dephasing time of O-H, T_2, was found to be 90 fs, which suggests that the inhomogeneous width of O-H is 66 cm^{-1}

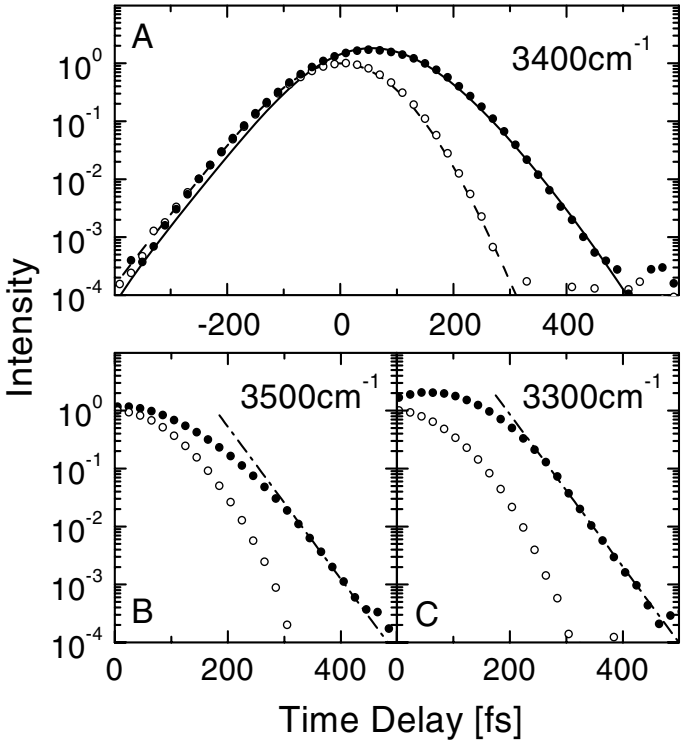

Figure 1.5 Amplitude of the rephasing signal as a function of the t_1 delay time at three spectral positions (°: instantaneous response in CaF_2; •: response of HDO in D_2O). The solid line in (a) represents the global fit of the water data, the dotted line the fit of the instantaneous response. Note, the peak maximum is at a positive t_1 delay time (Stenger 2001).

in D_2O[45].

1.7.4 Three-pulse photon echo peak shift. Measuring the FFCF with a third order technique was first accomplished with the three-pulse photon echo peak shift (3PEPS) experiment by measuring the rephasing signal maximum amplitude shift along t_1 seen in the PE experiment as a function of the t_2 delay. The experimental setup of 3PEPS is similar to that of PE, but requires the that both the t_1 and t_2 delays be stepped (**Fig 1.4B**)[46] independently creating a two-dimensional matrix, t_1 and t_2 being the dimensions, of the rephasing signal amplitude. The peak shift can be extracted at each t_2 delay to measure the ability of the chromophore to rephase at that t_2 delay. Because a chromophore that undergoes spectral diffusion during the t_2 delay time will lose its

ability to rephase, the t_2 dependence of peak shift is a measure of the chromophore's spectral diffusion. The 3PEPS experimental technique measured the tail of the spectral diffusion process of O-H stretch in D_2O to have a time constant of 5-15 ps time scale[47], which, although interesting, lacks the information of the hydrogen bond dynamics that occur on the femtosecond time scale.

1.7.5 Heterodyne detected stimulated photon echo. Similar to 3PEPS, the heterodyne detected stimulated photon echo (HSPE) experiment utilizes the ability of the chromophore to rephase as a measure of the FFCF. Rather than using t_1 peak shift as a measure of rephasing, HSPE utilizes the delay of the photon echo after E_3 as a proxy for rephasing (**Fig 1.4C**)[48, 49]. The photon echo delay arises because the time required for rephasing during the t_3 coherence is inherently equal to the dephasing time of the t_1 coherence. Measuring the time delay of the photon echo requires a fourth pulse, the local oscillator E_{LO}, used for heterodyne detection. The time delay of the photon echo is determined by measuring the rephasing signal at a series of τ_{LO} delays. As before, if the chromophore experiences spectral diffusion during t_2 it loses the ability to rephase, which for the HSPE experiment will cause the delay of the photon echo to decrease. The FFCF decay times of the O-H stretch of HOD in D_2O measured by HSPE was found to be 130 and 900 fs, assigned to the lifetime of a single hydrogen bond and the relaxation of the hydrogen bond network respectively[50].

1.7.6 Two-dimensional infrared spectroscopy. Spectral interferometry and its ability to ability to measure the phase of the signal generated by the third order polarization[51], $P^{(3)}$, allowed for the innovation of a new third order experiment, two-dimensional

infrared spectroscopy (2DIR). The acquisition of the data for single 2DIR spectrum requires the rephasing or nonrephasing signal to be measured at a series of t_1 delay times while holding the t_2 delay constant (**Fig 1.4D**), but unlike the experiments described above that allow for the signal to be measured by a single pixel detector, spectral interferometry requires the signal to be spectrally resolved before being measured by a pixel array detector. After the data is acquired, the 2DIR spectrum is generated by performing spectral interferometry on the acquired data followed by a Fourier transform along the t_1 axis.

The 2DIR spectrum generated through this process correlates the frequencies of the coherences during t_1 and t_3 by plotting their corresponding frequencies, ω_1 and ω_3, against each other. This ability of 2DIR to measure the frequency correlation during two separate time periods gives it the inherent ability to measure the FFCF of spectral diffusion by measuring a 2DIR spectrum at a series of t_2 delay times. At an early t_2 time delay, the frequencies during t_1 and t_3 are highly correlated causing the peak to be elongated along the diagonal; while at a large t_2 delay that allows for spectral diffusion, the frequencies during t_1 and t_3 lose correlation causing the peak to take a rounded shape (**Fig 1.6**). The FFCF can be extracted through a variety of features of an absorptive 2DIR spectrum. For example, Lazonder *et al*. demonstrated that the ellipticity of the fundamental transition frequency band can be related to the FFCF[52, 53], and Asbury *et al*. showed that the FFCF can be related to the line width of a single frequency[39], ω_3. Eaves *et al.* and Loparo *et al.* measured the dynamics of hydrogen bonding using the nodal line slope (NLS) to measure the FFCF of the O-H stretch of HOD in D_2O and found that

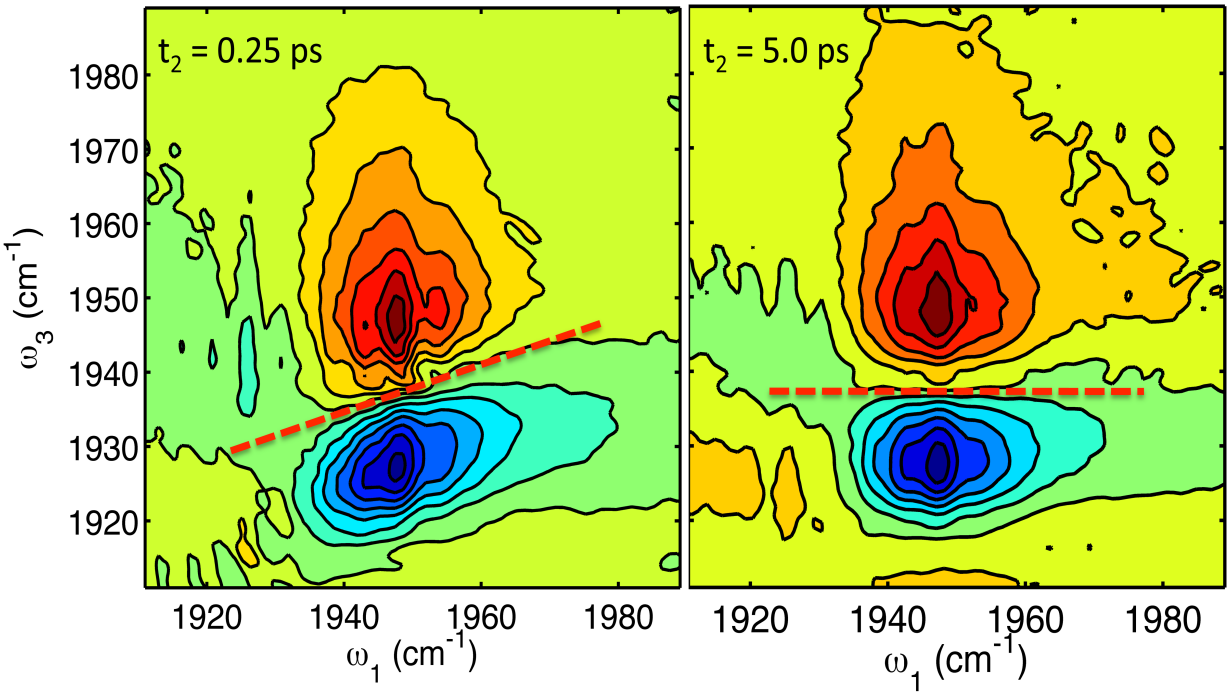

Figure 1.6 2DIR Spectra of cyclopentadienyl manganese tricarbonyl's asymmetric peak in methanol at t_2 time steps of (A) 0.25 ps and (B) 5 ps. Each spectrum consists of 2 peaks, a positive valued fundamental peak at 1947 cm^{-1} and the anharmonic peak at 1928 cm^{-1}. At early times, the nodal line (NL) in red is slanted due to inhomogeneous broadening. At later times, the NL has no slope due to a loss of memory of the original vibrational frequency.

strained hydrogen bond configurations do not persist for an extended period of time and a hydrogen bond will reform in less that 150 fs[13, 54, 55]. Using the center-line slope (CLS) Park *et al.* measured the same FFCF and found it to have a fast, 400 fs, and slow component, 1.7 ps, representing the hydrogen bond fluctuations (i.e. wobbling in a cone) and the hydrogen bond network randomization respectively[15].

Despite the differences between 2DIR and the experiments previously described, measuring the FFCF with 2DIR is also dependent on the ability of the chromophore to rephase during the t_3 coherence to reverse the inhomogeneous dephasing incurred during t_1 coherence. The absorptive 2DIR spectrum (**Fig. 1.6**) is the sum of the rephasing and nonrephasing 2DIR spectra, which are elongated along the diagonal and anti-diagonal respectively. When a chromophore experiences inhomogeneous broadening,

the magnitude of the rephasing spectrum will be larger than the nonrephasing spectrum causing the absorptive spectrum to be elongated along the diagonal. Roberts and coworkers developed the inhomogeneous index to extract the FFCF from the rephasing and nonrephasing 2DIR spectrum amplitude rather than from the absorptive spectrum:

$$II = \frac{A_R - A_N}{A_R + A_N} \quad (4)$$

Where II is the inhomogeneous index and A_R and A_N are the amplitudes of the rephasing and nonrephasing spectrum. Much of the work presented in this thesis uses the inhomogeneous index as a measure of the FFCF including the development of a novel third order technique that greatly reduces the experimental data acquisition time.

1.8 Summary

To make significant progress in exploring the interfacial dynamics of both hydration water and the biomolecules it solvates, we need new chemical probes as well as ultrafast, multidimensional optical techniques that we can interpret in terms of fundamental molecular dynamics. This thesis describes efforts to introduce both new metal carbonyl based vibrational probes of membrane-water interfaces, as well as fundamental studies of these labels in more simple environments. To increase experimental throughput and ensure robust experimental trends, we developed new experimental approaches for measuring ultrafast dynamics that extract specifically the key spectral diffusion observable of interest that can be linked to fast molecular motion in bulk, nanoconfined, and interfacial contexts.

1.9 References

1. Ball, P., "Water as an active constituent in cell biology". *Chemical reviews* **2008,** *108* (1), 74.

2. Ellis, R. J., "Macromolecular crowding: an important but neglected aspect of the intracellular environment". *Current Opinion in Structural Biology* **2001,** *11* (1), 114-119.

3. Arakawa, T.; Timasheff, S., "The stabilization of proteins by osmolytes". *Biophysical Journal* **1985,** *47* (3), 411.

4. Luby-Phelps, K.; Lanni, F.; Taylor, D. L., "The submicroscopic properties of cytoplasm as a determinant of cellular function". *Annual Review of Biophysics and Biophysical Chemistry* **1988,** *17* (1), 369-396.

5. Zimmerman, S. B.; Trach, S. O., "Estimation of macromolecule concentrations and excluded volume effects for the cytoplasm of Escherichia coli". *Journal of Molecular Biology* **1991,** *222* (3), 599-620.

6. Chandler, D., "Interfaces and the driving force of hydrophobic assembly". *Nature* **2005,** *437* (7059), 640-647.

7. Pal, S. K.; Peon, J.; Bagchi, B.; Zewail, A. H., "Biological water: femtosecond dynamics of macromolecular hydration". *The Journal of Physical Chemistry B* **2002,** *106* (48), 12376-12395.

8. Pal, S. K.; Peon, J.; Zewail, A. H., "Biological water at the protein surface: Dynamical solvation probed directly with femtosecond resolution". *Proceedings of the National Academy of Sciences* **2002,** *99* (4), 1763-1768.

9. Nucci, N. V.; Pometun, M. S.; Wand, A. J., "Site-resolved measurement of water-protein interactions by solution NMR". *Nature structural & molecular biology* **2011,** *18* (2), 245-249.

10. Franck, J. M.; Scott, J. A.; Han, S., "Nonlinear Scaling of Surface Water Diffusion with Bulk Water Viscosity of Crowded Solutions". *Journal of the American Chemical Society* **2013**.

11. Damodaran, K.; Merz Jr, K. M., "Head group-water interactions in lipid bilayers: a comparison between DMPC-and DLPE-based lipid bilayers". *Langmuir* **1993,** *9* (5), 1179-1183.

12. Jendrasiak, G. L.; Smith, R. L., "The interaction of water with the phospholipid head group and its relationship to the lipid electrical conductivity". *Chemistry and physics of lipids* **2004,** *131* (2), 183-195.

13. Eaves, J. D.; Loparo, J. J.; Fecko, C. J.; Roberts, S. T.; Tokmakoff, A.; Geissler, P. L., "Hydrogen bonds in liquid water are broken only fleetingly". *Proc. Natl. Acad. Sci. U. S. A.* **2005,** *102* (37), 13019-13022.

14. Nicodemus, R. A.; Ramasesha, K.; Roberts, S. T.; Tokmakoff, A., "Hydrogen Bond Rearrangements in Water Probed with Temperature-Dependent 2D IR". *The Journal of Physical Chemistry Letters* **2010,** *1* (7), 1068-1072.

15. Park, S.; Fayer, M. D., "Hydrogen bond dynamics in aqueous NaBr solutions". *Proc. Natl. Acad. Sci. U. S. A.* **2007,** *104* (43), 16731-16738.

16. Costard, R.; Levinger, N. E.; Nibbering, E. T.; Elsaesser, T., "Ultrafast Vibrational Dynamics of Water Confined in Phospholipid Reverse Micelles". *The Journal of Physical Chemistry B* **2012,** *116* (19), 5752-5759.

17. Moilanen, D. E.; Fenn, E. E.; Wong, D.; Fayer, M. D., "Water Dynamics at the Interface in AOT Reverse Micelles". *The Journal of Physical Chemistry B* **2009,** *113* (25), 8560-8568.

18. Fenn, E. E.; Wong, D. B.; Fayer, M. D., "Water dynamics in small reverse micelles in two solvents: Two-dimensional infrared vibrational echoes with two-dimensional background subtraction". *Journal of Chemical Physics* **2011,** *134* (5).

19. Fenn, E. E.; Wong, D. B.; Giammanco, C. H.; Fayer, M. D., "Dynamics of Water at the Interface in Reverse Micelles: Measurements of Spectral Diffusion with Two-Dimensional Infrared Vibrational Echoes". *J. Phys. Chem. B* **2011,** *115* (40), 11658-11670.

20. Yang, M.; Szyc, Å.; Elsaesser, T., "Decelerated Water Dynamics and Vibrational Couplings of Hydrated DNA Mapped by Two-Dimensional Infrared Spectroscopy". *The Journal of Physical Chemistry B* **2011,** *115* (44), 13093-13100.

21. King, J. T.; Kubarych, K. J., "Site-Specific Coupling of Hydration Water and Protein Flexibility Studied in Solution with Ultrafast 2D-IR Spectroscopy". *Journal of the American Chemical Society* **2012,** *134* (45), 18705-18712.

22. King, J. T.; Ross, M. R.; Kubarych, K. J., "Water-Assisted Vibrational Relaxation of a Metal Carbonyl Complex Studied with Ultrafast 2D-IR". *J. Phys. Chem. B* **2012,** *116* (12), 3754-3759.

23. Kubo, R., A Stochastic Theory of Line Shape. In *Advances in Chemical Physics*, John Wiley & Sons, Inc.: 1969; pp 101-127.

24. Skinner, J. L.; Auer, B. M.; Lin, Y.-S., "VIBRATIONAL LINE SHAPES, SPECTRAL DIFFUSION, AND HYDROGEN BONDING IN LIQUID WATER". *Advances in Chemical Physics, Vol 142* **2009,** *142*, 59-103.

25. Bublitz, G. U.; Boxer, S. G., "Stark spectroscopy: Applications in chemistry, biology, and materials science". *Annual Review of Physical Chemistry* **1997,** *48*, 213-242.

26. Liptay, W., "ELECTROCHROMISM AND SOLVATOCHROMISM". *Angew. Chem.-Int. Edit.* **1969,** *8* (3), 177-&.

27. Tamm, L. K.; Tatulian, S. A., "Infrared spectroscopy of proteins and peptides in lipid bilayers". *Quarterly Reviews of Biophysics* **1997,** *30* (4), 365-429.

28. Krimm, S.; Bandekar, J., "VIBRATIONAL SPECTROSCOPY AND CONFORMATION OF PEPTIDES, POLYPEPTIDES, AND PROTEINS". *Advances in Protein Chemistry* **1986,** *38*, 181-364.

29. Caughey, W. S.; Shimada, H.; Choc, M. G.; Tucker, M. P., "DYNAMIC PROTEIN STRUCTURES - INFRARED EVIDENCE FOR 4 DISCRETE RAPIDLY INTERCONVERTING CONFORMERS AT THE CARBON-MONOXIDE BINDING-SITE OF BOVINE HEART MYOGLOBIN". *Proceedings of the National Academy of Sciences of the United States of America-Biological Sciences* **1981,** *78* (5), 2903-2907.

30. Lim, M. H.; Jackson, T. A.; Anfinrud, P. A., "Ultrafast rotation and trapping of carbon monoxide dissociated from myoglobin". *Nature Structural Biology* **1997,** *4* (3), 209-214.

31. Tsubaki, M.; Srivastava, R. B.; Yu, N. T., "RESONANCE RAMAN INVESTIGATION OF CARBON-MONOXIDE BONDING IN (CARBON MONOXY) HEMOGLOBIN AND (CARBON MONOXY) MYOGLOBIN - DETECTION OF FE-CO STRETCHING AND FE-C-O BENDING VIBRATIONS AND INFLUENCE OF THE QUATERNARY STRUCTURE CHANGE". *Biochemistry* **1982,** *21* (6), 1132-1140.

32. Frydman, L.; Scherf, T.; Lupulescu, A., "The acquisition of multidimensional NMR spectra within a single scan". *Proc. Natl. Acad. Sci. U. S. A.* **2002,** *99* (25), 15858-15862.

33. Anna, J. M.; King, J. T.; Kubarych, K. J., "Multiple Structures and Dynamics of CpRu(CO)(2) (2) and CpFe(CO)(2) (2) in Solution Revealed with Two-Dimensional Infrared Spectroscopy". *Inorganic Chemistry* **2011,** *50* (19), 9273-9283.

34. Anna, J. M.; Kubarych, K. J., "Watching solvent friction impede ultrafast barrier crossings: A direct test of Kramers theory". *Journal of Chemical Physics* **2010,** *133* (17).

35. Anna, J. M.; Ross, M. R.; Kubarych, K. J., "Dissecting Enthalpic and Entropic Barriers to Ultrafast Equilibrium Isomerization of a Flexible Molecule Using 2DIR Chemical Exchange Spectroscopy". *Journal of Physical Chemistry A* **2009,** *113* (24), 6544-6547.

36. Cahoon, J. F.; Sawyer, K. R.; Schlegel, J. P.; Harris, C. B., "Determining transition-state geometries in liquids using 2D-IR". *Science* **2008,** *319* (5871).

37. King, J. T.; Anna, J. M.; Kubarych, K. J., "Solvent-hindered intramolecular vibrational redistribution". *Physical Chemistry Chemical Physics* **2011,** *13* (13), 5579-5583.

38. King, J. T.; Baiz, C. R.; Kubarych, K. J., "Solvent-Dependent Spectral Diffusion in a Hydrogen Bonded "Vibrational Aggregate"". *Journal of Physical Chemistry A* **2010,** *114* (39), 10590-10604.

39. Asbury, J. B.; Steinel, T.; Stromberg, C.; Corcelli, S. A.; Lawrence, C. P.; Skinner, J. L.; Fayer, M. D., "Water dynamics: Vibrational echo correlation spectroscopy and

comparison to molecular dynamics simulations". *Journal of Physical Chemistry A* **2004,** *108* (7), 1107-1119.

40. Kwak, K.; Park, S.; Finkelstein, I. J.; Fayer, M. D., "Frequency-frequency correlation functions and apodization in two-dimensional infrared vibrational echo spectroscopy: A new approach". *Journal of Chemical Physics* **2007,** *127* (12), 17.

41. Oudar, J. L.; Hulin, D.; Migus, A.; Antonetti, A.; Alexandre, F., "Subpicosecond Spectral Hole Burning Due to Nonthermalized Photoexcited Carriers in GaAs". *Physical Review Letters* **1985,** *55* (19), 2074-2077.

42. Graener, H.; Seifert, G.; Laubereau, A., "NEW SPECTROSCOPY OF WATER USING TUNABLE PICOSECOND PULSES IN THE INFRARED". *Physical Review Letters* **1991,** *66* (16), 2092-2095.

43. Ogilvie, J. P.; Kubarych, K. J., Multidimensional Electronic and Vibrational Spectroscopy: An Ultrafast Probe of Molecular Relaxation and Reaction Dynamics. In *Advances in Atomic, Molecular, and Optical Physics, Vol 57*, Arimondo, E.; Berman, P. R.; Lin, C. C., Eds. Elsevier Academic Press Inc: San Diego, 2009; Vol. 57, pp 249-321.

44. de Boeij, W. P.; Pshenichnikov, M. S.; Wiersma, D. A., "ULTRAFAST SOLVATION DYNAMICS EXPLORED BY FEMTOSECOND PHOTON ECHO SPECTROSCOPIES". *Annual Review of Physical Chemistry* **1998,** *49* (1), 99-123.

45. Stenger, J.; Madsen, D.; Hamm, P.; Nibbering, E. T. J.; Elsaesser, T., "Ultrafast vibrational dephasing of liquid water". *Physical Review Letters* **2001,** *87* (2).

46. Joo, T. H.; Jia, Y. W.; Yu, J. Y.; Lang, M. J.; Fleming, G. R., "Third-order nonlinear time domain probes of solvation dynamics". *Journal of Chemical Physics* **1996,** *104* (16), 6089-6108.

47. Stenger, J.; Madsen, D.; Hamm, P.; Nibbering, E. T. J.; Elsaesser, T., "A photon echo peak shift study of liquid water". *Journal of Physical Chemistry A* **2002,** *106* (10), 2341-2350.

48. de Boeij, W. P.; Pshenichnikov, M. S.; Wiersma, D. A., "Phase-locked heterodyne-detected stimulated photon echo. A unique tool to study solute,ÄîsolventÄì interactions". *Chem. Phys. Lett.* **1995,** *238* (1,Äì3), 1-8.

49. de Boeij, W. P.; Pshenichnikov, M. S.; Wiersma, D. A., "Heterodyne-detected stimulated photon echo: applications to optical dynamics in solution". *Chem. Phys.* **1998,** *233* (2-3), 287-309.

50. Yeremenko, S.; Pshenichnikov, M. S.; Wiersma, D. A., "Hydrogen-bond dynamics in water explored by heterodyne-detected photon echo". *Chem. Phys. Lett.* **2003,** *369* (1,Äì2), 107-113.

51. Lepetit, L.; ChÈriaux, G.; Joffre, M., "Linear techniques of phase measurement by femtosecond spectral interferometry for applications in spectroscopy". *J. Opt. Soc. Am. B* **1995,** *12* (12), 2467-2474.

52. Lazonder, K.; Pshenichnikov, M. S.; Wiersma, D. A., "Easy interpretation of optical two-dimensional correlation spectra". *Opt. Lett.* **2006,** *31* (22), 3354-3356.

53. Lazonder, K.; Pshenichnikov, M. S.; Wiersma, D. A., "Two-dimensional optical correlation spectroscopy applied to liquid/glass dynamics". *Ultrafast Phenomena XV* **2007,** *88*, 356-358.

54. Loparo, J. J.; Roberts, S. T.; Tokmakoff, A., "Multidimensional infrared spectroscopy of water. I. Vibrational dynamics in two-dimensional IR line shapes". *Journal of Chemical Physics* **2006,** *125* (19).

55. Loparo, J. J.; Roberts, S. T.; Tokmakoff, A., "Multidimensional infrared spectroscopy of water. II. Hydrogen bond switching dynamics". *Journal of Chemical Physics* **2006,** *125* (19).

Chapter Two

Developing Accelerated Spectroscopic Techniques: Rapidly Acquired Spectral Diffusion

The work of this chapter has been published as the following article:

Derek G. Osborne and Kevin J. Kubarych "*Rapid and Accurate Measurement of the Frequency-Frequency Correlation Function*" Journal of Physical Chemistry A (In press)

2.1 Introduction

Condensed phase chemical dynamics are, in principle, encoded in the linear and nonlinear optical response functions that underlie vibrational and electronic spectroscopy. Extracting the dynamical information, however, is generally complicated due to the inability of one-dimensional methods to separate homogeneous and inhomogeneous contributions to broadened line shapes. As the local microenvironment of a chromophore in the condensed phase changes due to the dynamics of the solvent, the transition frequency also changes, a process known as "spectral diffusion," which

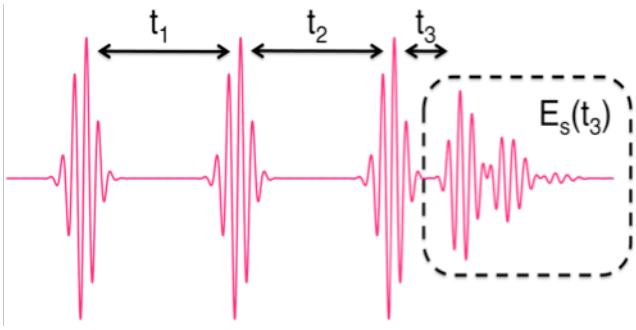

Figure 2.1 The time ordering conventions of the four-wave mixing experiments presented here. The three pulses generated by the laser give rise to the polarization that produces the signal $E_s(t_3)$ are separated by t_1, t_2, and t_3.

gives rise to the decay of the frequency-frequency correlation function (FFCF) of a given spectroscopic transition. The FFCF is defined as $C(t) = \langle \delta\omega(0)\delta\omega(t) \rangle$, where represents an instantaneous frequency fluctuation from the average $\langle \omega \rangle$, such that $\delta\omega(t) = \omega(t) - \langle \omega \rangle$. Experimentally measuring this FFCF has long been a goal of ultrafast optics and multidimensional spectroscopy.

Three-pulse Photon echo peak shift (3PEPS) is a well known experimental method that utilizes rephasing induced asymmetry to measure the FFCF, but global fitting of the data is needed to extract the FFCF from the spectroscopic features, requiring previous knowledge of the system[1-3]. Moreover, in a conventional 3PEPS experiment, both the coherence time (t_1) and the waiting time (t_2) must be scanned, resulting in a two (time) dimensional data set that requires significant acquisition times. In the past decade, two-dimensional infrared spectroscopy (2DIR) has proven to offer a robust means for measuring the FFCF[4-10]. The FFCF can be extracted through a variety of absorptive 2DIR spectroscopic features. Kwak *et al.*, for example, proposed the use of

the center line slope to report the FFCF[11], while Lazonder *et al*. demonstrated that the ellipticity of the fundamental transition frequency band can be related to the FFCF[12,13], and Asbury *et al*. showed that the FFCF can be related to the line width of a single frequency, w_3[14]. These spectroscopic features in the absorptive 2DIR spectrum arise from differences in amplitude between the rephasing and nonrephasing Liouville space pathways[15]. Roberts *et al*. proposed an alternative method of extracting the FFCF by comparing the rephasing and nonrephasing amplitudes directly using 2D-IR absolute magnitude spectra[16]. Here, we refer to this approach as the 2DIR "peak volume inhomogeneous index" (PVII).

Recently, Park *et al*. proposed that the chromophore's ability to rephase, and therefore the FFCF, could be measured without scanning the coherence time (t_1, see Fig. 2.1 for ordering conventions), denoting their approach "t_1 resolved transient grating" (TRTG)[17]. By avoiding the t_1 scan, data acquisition and processing time is greatly reduced. Although a promising method of rapidly measuring the FFCF, TRTG does not ideally measure the FFCF. The TRTG setup uses two photodiodes to measure the rephasing and nonrephasing spectra simultaneously in a background free direction. By detecting the rephasing and nonrephasing spectrum simultaneously, the magnitude of t_1 for the rephasing and nonrephasing signal is inherently the same, but, in practice, by using two independent detectors it is not possible to measure the static inhomogeneity and the use of a photodiode makes it difficult to measure the FFCF of a single mode in a cluttered spectrum since there is no spectral selection of the signal. Replacing the two photodiodes with a spectrograph and an array detector affords spectral resolution of

the signal, but with considerably added experimental complexity. Nevertheless, one could imagine recording the rephasing and nonrephasing signals on two different regions of the same CCD detector.

Reduced dimensionality approaches have been long used in NMR spectroscopy, where recording full multidimensional spectra can require significant measurement times.[18,19] For instance, methods such as accordion spectroscopy make use of scanning both t_1 and t_2 simultaneously though at different rates over different time ranges, resulting in a distorted 1D spectrum where the kinetics of chemical exchange are encoded in the spectral line widths.[20] Here, we demonstrate that a central observable of ultrafast 2D spectroscopy, the FFCF, can be measured with good fidelity without scanning t_1, but by utilizing the inhomogeneous index for the spectrally resolved, heterodyne detected signal. Additionally, we demonstrate how to accurately duplicate the t_1 delay so that the rephasing and nonrephasing signals can be measured on a single detector, in principle allowing measurements of the static inhomogeneous component. To test the utility of rapidly acquired spectral diffusion (RASD) we first explore the theory of the method and then compare the experimentally measured FFCF of one of the carbonyl stretching bands of cyclopentadienyl manganese tricarbonyl (CMT) using alternatively RASD and PVII. We find that the RASD directly measures the FFCF and the experimentally measured PVII and RASD are comparable. Without the need to scan t_1, the FFCF can be measured orders of magnitude faster, with two orders of magnitude more data points representing the FFCF, while avoiding potential phase errors that are common to 2DIR and create uncertainties in the measurements.

2.2 Methods

CMT, methanol, and butanol were purchased from Sigma Aldrich and were used without further purification. Sample solutions were made to give a concentration of ~3 mM. The sample cell consisted of two 3mm thick CaF_2 windows that were separated by a 100 mm Teflon spacer.

The experimental setup and data acquisition used here has been reported previously[21]. Briefly, three 100 fs infrared pulses are generated by a white light seeded b-barium borate optical parametric amplifier (OPA) and difference frequency generation (DFG). The signal, $E_s(t_3)$, is collinearly mixed with a slightly delayed local oscillator. We measure dispersed single shot $E_s(t_3)$ and local oscillator with a 1340x100 pixel CCD camera after $E_s(t_3)$ and local oscillator are upconverted to the visible using sum-frequency generation with a chirped 800-nm pulse[22]. Single shot detection enables t_1 and t_2 to be scanned continuously during data acquisition, and for each frame of the scan, the absolute $E_s(t_3)$ is integrated over the frequency range of interest. For 2DIR spectroscopy, diagonal peaks are differentiated from cross peaks by Fourier transforming with respect to t_1, giving ω_1. By not performing this Fourier transform over t_1 we are effectively integrating over ω_1. This lack of discrimination between Liouville pathways that would give rise to cross and diagonal peaks is manifested in t_1 scans as a signal modulation. A t_1 time scan refers to scanning E_1 in the negative time direction while E_2 and E_3 remain stationary while a t_2 time scan refers to E_3 being scanned to positive times while E_1 and E_2 remain stationary. For the t_1 time scan data

presented here, both the rephasing and nonrephasing data are averaged over 5 scans while they are averaged over 10 scans for the t_2 scans. We use zinc selenide, n_D=2.6, wedge pairs (7° apex angle) to manipulate the t_1 delay time. These wedges are calibrated to account for deformities prior to the experiment using spectral interferometry as described in our previous work. The linear encoders on the motors controlling the wedge position are capable of achieving 7.3724 nm resolution. In practice we find that the minimum displacement achievable is 36.86 nm. A movement of 36.86 nm will increase the zinc selenide optical path by 4.525 nm which results in a time delay resolution of 0.025 fs. Making our time delay resolution more than 500 times smaller than the optical cycle. Due to the unreliability of early t_2 times, where pulse overlap is not entirely eliminated, the fits exclude the first 250 fs of t_2.

2.3 Theory

2.3.1 Nonlinear optics. The experiments presented here are third-order nonlinear optical processes that require the sample to interact with three infrared fields separated in time by t_1, t_2, and t_3 (Fig. 2.1). These three fields create a third-order nonlinear polarization $P^{(3)}(t)$

$$P^{(3)}(t) = \int_{-\infty}^{\infty} dt_3 \int_{-\infty}^{\infty} dt_2 \int_{-\infty}^{\infty} dt_1 R^{(3)}(t_1, t_2, t_3) E(t)^3 \tag{1}$$

that generates the measured signal field, $E_s(t_3)$. Due to conservation of momentum, the rephasing and nonrephasing signals are emitted in the $-k_1 + k_2 + k_3$ and $k_1 - k_2 + k_3$ directions, respectively, allowing us to detect the rephasing and nonrephasing signal separately in a background free direction. The distinction between rephasing and

nonrephasing arises from the evolution of the phase during t_1 and t_3. In a linear spectrum, which results from the interference of the linear free-induction decay signal and transmitted excitation field, dephasing arises from both (i.e. homogeneous) pure dephasing, which is inherently irreversible, and from inhomogeneities, which are, at least in principle, reversible. For a system with some degree of inhomogeneous broadening, which may be either static or dynamic, a rephasing echo leads to a larger amplitude signal relative to the nonrephasing signal provided the same inhomogeneity is present during the second coherence time (t_3). If the vibrational frequencies of the chromophores become altered during the waiting time (t_2) the rephasing pulse sequence will be less effective at producing an echo, and the rephasing and nonrephasing signals will be of similar amplitude. As t_2 is increased, the solvent molecules creating the microenvironment have more time to reorient and reduce the amplitude of the rephasing signal, and at large t_2 times, where $C(t_2)$ is fully decayed, the rephasing signal amplitude matches that of the nonrephasing signal amplitude. It is this difference in amplitude, the inhomogeneous index (II) that we use to determine the FFCF.

$$II = \frac{A_r - A_n}{A_r + A_n} \tag{2}$$

2.3.2 Response function. Typically, infrared spectroscopy is modeled through the use of response functions where the linear response function under the second-order cumulant approximation, the bath potential surface is assumed to be harmonic, is represented as[10,15]:

$$R^{(1)}(t) = \left|\mu_{0,1}\right|^2 \exp\left[-g^1(t) - i\omega_{0,1}t\right] \tag{3}$$

The orientational relaxation, vibrational lifetime, and the homogeneous dephasing can

be added to eq. 3 phenomenologically but are omitted for simplicity. $g^{(1)}(t)$ is the line shape function:

$$g^{(1)}(t) = \left\langle \delta\omega^2 \right\rangle \int_0^t d\tau_2 \int_0^{\tau_2} d\tau_1 \bar{C}(\tau_1) \tag{4}$$

where is the normalized FFCF, $\bar{C}(t) = \left\langle \delta\omega(t)\delta\omega(0) \right\rangle / \left\langle \delta\omega^2 \right\rangle$, that we seek to extract through experimental methods. The form of has been discussed extensively elsewhere[23,24], but is generally treated as being a sum of exponentials, though we have observed examples of nonexponential FFCFs in probe chromophores in glass forming liquids.

The third-order nonlinear response function $R^{(3)}(t_1,t_2,t_3)$ used to model absorptive 2DIR is the sum of the rephasing and nonrephasing response functions. Under the short time approximation, a commonly used approximation in vibrational spectroscopy[11,16], where the dephasing times, t_1, t_3, are assumed to be short relative to the t_2[25] dependent correlation function,

$$g^{(1)} = \frac{1}{2}\langle \delta\omega^2 \rangle t^2 \tag{5}$$

For CMT in methanol and butanol, the FWHM of the linear absorption is 16 cm^{-1}, which, assuming a Gaussian line shape and dephasing, corresponds to a dephasing time of 320 fs. The dephasing time of 320 fs is significantly faster than the measured correlation time scales presented below. The rephasing and nonrephasing response functions of a two level system can be written as:

$$R_r^{(3)}(t_1,t_2,t_3) = \exp\left[\frac{-\langle\delta\omega^2\rangle}{2}\left(t_3^2 + t_1^2 - 2t_1t_3\,\bar{C}(t_2)\right)\right]\exp\left[i\langle\omega\rangle(t_3 - t_1) - 2iQ(t_2)t_3\right] \tag{6}$$

$$R_n^{(3)}(t_1,t_2,t_3) = \exp\left[\frac{-\langle\delta\omega^2\rangle}{2}\left(t_3^2 + t_1^2 + 2t_1t_3\,\bar{C}(t_2)\right)\right]\exp\left[i\langle\omega\rangle(t_3 - t_1)\right] \tag{7}$$

$$Q(t_2) \equiv \bar{C}(t_2) - \frac{\lambda}{\hbar} \tag{8}$$

where l is the solvation reorganization energy.

2.3.3 Inhomogeneous index. Here, we develop the theoretical formulation of the frequency-frequency correlation function (FFCF) that can be measured from a nonlinear experiment without scanning t_1[26]. The amplitudes of the rephasing and nonrephasing signals are the time integrals (over t_3) of the absolute third-order response functions. First we take the absolute value of the response function:

$$\left|R_r^{(3)}\right| = \exp\left[\frac{-\langle\delta\omega^2\rangle}{2}\left(t_1^2 + t_3^2 - 2t_1t_3\,\bar{C}(t_2)\right)\right] \tag{9}$$

$$\left|R_n^{(3)}\right| = \exp\left[\frac{-\langle\delta\omega^2\rangle}{2}\left(t_1^2 + t_3^2 + 2t_1t_3\,\bar{C}(t_2)\right)\right] \tag{10}$$

We then integrate over t_3:

$$\int_0^\infty \left|R_r^{(3)}\right| dt_3 = \exp\left[\frac{-\langle\delta\omega^2\rangle}{2}t_1^2\right]\int_0^\infty \exp\left[\frac{-\langle\delta\omega^2\rangle}{2}\left(t_3^2 - 2t_1t_3\,\bar{C}(t_2)\right)\right]dt_3 \tag{11}$$

$$\int_0^\infty \left|R_n^{(3)}\right| dt_3 = \exp\left[\frac{-\langle\delta\omega^2\rangle}{2}t_1^2\right]\int_0^\infty \exp\left[\frac{-\langle\delta\omega^2\rangle}{2}\left(t_3^2 + 2t_1t_3\,\bar{C}(t_2)\right)\right]dt_3 \tag{12}$$

Defining b and g as:

$$b = \frac{\left\langle \delta\omega^2 \right\rangle}{2} \qquad g = 2t_1 \bar{C}\left(t_2\right) \tag{13}$$

The integral can be simplified as:

$$\int_0^\infty \left| R_r^{(3)} \right| dt_3 = \exp\left[bt_1^2 \right] \int_0^\infty \exp\left[bt_3^2 + bgt_3 \right] dt_3 \tag{14}$$

$$\int_0^\infty \left| R_n^{(3)} \right| dt_3 = \exp\left[bt_1^2 \right] \int_0^\infty \exp\left[bt_3^2 - bgt_3 \right] dt_3 \tag{15}$$

Performing the integral, and defining $A_\pm$ as $\int_0^\infty |R_\pm| dt_3$, $A_\pm$ is defined as:

$$A_r = \int_0^\infty \left| R_r^{(3)} \right| dt_3 = \frac{\sqrt{\pi} \exp\left[bt_1^2 + g^2 b/4 \right] \left[1 + erf\left(\frac{g\sqrt{b}}{2} \right) \right]}{2\sqrt{b}} \tag{16}$$

$$A_n = \int_0^\infty \left| R_n^{(3)} \right| dt_3 = \frac{\sqrt{\pi} \exp\left[bt_1^2 + g^2 b/4 \right] \left[1 - erf\left(\frac{g\sqrt{b}}{2} \right) \right]}{2\sqrt{b}} \tag{17}$$

If H and Q are defined as:

$$H = \frac{\sqrt{\pi} \exp\left[bt_1^2 + g^2 b/4 \right]}{2\sqrt{b}} \qquad Q = erf\left(\frac{g\sqrt{b}}{2} \right) \tag{18}$$

A_+ and A_- become:

$$A_n = H\left(1 - Q\right) \quad A_r = H\left(1 + Q\right) \tag{19}$$

The inhomogeneous index, *II*, is defined as:

$$II = \frac{A_r - A_n}{A_r + A_n} \tag{20}$$

Making the inhomogeneous index of the RASD experiment defined as:

$$II = Q \tag{21}$$

Reintroducing the Q, b and g, the inhomogeneous index becomes:

$$II = erf\left(t_1 \bar{C}(t_2) \sqrt{\langle \delta\omega^2 \rangle / 2} \right) \tag{22}$$

Where erf is the error function. Finally, we solve for the FFCF:

$$\bar{C}(t_2) = \frac{erf^{-1}(II)\sqrt{2}}{t_1 \sqrt{\langle \delta\omega^2 \rangle}} \tag{23}$$

For small values of *II* the FFCF is directly proportional to *II*, scaled by $\frac{1}{t_1}\sqrt{\frac{2}{\langle \delta\omega^2 \rangle}}$.

Therefore, the FFCF can be directly measured by setting t_1 to a specific delay and then scanning t_2.

2.4 Experimental

2.4.1 Setting t_1. Correctly measuring the FFCF with a single detector using RASD requires the delay between the first two pulses, t_1, to be duplicated for both the rephasing and nonrephasing, $\delta t_1 = t_1^{rep} - t_1^{non} = 0$, which requires an accurate determination of $t_1 = 0$. We first approximate $t_1 = 0$ by scattering E_1 and E_2 through a pinhole and detecting the spectral interferogram as E_1 is scanned relative to E_2. Due to the finite precision of pinhole scattering[27], which is 20 mm, we more accurately identify $t_1 = 0$ by using features from the recorded t_1 scan. In the presence of multiple IR active modes, the excited coherences will cause modulations of the signal as t_1 is scanned (Fig. 2.2A). Although the rephasing and nonrephasing response functions have opposite phases during t_1 the envelope of the low frequency beatings in the rephasing and

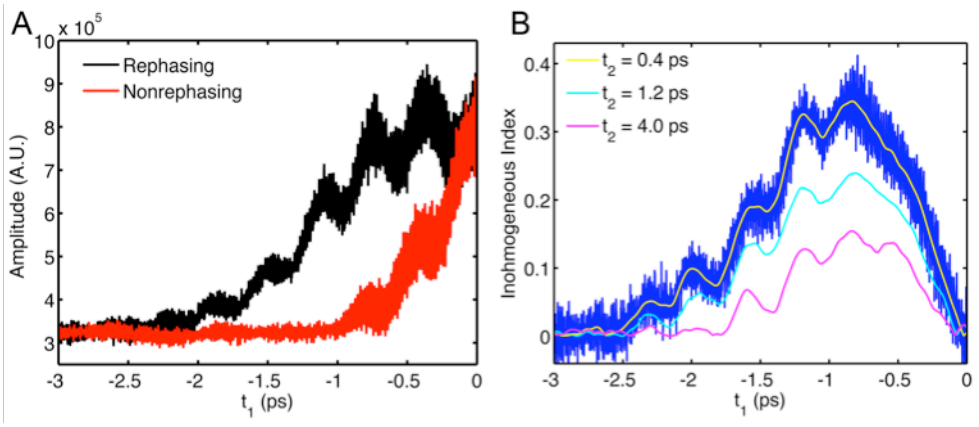

Figure 2.2 (A) The t_1 time delay is continuously scanned while $E_s(t_3)$ is measured and integrated over the asymmetric stretch of CMT. The high frequency oscillations along t_1 arise from interference between E_1 and E_2 and the beatings arise being excited at the symmetric stretch during t_1 and the asymmetric stretch during t_3. (B) The inhomogeneous index along t_1 is taken to determine the t_1 value that maximizes the signal to noise ratio to be used while measuring the FFCF. The high frequency oscillations are removed using a low pass filter and are plotted for various t_2 delays. **2.** (A) The t_1 time delay is continuously scanned while $E_s(t_3)$ is measured and integrated over the asymmetric stretch of CMT. The high frequency oscillations along t_1 arise from interference between E_1 and E_2 and the beatings arise being excited at the symmetric stretch during t_1 and the asymmetric stretch during t_3. (B) The inhomogeneous index along t_1 is taken to determine the t_1 value that maximizes the signal to noise ratio to be used while measuring the FFCF. The high frequency oscillations are removed using a low pass filter and are plot for varying t_2 delays.

nonrephasing response functions will have identical phases, and because we only analyze the absolute value, the high frequency oscillations will also appear to be of the same phase. We set the final $t_1 = 0$ by adjusting t_1 such that the maximum of the t_1 beats in the rephasing and nonrephasing become overlapped. We find that the $t_1 = 0$ approximated by the pinhole scattering differs by ~50 fs from that of the maximum of the beatings.

Once $t_1 = 0$ is set, we select the single t_1 time used for the RASD scan that will maximize the signal-to-noise ratio by recording the inhomogeneous index over the t_1 scan (Fig. 2.2B). At early t_1 times, the inhomogeneous index has the form of the error function, and at latter t_1 times, the inhomogeneous index decays back to zero as the signal decays. Here, we maximize the signal-to-noise ratio of the RASD by selecting the

t_1 time with the largest inhomogeneous index magnitude. To demonstrate the t_2 time dependence of the inhomogeneous index, we plot the t_1-scanned inhomogeneous index at various t_2 times. Applying a low pass filter, we remove the inhomogeneous index high frequency oscillations, which will be discussed below. Note, comparing the t_1 of the maximum inhomogeneous index, t_1^{max}, for three different t_2 times, we find that the t_1^{max} time does not significantly change as a function of t_2.

Another consideration that can be used while selecting the single t_1 time is the ability to selectively excite the transition of interest[28]. The excitation probability is the product of the chromophore's absorption spectrum and the power spectrum of the first two pump pulses, which has frequency domain modulations due to the non-zero t_1 time delay.[29] Figures 2.3C-D demonstrate the t_1 time dependence of exciting the symmetric and asymmetric modes of CMT (Fig. 2.4). To quantify the ability to selectively excite a single transition, we define a contrast (G) of excitation between the symmetric and asymmetric modes as:

$$\Gamma_s = \frac{A_s - A_a}{A_s} \qquad (13) \qquad\qquad \Gamma_a = \frac{A_a - A_s}{A_a} \qquad (14)$$

where A_s and A_a are the probabilities of excitation integrated over the symmetric and asymmetric modes respectively at a given t_1 time (Fig. 2.3A-B). At later t_1 times, the magnitude of the contrast is more than an order of magnitude less than it is as early times, indicating the ability to selectively excite a specific transition is reduced. This loss of selectivity is due to the higher frequency of oscillations of the temporal streaking of the electric field's interference pattern in the later t_1 times (Fig. 2.3F) relative to early t_1 times (Fig. 2.3E), an effect that is largely independent of the details of the molecular

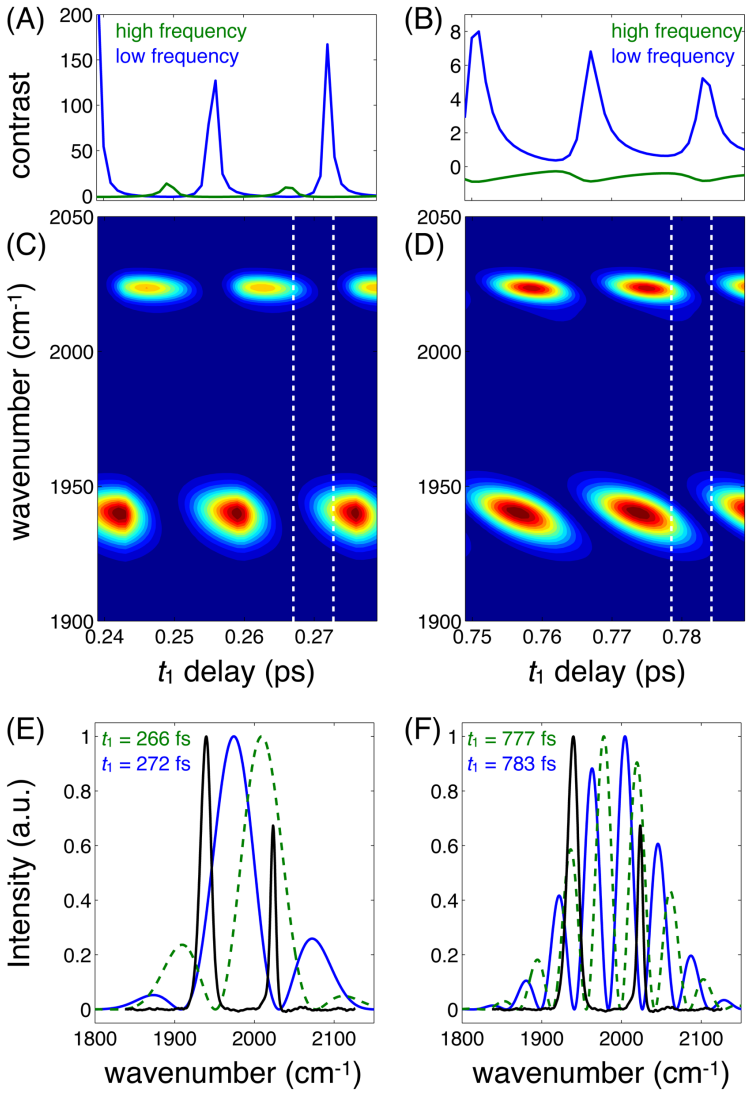

Figure 2.3 The probability of excitation (C, D) and the corresponding contrast for the asymmetric and symmetric modes of CMT (A , B). The interference pattern at given t_1 times, indicated by the dashed lines in (C), plotted against the linear absorption spectrum of CMT in butanol (E, F).

system or of the absorption linewidth.

2.5 Results and Discussion

2.5.1 Technique calibration. Cyclopentadienyl manganese tricarbonyl (CMT) is a well studied piano stool metal carbonyl complex. The carbonyls have three modes that are Raman and IR active while the linear spectrum consists of two bands (Fig. 2.4); the low

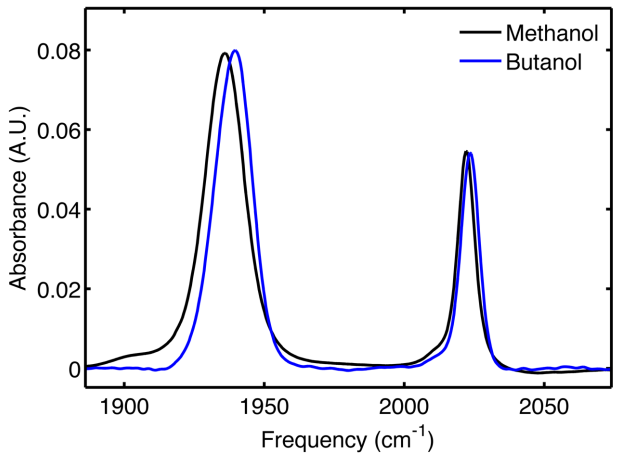

Figure 2.4 The linear FTIR spectra of $CpMn(CO)_3$ in methanol and butanol normalized to the symmetric band area.

frequency band is composed of two degenerate asymmetric stretches, and the high frequency band is a symmetric stretch that is blue shifted by ~80 cm^{-1}. Comparing the widths of the symmetric stretch bands, we see only a minimal solvent dependence, 8.07 and 8.14 cm^{-1} for methanol and butanol respectively, while the asymmetric band of methanol is slightly broader than that of butanol, 17.92 and 15.78 cm^{-1} respectively. Figure 2.5 shows the absorptive spectrum, which is the sum of the rephasing and nonrephasing spectrum, of the asymmetric stretch of CMT in methanol at two t_2 times of 0.25 ps and 5.0 ps. The ground state bleach (GSB) and stimulated emission (SE) band (red) arises from the 0-1 transitions, and the opposite-singed band (blue) is due to excited state absorption (ESA) into the anharmonically red-shifted second excited state. At early times, while the w_1 and w_3 frequencies are strongly correlated, the fundamental transition is somewhat elongated along the diagonal and the nodal line separating the GSB/SE and ESA bands is slanted; the anti-diagonal width of the fundamental transition arises from the homogeneous broadening. At latter times, when the ω_1 and w_3 frequencies have lost correlation due to spectral diffusion, the

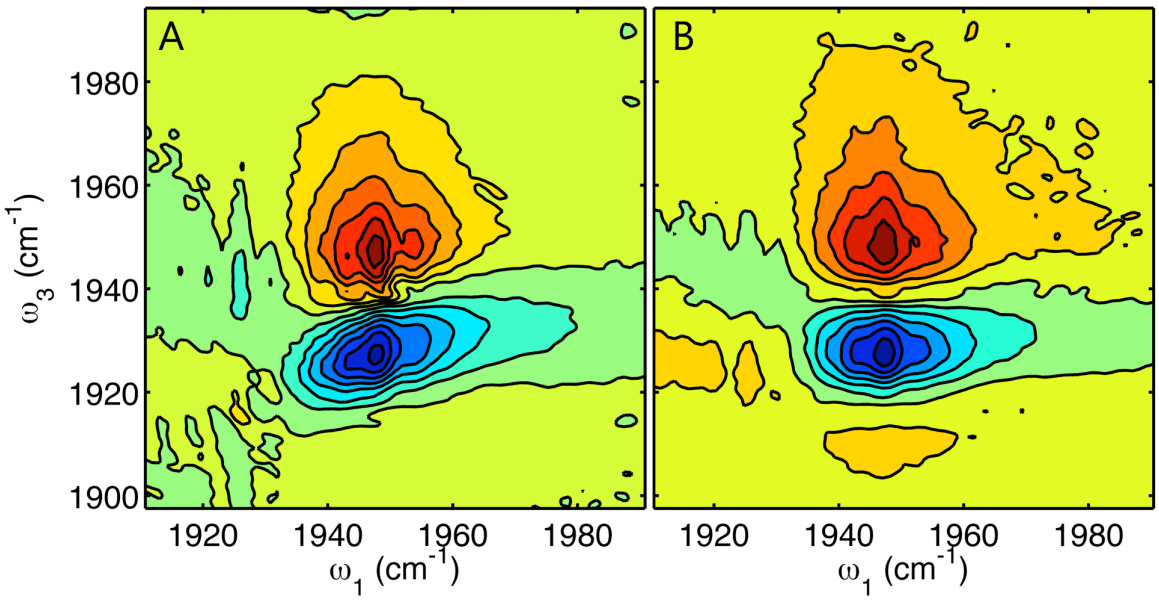

Figure 2.5 The absorptive spectrum of the asymmetric band of cyclopentyldienyl manganese tricarbonyl (CMT) in methanol at (A) t_2 = 0.25 ps and (B) t_2 = 5 ps. The fundamental peak is the positive going peak (red) while the first excited transition is negative going (blue). Changes in the spectroscopic features over t_2 arise from spectral diffusion.

fundamental band acquires a rounded shape while the nodal line is no longer slanted.

We measure the spectral diffusion of the asymmetric stretch of CMT in methanol and butanol using the 2DIR peak volume inhomogeneous index (Fig. 2.6). The time constant from a single-exponential fit to spectral diffusion in butanol yields 4.2±0.74 ps, which is more than twice that of the value in methanol, 1.86±0.13 ps. This pronounced difference is in stark contrast to the nearly identical spectral widths of the linear spectra, where the width of the asymmetric band only varies by about 12%. The linewidth in the linear spectrum is only a measure of the maximum frequency fluctuations, dw, available to the chromophore, but does not give any information on the number of microenvironments available to the chromophore or the timescales required to sample those microenvironments. Although there are often correlations between line shapes and spectra diffusion times, they can also be essentially uncoupled[30-34]. For example,

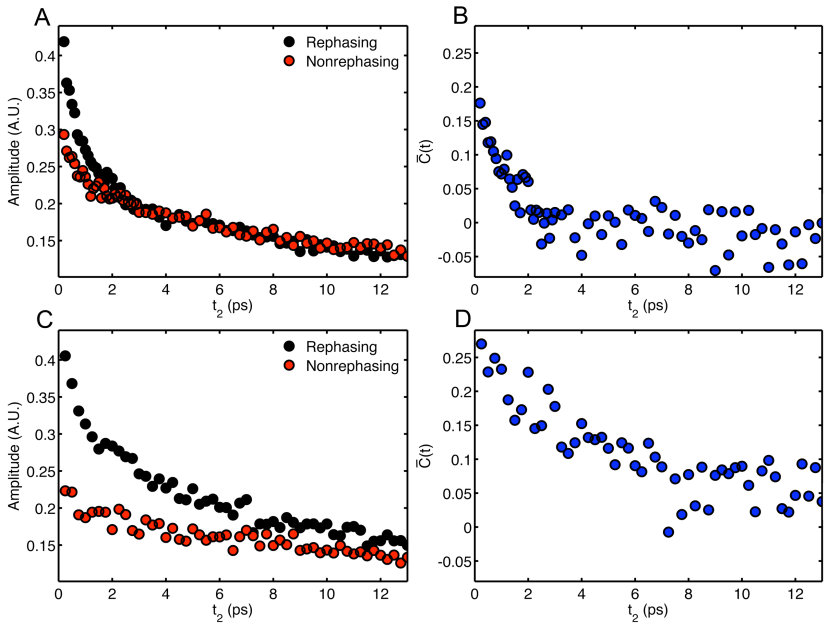

Figure 2.6 The peak volume of the rephasing and nonrephasing spectrum for CMT in (A) methanol and (C) butanol, with their corresponding computed FFCFs (B, D).

polar environments tend to amplify motional dynamics because solvent rearrangements map strongly to spectral fluctuations. An alcohol series study of a vibrational probe $Mn_2(CO)_{10}$ showed a clear correlation between viscosity and spectral diffusion times, with the inhomogeneous widths varying inversely with alcohol chain length, and hence with viscosity.[29] Though some contribution to the extracted inhomogeneous widths is likely due to the diversity of solvation environments, some contribution must also be due to the varying polarity, which induces larger changes in instantaneous vibrational frequency. Because polarity also decreases with increased chain length, it is certainly the case that our previous observation of alcohol-dependent inhomogeneous broadening contains a polarity contribution. In contrast to the inhomogeneous width, which is essentially a static property, spectral diffusion is inherently dynamical, and is decoupled from the magnitude of frequency fluctuations, since it is sensitive only to their time correlation function. The slower spectral diffusion of CMT in butanol relative

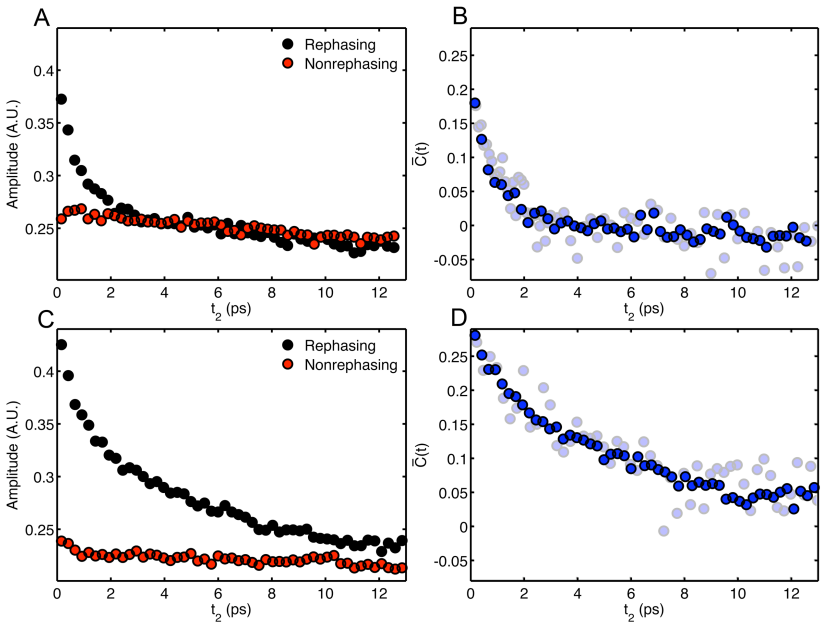

Figure 2.7 RASD acquired rephasing and nonrephasing signal, $E_s(t_3)$, of CMT in (A) methanol and (C) butanol, with their corresponding computed FFCFs (B, D); the opaque data points are the same as those in Fig. 6. Due to the large data set provided by RASD, this figure displays only 1 in 30 data points.

to that in methanol is therefore relatively unsurprising. Nevertheless, the insensitivity of the inhomogeneous width to solvent is noteworthy and emphasizes the limited dynamical information available from 1D spectra.

Utilizing the rapidly acquired spectral diffusion (RASD) method to measure the FFCF of CMT in methanol and butanol we see that, as expected, CMT solvation in methanol occurs much faster than does CMT in butanol (Fig. 2.7). The t_1 time delay values used for the methanol and butanol measurements are 786 and 768 fs respectively, where the delay was selected to maximize the signal to noise ratio. The time constants of single exponential fits in methanol and in butanol are 1.29 ± .04 ps and 5.49 ± .08 ps respectively. The RASD time constants of methanol and butanol compare favorably to those of the PVII with the largest discrepancy being that butanol measurements differ by ~30%. Nevertheless, visual inspection reveals the similarity of the extracted FFCF

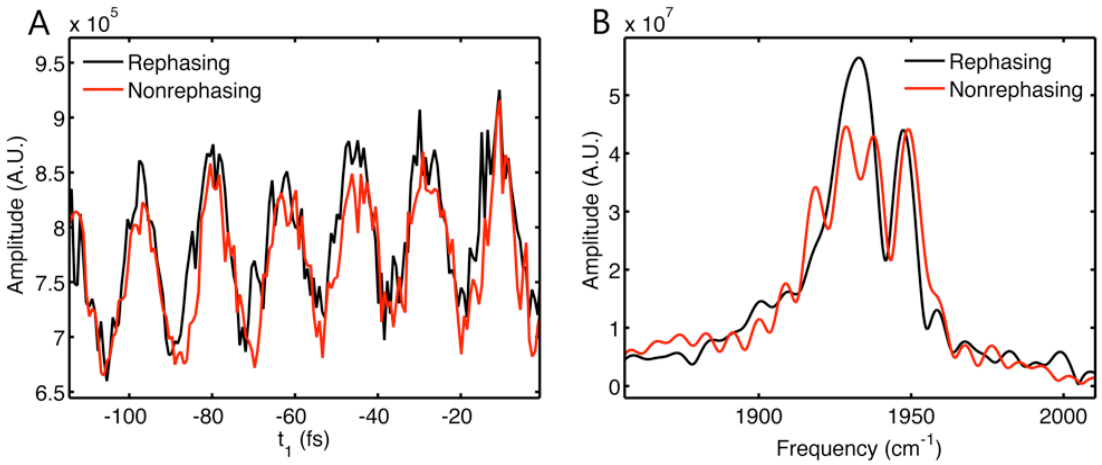

Figure 2.8 The t_1 time delay continuously scanned for both the rephasing and nonrephasing signal; note, this is the same data presented in figure 2, but over a shorter time interval (a), and their corresponding Fourier transforms.

values. Another noticeable difference between the PVII and RASD is the magnitude of the fit errors for the RASD being substantially smaller than that of PVII. This is due to the fact that the RASD data sets containing ~3500 data points that are averaged over 10 scans, where as the PVII data sets contain 60 data points without any averaging. The enlarged data sets of RASD gives additional confidence to the exponential fits and could allow the identification of subtle features of the FFCF that may be obscured by slow drift using the PVII.

2.5.2 Interference. An inference pattern in the frequency domain arises from the t_1 time delay, where the double-pulse field can either select or deselect the mode of interest. Due to the sensitivity of this interference pattern to the optical cycle, a t_1 difference of ~8 fs will modulate the selection of the vibrational mode of interest (Fig. 2.3).

The high frequency oscillations of the t_1 scan (Fig. 2.8) result from the interference patterns being imprinted onto the spectrum; the Fourier transform of these oscillations is the vibrational frequency of the asymmetric stretch of CMT, 1940 cm^{-1}.

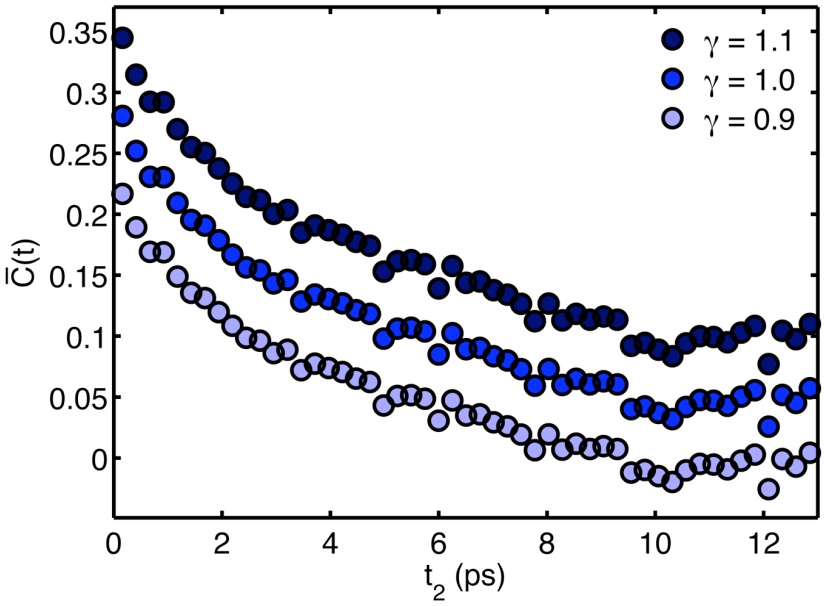

Figure 2.9 To test the impact that inaccurate rephasing and nonrephasing relative amplitudes has on the FFCF, we calculate the inhomogeneous index of CMT in butanol while scaling the rephasing signal amplitude by γ. We find that γ has little impact on the form of FFCF, but it does introduce a vertical offset.

Setting the t_1 value of the rephasing and nonrephasing by a difference of one half of an optical cycle, $\delta t_1 = 8\,fs$, will not change the form of the rephasing and nonrephasing but will cause the relative amplitudes to be incorrect. The impact of $dt_1 \neq 0$ is demonstrated by the large t_2 times in Figure 2.7B where the FFCF of CMT in methanol decay to a constant negative value. Because $\delta t_1 = 8\,fs$ will have little impact on the form of the response function, we can test the consequence of $\delta t_1 \neq 0$ by altering the relative amplitudes of the rephasing and nonrephasing data. Using the CMT/butanol results, we compare the RASD with different rephasing scaling factors, g:

$$II_\gamma = \frac{\gamma A_r - A_n}{\gamma A_r + A_n} \tag{24}$$

Comparing γ = 1.1, 1.0, and 0.9, shows that g has a dramatic impact on the vertical offset (Fig. 2.9), $\Delta_{1.1} = \langle II_{1.1} - II_{1.0} \rangle = -.0472$ and $\Delta_{0.9} = .052$, but has almost no effect on the form

of the decay. Adjusting for this vertical offset, the reduced *c*-squared, $\chi^2_\gamma = \sum \frac{\left(II_{1.0} - \left(II_\gamma - \Delta_\gamma\right)\right)^2}{\sigma^2}$, of both γ=1.1 and 0.9 are very small, less than 10^{-5}. If the inhomogeneous index at $t_2 = 0$ or at large t_2 times is previously known or if only the form of the spectral diffusion is desired, the inhomogeneous index can be adjusted numerically. Of course, there are many cases where a precise value of the long-time offset is meaningful, for instance in proteins and glasses[30] which exhibit dynamics over many time scales, and in those cases, care must be taken to set the delays properly. With the experimental methods used here, we set the t_1 delay to within 0.025 fs ($l/640$) allowing RASD to be used to measure dynamics of varying time scales.

2.6 Conclusion

Exploring the utility of the RASD approach to measuring spectral diffusion, we find that both the theoretical formalism and experimental comparisons suggest that RASD provides an accurate measure of the frequency-frequency correlation function, and is simply proportional to the FFCF scaled by $\frac{1}{t_1}\sqrt{\frac{2}{\langle \delta\omega^2 \rangle}}$. Experimentally, we have demonstrated that the spectral diffusion of cyclopentadienyl manganese tricarbonyl in methanol and butanol measured by PVII compared favorably to spectral diffusion measured by RASD with a single array detector, which requires the t_1 delay to be duplicated for the rephasing and nonrephasing. These experiments were achieved using a data acquisition and processing time of ~5 min, which compares very favorably with other reports of metal carbonyl spectral diffusion[35], while acquiring nearly 3 orders of magnitude more data points. In principle, the faster data acquisition of RASD allows

us to average multiple scans and measure subtle features of the FFCF that might be missed in the much slower, conventional approach based on recording the entire 2D-IR spectrum at each waiting time. We note that RASD is fully compatible with pulse-shaping based implementations of 2D spectroscopy, where the rephasing and nonrephasing signals can be obtained using phase cycling.[36] RASD will enable real-time studies of *changes* in molecular dynamics on chemical systems evolving on slow time scales, such as protein aggregation, or macromolecular gelation. Future work will be required to test the robustness of the RASD method, particularly under conditions where some of the commonly the applied approximations (short time and cumulant approximations) may prove to be inappropriate.

Acknowledgements

This work was supported by the National Science Foundation (CHE-0748501) and the Camille & Henry Dreyfus Foundation.

2.7 References

1. Joo, T. H.; Jia, Y. W.; Yu, J. Y.; Lang, M. J.; Fleming, G. R., "Third-order nonlinear time domain probes of solvation dynamics". *Journal of Chemical Physics* **1996,** *104* (16), 6089-6108.

2. Hamm, P.; Lim, M.; Hochstrasser, R. M., "Non-Markovian dynamics of the vibrations of ions in water from femtosecond infrared three-pulse photon echoes". *Physical Review Letters* **1998,** *81* (24), 5326-5329.

3. Piryatinski, A.; Skinner, J. L., "Determining vibrational solvation-correlation functions from three-pulse infrared photon echoes". *Journal Physical Chemistry B* **2002,** *106* (33), 8055-8063.

4. Hamm, P. a. Z., Martin, *Concepts and Methods of 2D Infrared Spectroscopy*. Cambridge University Press: 2011; p 286.

5. Ge, N. H.; Zanni, M. T.; Hochstrasser, R. M., "Effects of vibrational frequency correlations on two-dimensional infrared spectra". *Journal of Physical Chemistry A* **2002,** *106* (6), 962-972.

6. Khalil, M.; Demirdoven, N.; Tokmakoff, A., "Coherent 2D IR spectroscopy: Molecular structure and dynamics in solution". *Journal of Physical Chemistry A* **2003,** *107* (27), 5258-5279.

7. Khalil, M.; Demirdoven, N.; Tokmakoff, A., "Vibrational coherence transfer characterized with Fourier-transform 2D IR spectroscopy". *Journal of Chemical Physics* **2004,** *121* (1), 362-373.

8. Wang, J. P.; Chen, J. X.; Hochstrasser, R. M., "Local structure of beta-hairpin isotopomers by FTIR, 2D IR, and ab initio theory". *Journal Physical Chemistry B* **2006,** *110* (14), 7545-7555.

9. Fulmer, E. C.; Ding, F.; Zanni, M. T., "Heterodyned fifth-order 2D-IR spectroscopy of the azide ion in an ionic glass". *Journal of Chemical Physics* **2005,** *122* (3), 034302.

10. Piryatinski, A.; Lawrence, C. P.; Skinner, J. L., "Vibrational spectroscopy of HOD in liquid D2O. IV. Infrared two-pulse photon echoes". *Journal of Chemical Physics* **2003,** *118* (21), 9664-9671.

11. Kwak, K.; Park, S.; Finkelstein, I. J.; Fayer, M. D., "Frequency-frequency correlation functions and apodization in two-dimensional infrared vibrational echo spectroscopy: A new approach". *Journal of Chemical Physics* **2007,** *127* (12), 124503.

12. Lazonder, K.; Pshenichnikov, M. S.; Wiersma, D. A., "Easy interpretation of optical two-dimensional correlation spectra". *Optics Letters* **2006,** *31* (22), 3354-3356.

13. Lazonder, K.; Pshenichnikov, M. S.; Wiersma, D. A., "Two-dimensional optical correlation spectroscopy applied to liquid/glass dynamics". *Ultrafast Phenomena XV* **2007,** *88*, 356-358.

14. Asbury, J. B.; Steinel, T.; Stromberg, C.; Corcelli, S. A.; Lawrence, C. P.; Skinner, J. L.; Fayer, M. D., "Water dynamics: Vibrational echo correlation spectroscopy and comparison to molecular dynamics simulations". *Journal of Physical Chemistry A* **2004,** *108* (7), 1107-1119.

15. Mukamel, S., *Principles of Nonlinear Optical Spectroscopy*. Oxford University Press: 1995.

16. Roberts, S. T.; Loparo, J. J.; Tokmakoff, A., "Characterization of spectral diffusion from two-dimensional line shapes". *Journal of Chemical Physics* **2006,** *125* (8), 084502.

17. Park, S.; Park, J. S.; Joo, T., "Solvation Dynamics by Coherence Period Resolved Transient Grating". *Journal of Physical Chemistry A* **2011,** *115* (16), 3973-3979.

18. Kim, S.; Szyperski, T., "GFT NMR, a new approach to rapidly obtain precise high-dimensional NMR spectral information". *Journal of the American Chemical Society* **2003,** *125* (5), 1385-1393.

19. Szyperski, T.; Yeh, D. C.; Sukumaran, D. K.; Moseley, H. N. B.; Montelione, G. T., "Reduced-dimensionality NMR spectroscopy for high-throughput protein resonance assignment". *Proceedings of the National Academy of Science U. S. A.* **2002,** *99* (12), 8009-8014.

20. Bodenhausen, G.; Ernst, R. R., "The accordion experiment, a simple approach to 3-dimensional NMR-Spectroscopy". *Journal of Magnetic Resonance* **1981,** *45* (2), 367-373.

21. Nee, M. J.; Baiz, C. R.; Anna, J. M.; McCanne, R.; Kubarych, K. J., "Multilevel vibrational coherence transfer and wavepacket dynamics probed with multidimensional IR spectroscopy". *The Journal of chemical physics* **2008,** *129* (8), 084503.

22. Nee, M. J.; McCanne, R.; Kubarych, K. J.; Joffre, M., "Two-dimensional infrared spectroscopy detected by chirped pulse upconversion". *Optics Letters* **2007,** *32* (6), 713-715.

23. Schmidt, J. R.; Sundlass, N.; Skinner, J. L., "Line shapes and photon echoes within a generalized Kubo model". *Chemical Physics Letters* **2003,** *378* (5-6), 559-566.

24. Kubo, R.; Schuler, K. E., "A Stochastic Theory of Line Shape". *Advances in Chemical Physics* **1969,** *15*.

25. Kwac, K.; Cho, M., "Two-color pump-probe spectroscopies of two- and three-level systems: 2-dimensional line shapes and solvation dynamics". *Journal of Physical Chemistry A* **2003,** *107* (31), 5903-5912.

26. Supplemental Information.

27. Backus, E. H. G.; Garrett-Roe, S.; Hamm, P., "Phasing problem of heterodyne-detected two-dimensional infrared spectroscopy". *Optics Letters* **2008,** *33* (22), 2665-2667.

28. Baumberg, J. J.; Heberle, A. P.; Kohler, K.; Kavokin, A. V., "Ultrafast coherent carrier control in quantum wells". *Physica Status Solidi B-Basic Research* **1997,** *204* (1), 9-15.

29. Jefferson, C. M.; Meixner, A. J., "Frequency-Domain measuremens of spectral hole patterns burned with phase-coherent pulses". *Chemical Physics Letters* **1992,** *189* (1), 60-66.

30. King, J. T.; Baiz, C. R.; Kubarych, K. J., "Solvent-Dependent Spectral Diffusion in a Hydrogen Bonded "Vibrational Aggregate"". *Journal of Physical Chemistry A* **2010,** *114* (39), 10590-10604.

31. King, J. T.; Ross, M. R.; Kubarych, K. J., "Ultrafast alpha-Like Relaxation of a Fragile Glass-Forming Liquid Measured Using Two-Dimensional Infrared Spectroscopy". *Physical Review Letters* **2012,** *108* (15), *157401*.

32. Deak, J. C.; Rhea, S. T.; Iwaki, L. K.; Dlott, D. D., "Vibrational energy relaxation and spectral diffusion in water and deuterated water". *Journal of Physical Chemistry A* **2000,** *104* (21), 4866-4875.

33. Eaves, J. D.; Loparo, J. J.; Fecko, C. J.; Roberts, S. T.; Tokmakoff, A.; Geissler, P. L., "Hydrogen bonds in liquid water are broken only fleetingly". *Proceedings of the National Academy of Science U. S. A.* **2005,** *102* (37), 13019-13022.

34. Zheng, J. R.; Kwak, K.; Asbury, J.; Chen, X.; Piletic, I. R.; Fayer, M. D., "Ultrafast dynamics of solute-solvent complexation observed at thermal equilibrium in real time". *Science* **2005,** *309* (5739), 1338-1343.

35. Myers, J. A.; Lewis, K. L. M.; Tekavec, P. F.; Ogilvie, J. P., "Two Color Two Dimensional Fourier Transform Electronic Spectroscopy With a Pulse Shaper". Optics Express **2008**, 16, 17420-17428

36. Kumar, S. K.; Tamimi, A.; Fayer, M. D. "Comparisons of 2D IR measured spectral diffusion in rotating frames using pulse shaping and in the stationary frame using the standard method". *Journal of Chemical Physics* **2012,** 137, 184201

Chapter Three

Developing Accelerated Spectroscopic Techniques: Compressed Sensing

The work of this chapter was possible with the help of:

Josef A. Dunbar

3.1 Introduction

The data analysis techniques in a diverse group of fields—including magnetic resonance imaging in medicine[1-3], image processing[4, 5], astronomy[6], and genomics[7, 8]—have recently been revolutionized due to the introduction of the compressed sensing method (CS)[9]. In contrast to conventional Fourier transform based algorithms that convert, for example, time domain signals into the frequency domain making no assumptions about the transformed signals, compressed sensing explicitly enforces sparsity on the transformed signal. A system of linear equations that is underdetermined is known to have multiple solutions; of those solutions, the sparse solution has a maximum number of negligibly small coefficients. If the desired solution

is known to be sparse, the number of measurements required to accurately determine the solution can be greatly reduced. Since many spectroscopic methods are primarily concerned with determinations of peak positions and amplitudes, including in ultrafast, multidimensional applications, compressed sensing has the potential to accelerate data acquisition by orders of magnitude over conventional Fourier transform-based approaches.

CS has proven to be a valuable method to reduce the time required for both experimental and computational techniques[10-13]. These experiments use CS to numerically calculate the Fourier coefficients from the time domain data in lieu of the commonly used fast Fourier transform (FT). With the use of CS, the number of experimentally measured data points in the time domain can be greatly reduced while maintaining a high level of spectral resolution and signal to noise ratio. Two-dimensional infrared (2DIR) spectroscopy is ideally suited to the use of CS.

2DIR is a four wave mixing experiment as represented in **Fig. 3.1**; the first three fields (E_1, E_2, and E_3) interact resonantly with vibrational transitions within the pulse bandwidth, generating a signal field, $E_s(t_1, t_2, t_3)$, that is experimentally measured in the frequency domain using spectral interferometry. The experiment is broken up into three time periods (denoted t_1, t_2, and t_3), where t_1 and t_3 are conjugate to the frequencies ω_1 and ω_3, respectively, and t_2 is the waiting time between them (**Fig. 3.1**). Changes in the 2DIR spectra as a function of t_2 yield a variety of molecular dynamical information on the picosecond time scale including chemical exchange (i.e. equilibrium reactions)[14-17], spectral diffusion due to intermediate timescale frequency fluctuations[18, 19],

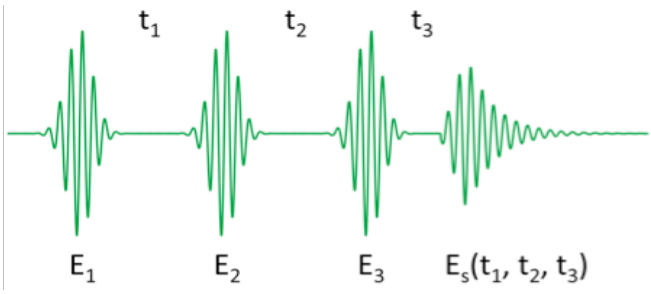

Figure 3.1 The pulse sequence of 2DIR separated by the three time delays t_1, t_2, and t_3.

intramolecular vibrational energy redistribution[20, 21], vibrational relaxation[22], and coherent wave packet motion[23]. In conventional experiments that fully sample the coherence times (t_1 and t_3) these molecular dynamical properties can be extracted by measuring t_2-dependent peak amplitudes by integrating over appropriate regions of the 2D spectra. Here, we will refer to this experimental and analytical approach as "t_2 dependent peak volume analysis."

The most common implementation of 2D spectroscopy based on the three-pulse echo sequence involves the measurement of numerous t_1 delays. Although it depends on the inherent spectral line widths, for narrow band IR transitions, a reasonable maximum t_1 delay would be ~10 ps, resulting in ~14000 data points with typically oversampled points, though certainly less oversampling is feasible. Using conventional Fourier transformation, such a data set would provide 3 cm^{-1} resolution, and in our implementation, which uses continuously scanned time delays and a 1-kHz laser system, one 2D spectrum requires 15 seconds. It is this scanning process that limits the time to acquire a full set of t_2-dependent 2DIR spectra. CS offers a method to reduce the number of t_1 time points dramatically, where the maximum delay may be less than 500 fs, sampled with fewer than 500 data points while still effectively measuring the full

2DIR spectrum. Here, using the well characterized dicarbonyl-acetylacetonato-rhodium(I), or rhodium dicarbonyl (RDC)[15, 24, 25] (**Fig. 3.2**), we explore the robustness of the CS method. First, we show that the key features of the two dimensional spectrum of RDC can be largely reproduced using a t_1 range that extends to just 2% of that using traditional methods, while maintaining the ability to reproduce accurately t_2 dependent peak volume spectral features, including the coherent quantum beats. Additionally, we explore the limitations of the CS method in measuring spectra where there is a large dynamic range of spectral amplitude, as well as detailing the impact on spectral widths caused by choices of the input parameters to the CS method.

3.2. Theory

Consider the simple equation $\mathbf{A} \bullet \mathbf{x} = \mathbf{b}$ where **b** is a vector of length N, **x** is a vector of length M, and **A** is an N x M matrix. When **x** is unknown and $N < M$, $\mathbf{A} \bullet \mathbf{x} = \mathbf{b}$ is an underdetermined system allowing for multiple solutions of **x**. Compressed sensing algorithms assume that the desired solution of **x** is a sparse solution, where sparsity is defined as the solution with a maximal number of negligibly small coefficients of the vector **x**. Utilizing CS to compute the Fourier transform is a subset of compressed sensing and requires the matrix **A** to act as a transformation between two orthogonal bases. The discrete Fourier transform (DFT) matrix does this by casting the Fourier transform as a spectral decomposition problem[26].

Briefly, the Fourier transform of $f(t)$ is defined as

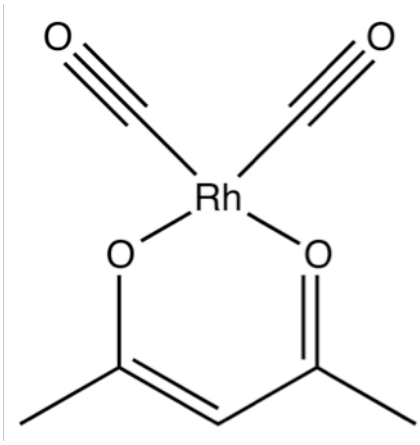

Figure 3.2 RDC is a metal carbonyl complex with two IR active modes at 2015cm^{-1}, the antisymmetric stretch, and at 2084cm^{-1}, the symmetric stretch. The two carbonyls units are an example of an excitonically coupled dimer of vibrations.

$$g(\omega) = \int_{-\infty}^{\infty} f(t) e^{-it\omega} dt \tag{1}$$

At a single frequency, w_0, the Fourier transform, $g(w_0)$, becomes the inner product between the two functions $f(t)$ and $\exp(-it\omega_0)$. If $f(t)$ is discrete and finite in time, the Fourier transform at a single frequency becomes

$$g(\omega_0) = \sum_{\tau_i}^{\tau_f} f(t) e^{-it\omega_0} \Delta t \tag{2}$$

Now, if we introduce multiple frequencies and the frequency space is also discrete and finite, the Fourier transform becomes a matrix multiplication problem, $\mathbf{F}_{jk}f(t)$, where the coefficients of $\mathbf{F}_{jk}$ can be represented as:

$$\mathbf{F}_{ij} = e^{-it_i\omega_j} \Delta t \Delta\omega \tag{3}$$

The DFT matrix is a well-developed and elegantly derived case of $\mathbf{F}_{jk}$,[27] requiring that $\mathbf{F}_{ij}$ be square and that both t_i and ω_i be evenly spaced.

Here, we take **x** to represent the observed signal in the time domain of length *N*,

b is the unknown of length M, and **A** is a region of the (DFT) matrix such that the size of **A** is *N* x *M*. When the DFT matrix is used to calculate the Fourier transform without using compressed sensing, the DFT matrix must be square and the Δt and t_{max} of the experimentally measured data are linked to the $\Delta\omega$ and ω_{max} of the Fourier transform. Because compressed sensing only uses a region of the DFT matrix, there is no longer an enforced mapping from Δt and t_{max} to Δw and ω_{max}, allowing one to arbitrarily choose $\Delta\omega$.

The basis pursuit problem (BP)[28] is used to search for the sparse solution of **x** by minimizing $\|\mathbf{x}\|_1$, where $\|\mathbf{x}\|_n$ is defined as $\|\mathbf{x}\|_n = \sum_{i=1}^{j} |x_i|^n$, subject to $\mathbf{A} \bullet \mathbf{x} = \mathbf{b}$. When noise is introduced to **b**, as is the case of our measured data, for example, the basis pursuit denoising (BPDN)[28] is preferable such that the minimization of $\|\mathbf{x}\|_1$ is subject to the relaxed condition of $\|\mathbf{A} \bullet \mathbf{x} - \mathbf{b}\|_2 \leq \sigma$, where s is related to the signal to noise ratio of **b**.

3.3 Methods and Experimental Setup

3.3.1. 2DIR setup. Our implementation of 2D-IR spectroscopy has been detailed previously[29-31]. Briefly, the fields E_1, E_2, and E_3 are 100 fs infrared pulses generated by a white light seeded b-barium borate optical parametric amplifier (OPA) and followed by a difference frequency generation (DFG). The signal, $E_s(t_1, t_2, t_3)$, is made collinear with a slightly delayed reference pulse. We upconvert the $E_s(t_1, t_2, t_3)$ signal and reference pulse to the visible using sum-frequency generation with a chirped 800-nm pulse in a MgO:$LiNbO_3$ crystal and the resulting visible light is subsequently spectrally resolved

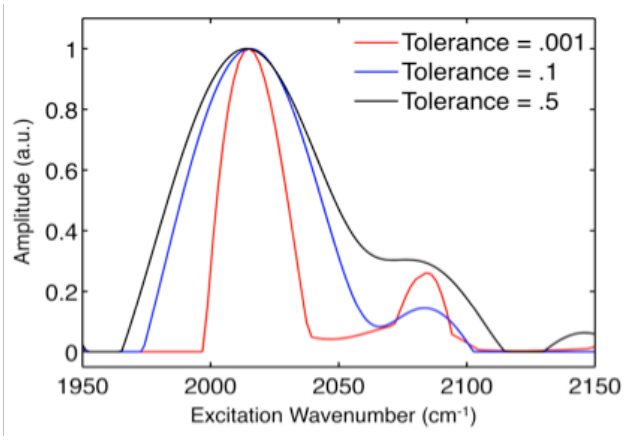

Figure 3.3 The minimization tolerance of $||b||_1$ can be thought of as the sparsity tolerance; as the tolerance is increased, the widths are also correspondingly increased.

with a 0.5-m spectrograph (1200 grooves/mm grating) and digitized with a 1340x100 pixel CCD camera synchronized to the laser at 1 kHz. The t_1 delay stage is scanned continuously using an optically encoded (7 nm resolution) DC motor moving one of a pair of 7° apex ZnSe wedges.

3.3.2. Sample preparation. RDC was purchased from Sigma Aldrich and was used as received. Samples were prepared to be ~8 mM and filtered before use. The sample cell consisted of a 100 mm Teflon spacer sandwiched between two 3 mm thick and 25 mm diameter calcium fluoride windows.

3.3.3. Data acquisition. The geometry of the incoming pulses is such that the acquired data is the rephasing signal. The data was collected at room temperature. The t_2 time steps range from -.3 to 99.5 ps at varying time steps: -0.3 to 5 ps – 0.1 ps time steps; 5.5 to 10.5 ps – 0.5 ps times steps; 11.5 to 51.5 ps – 1.0 ps time steps; and 53 to 99.5 ps – 1.5 ps delays. To avoid drifting over the course of the experiment, the t_2 delays were measured in a non-sequential order. At each t_2 time delay, t_1 was varied from -.5 to ~9ps in ~12000 steps of approximately equal size; using linear interpolation during the data

analysis, t_1 time steps were adjusted to be exactly evenly spaced. The t_1 axis is calibrated using interferometry as described elsewhere.

3.3.4. Compressed sensing. If not otherwise indicated, the CS method was used for the $E_s(t_1, t_2, \omega_3)$ data over t_1 time ranging between 190.7 fs to 497.3 fs. For all data, σ was given a value of 0.03. The minimization tolerance of the BPDN algorithm can be thought of as measure of the "tolerable" sparsity. Comparing the spectra of multiple minimization tolerances (**Fig. 3.3**), normalized to the asymmetric stretch peak maximum, we see at larger values of minimization tolerance, the features broaden. Despite having a two orders of magnitude difference, the difference between the σ = 0.001 and σ = 0.1 spectra is comparable to the difference between the σ = 0.1 and σ = 0.5, a factor of five difference suggesting that lowering the minimization tolerance has a diminishing return on decreasing the sparsity. Although lowering the tolerance narrows the spectral widths, as the tolerance level is decreased, the computational iterations of the CS method dramatically increase; therefore, the minimization tolerance needs to be chosen with care. The 2DIR data presented here have a minimization tolerance of 0.001.

Because the two dimensional spectra require a Fourier transform over multiple ω_3 frequencies that require the relative amplitudes of the spectrum to be preserved, we divide $E_s(t_1, t_2, w_3)$ by $|| E_s(t_1, t_2, w_3) ||_2$ prior to CS analysis and multiply $E_s(w_1, t_2, w_3)$ by $|| E_s(t_1, t_2, w_3) ||_2$ after the CS analysis.

Solving the BPDN problem as described above is not a trivial problem. Here, we rely on the spectral projected gradient for 1-norm minimization algorithm (SPGL1)

developed by Van Den Berg and Friedlander[32]. Because the CS method requires hundreds of matrix multiplications, relative to the fast Fourier transform the SPGL1 algorithm is computationally slow. For the t_2 time data presented here, the 2DIR spectra was only produced over the w_3 region of interest, 2007 to 2020 cm^{-1}. The CS method is known to shift the peak maximum[10]; therefore, for ease of analysis, the w_1 axis is shifted and scaled so that asymmetric band is centered at 2015 cm^{-1} and the symmetric band at 2084 cm^{-1}.

3.4 Results and Discussion

To test the utility of CS we first compare the full 2DIR spectrum of RDC at a waiting time of 400fs computed with a discrete FT (**Fig. 3.4a**) and CS (**Fig. 3.4b**). We see that the CS method is capable of reproducing all of the peaks in the RDC spectrum, including both diagonal peaks, their corresponding cross peaks, and the four peaks that arise from anharmonically-shifted excited state absorption. It is also of note that the relative amplitudes of the peaks appear to be consistent between the two methods (relative peak amplitudes will be discussed further below). Because the CS method only computes the Fourier transform over ω_1, and ω_3 is determined by the spectrometer, it is not surprising that spectral differences along ω_3 are negligible. Along ω_1 we see that spectral widths of the CS method are distinctly larger than those in the FT spectrum. Because the line shapes reflect the complete t_1 dephasing time, it is not surprising that the CS method lacks the capability of reproducing the w_1 line shape. Additionally, we see that the cross peak at ω_3 = 2015 cm^{-1} and ω_1 = 2084 cm^{-1} is shifted by 20 cm^{-1} to the red. The ability of

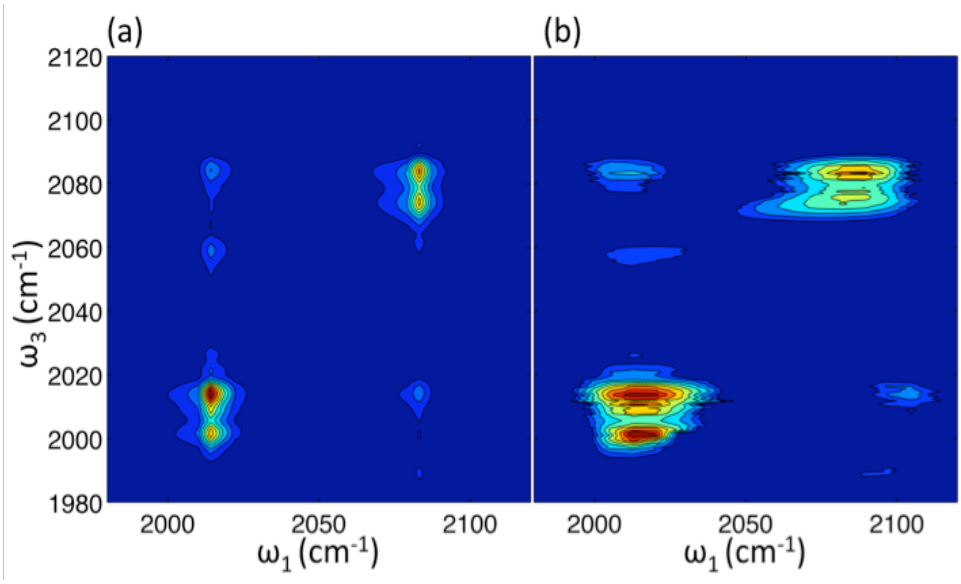

Figure 3.4 The 2DIR spectrum of RDC in hexane at a waiting time of t_2 = 400fs where the Fourier coefficients along the ω_1 axis are calculated using a FT (a) and CS (b).

CS to accurately determine the center peak position has been discussed elsewhere and was found to reflect the length of the t_1 time interval[10].

To better understand how CS distorts the spectrum, we compare the CS method over a 307 fs t_1 interval to a FT over the full dephasing time along w_1 at a single detection frequency, ω_3 = 2015 cm^{-1} (**Fig. 3.5**). The units are arbitrary and thus we normalize the spectra to the antisymmetric peak maximum. The discrepancy in line shape as seen in **Fig. 3.4** is better viewed here; the asymmetric peak FWHM from CS is more than triple the width from FT. Again, this is expected because the FWHM of a homogeneously broadened spectrum, as is RDC in hexane, is dependent on the t_1 dephasing time, but the CS analysis here only has knowledge of 307 fs of the t_1 dephasing time. A plot of the FT of the brief 307 fs t_1 interval consists of a single broad band that is significantly red shifted, and hardly resembles the FT of the full t_1 dephasing time of the CS spectrum. Although CS reproduces the general form of the FT

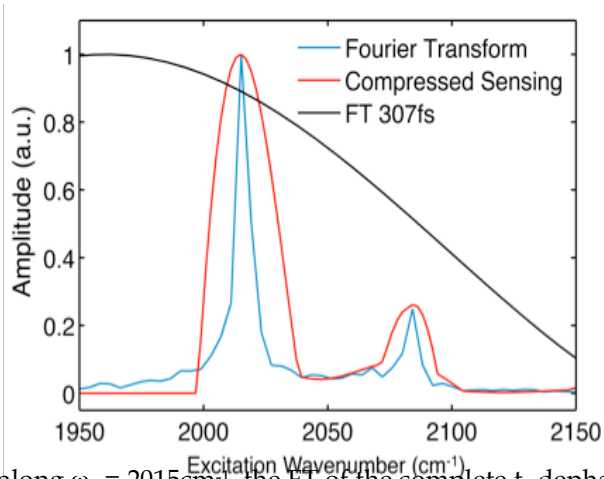

Figure 3.5 At the slice along ω_3 = 2015cm^{-1}, the FT of the complete t_1 dephasing time is compared against CS of a brief 307fs t_1 interval and the FT of the same 307fs t_1 interval.

spectrum, we find that the dynamic range of the CS method is dependent on the length of t_1 interval.

Comparing the peak maximum of the CS method and the full FT, we see that the ratio of asymmetric to symmetric peak maximum of the full FT is close to the CS method (4.02 and 3.83 respectively). Because we are also interested in reproducing the t_2 dependent peak volume analysis with CS, reproducing the relative peak amplitudes is critical. To test the robustness of the CS method, we compute the spectrum of RDC with three different t_1 time intervals (**Fig. 3.6**). As before, we normalize the spectra to the asymmetric stretch peak maximum. As the t_1 time interval is reduced from 307 to 153 to 77 fs, we see the inability of the CS method to accurately reproduce the relative peak amplitude of the symmetric stretch suggesting that the dynamic range of the CS method is dependent upon the length of the t_1 interval. The impact that the dynamic range has on t_2 dependent peak volume analysis will be discussed below.

The t_2 dependent peak volume analysis using CS over the 307 fs t_1 interval compares favorably to the corresponding FT calculated peak volume analysis. The

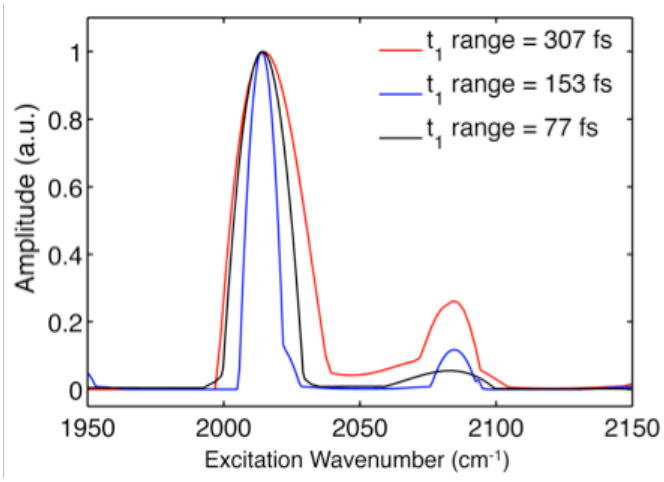

Figure 3.6 The Fourier coefficients calculated with CS with multiple t_1 interval lengths. As the t_1 interval is decreased, the dynamic range is correspondingly decreased suggesting that the dynamic range of CS is dependent on the t_1 interval length.

diagonal peak of the homogeneously broadened RDC includes contributions from orientational relaxation, vibrational energy redistribution and vibrational relaxation. Comparing CS and FT, the diagonal peak of the CS method is indistinguishable from that of the FT, with no noticeable difference in the signal-to-noise ratios between the two methods (**Fig. 3.7(a)**). The ability of CS to reproduce the diagonal peak waiting time dynamics demonstrates that that spectral diffusion, using the inhomogeneous index, can be measured with CS. Because the inhomogeneous index utilizes the difference in amplitude between the rephasing and nonrephasing signal, the t_1 interval must span a time where the nonrephasing signal is given ample time to dephase.

For RDC in hexane, the cross peak t_2 dependence measures IVR between the symmetric and asymmetric transitions. Here, we are measuring the rephasing signal where the cross peak contains oscillations that arise from a vibrational coherence between the excited symmetric and asymmetric states during t_2. The oscillations are at a frequency equal to the difference between the symmetric and antisymmetric

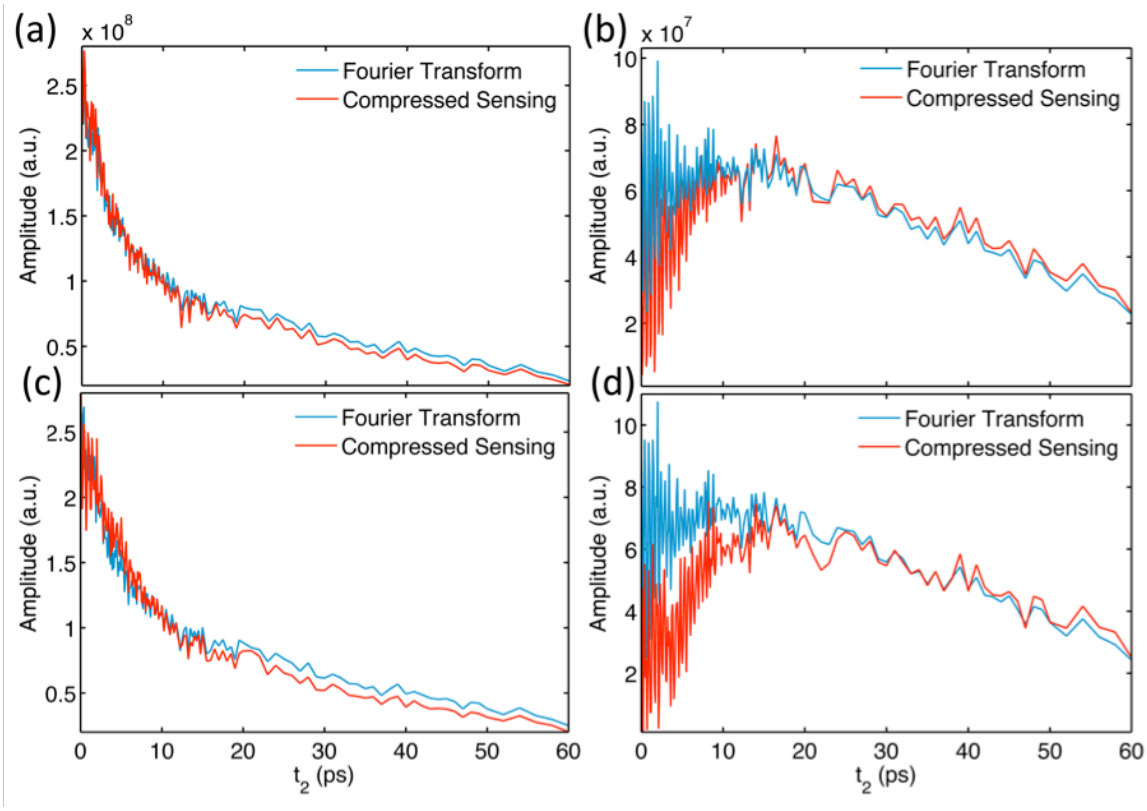

Figure 3.7 The CS and FT t_2 dependent peak volumes with two different t_1 interval length, 307fs (a&b) and 171fs (c&d). (a) and (c) are the t_2 dependent peak volumes of the asymmetric diagonal peak, and (b) and (d) are of the cross peak at 2015 and 2084cm^{-1}.

frequencies, 69 cm^{-1}. Although the cross peak t_2 dependence of the CS method follows a similar trend to the FT, there are noticeable differences (**Fig. 3.7(b)**). At the maxima of the coherence oscillations, the CS and FT methods compare favorably, but at the minima of the coherence oscillations the CS peak volume are significantly lower than those of the FT. This deviation arises due to the t_1-duration dependence of the CS method's spectral amplitude dynamic range. If the length of the t_1 interval is decreased to 171 fs the dynamic range is decreased as well, manifested as incorrectly small cross peak volume amplitudes (**Fig. 3.7(c)**) at early t_2. Because a decrease in the t_1 interval only changes the dynamic range, the dominant diagonal peak is largely unchanged (**Fig. 3.7(d)**). If CS is to be used to measure dynamic cross peak volumes for both IVR, as

we

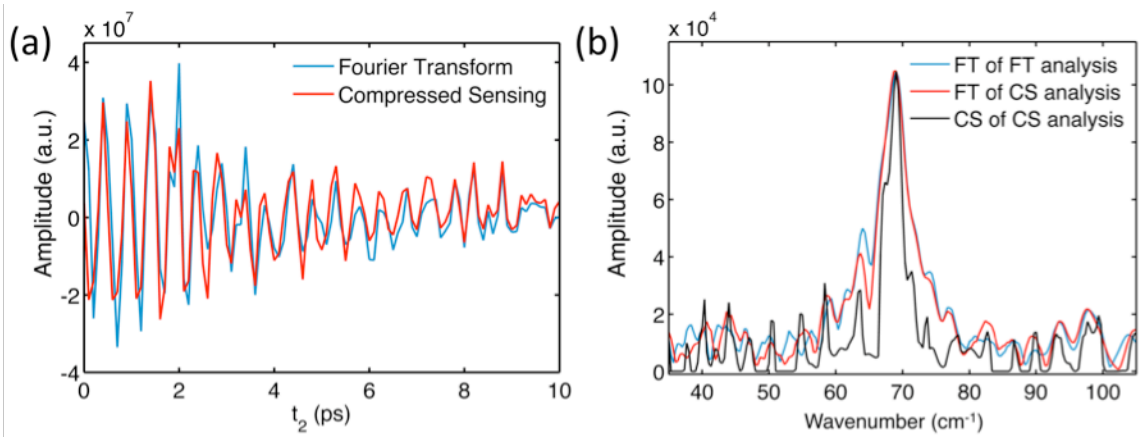

Figure 3.8 (a) The coherent oscillations are isolated from the peak volumes in **Fig. 3.7(b)** by subtracting off a simple biexponential fit and (b) the corresponding Fourier coefficients of these oscillations calculated with a discrete Fourier transform and compressed sensing.

demonstrated here, or chemical exchange, a careful selection of the t_1 interval length is required to avoid dynamic range induced distortions. Possibly, if one seeks to extract trends, rather than precise values of cross peak t_2 growth over a series of some other parameters such as solvent or temperature, the dynamic range distortions would be consistent through out the series, though not if line shapes change dramatically.

Despite distorting the minima of the coherent oscillations, we see only subtle differences between the CS and FT oscillations when a simple biexponential fit is subtracted from both (**Fig. 3.8(a)**). The corresponding Fourier transform of these oscillations are very similar; the signal-to-noise ratios, center peak locations at 69 cm^{-1}, and peak widths are all nearly identical (**Fig. 3.8(b)**). If artifacts from the limited dynamic range remained after subtracting the biexponential fit, one might expect a ringing in the frequency domain, which is absent in the spectra. Compressed sensing can again be used to numerically determine the Fourier coefficients of the coherence oscillations. The Fourier coefficients of the CS coherent oscillations calculated with a

discrete Fourier transform were duplicated using 15% of the t_2 waiting time with compressed sensing[33]. The reduction of the t_2 waiting time required to accurately measure the coherent oscillations again reduces the required experimental acquisition time.

3.5. Conclusion

We have explored the ability of compressed sensing (CS) to reproduce the fast Fourier transform (FT) 2DIR spectra and t_2 dependent peak volume analysis of those spectra. We found that CS is capable of accurately reproducing a 2DIR spectrum with only minor modifications to the spectroscopic features, and the CS t_2 dependent peak volume analysis closely mimics that of FT. The differences of the 2DIR spectrum of the FT and CS are most prevalent along ω_1, where the widths of CS spectra are noticeably larger than those of the direct FT spectra. Although distortions of the line shape are expected, the line shape is a product of the full t_1 dephasing time and CS only uses a brief interval of the dephasing time, the distortions limit the utility of CS in performing 2DIR line shape analysis. However, the t_2 dependent peak volume analysis with CS shows great promise. Waiting time dependent peak volumes determined with FT and CS spectra yield only minimal changes to the form and no noticeable changes to the signal-to-noise ratios. We also find that the dynamic range can be increased by increasing the t_1 interval length. These findings suggest that with the use of CS, t_2 dependent peak volume experiments—including vibrational lifetime, spectral diffusion, IVR, chemical exchange, and coherent oscillations—can be accurately measured despite

the t_1 interval length being reduced by nearly two orders of magnitude. For the example system described here, the total laboratory time required to record the 189 2D-IR spectra was 150 minutes. Had compressed sensing been used, it would have been possible to obtain the dynamical information contained in the waiting time dependent peak amplitudes in less than 10 minutes. Finally, we note that there is nothing specific or idiosyncratic about RDC, which has strong narrow spectral features, since any 2DIR experiment can, in principle, be accelerated by compressed sensing, provided one does not need perfect spectral line shapes. Nevertheless, it should be possible to extract spectral diffusion and inhomogeneous line widths using the inhomogeneity index method[18, 34], where only integrated peak volumes of rephasing and nonrephasing spectra are needed.

Acknowledgements

This work was supported by the National Science Foundation (CHE-0748501), and the Camille & Henry Dreyfus Foundation.

References

1. Chen, G.-H.; Tang, J.; Leng, S., "Prior image constrained compressed sensing (PICCS): A method to accurately reconstruct dynamic CT images from highly undersampled projection data sets". *Medical Physics* **2008,** *35* (2).

2. Lustig, M.; Donoho, D.; Pauly, J. M., "Sparse MRI: The application of compressed sensing for rapid MR imaging". *Magnetic Resonance in Medicine* **2007,** *58* (6).

3. Goldstein, T.; Osher, S., "The Split Bregman Method for L1-Regularized Problems". *Siam Journal on Imaging Sciences* **2009,** *2* (2).

4. Duarte, M. F.; Davenport, M. A.; Takhar, D.; Laska, J. N.; Sun, T.; Kelly, K. F.; Baraniuk, R. G., "Single-pixel imaging via compressive sampling". *Ieee Signal Processing Magazine* **2008,** *25* (2).

5. Wright, J.; Yang, A. Y.; Ganesh, A.; Sastry, S. S.; Ma, Y., "Robust Face Recognition via Sparse Representation". *IEEE Transactions on Pattern Analytical Machine Intelligence* **2009,** *31* (2), 210-227.

6. Bobin, J.; Starck, J.-L.; Ottensamer, R., "Compressed Sensing in Astronomy". *IEEE Journal of Selected Topics in Signal Processing* **2008,** *2* (5).

7. Amir, A.; Zuk, O., "Bacterial Community Reconstruction Using Compressed Sensing". *Journal Computational Biology* **2011,** *18* (11), 1723-1741.

8. Erlich, Y.; Gordon, A.; Brand, M.; Hannon, G. J.; Mitra, P. P., "Compressed Genotyping". *IEEE Transactions on Information Theory* **2010,** *56* (2).

9. Donoho, D. L., "Compressed sensing". *IEEE Transactions on Information Theory* **2006,** *52* (4).

10. Andrade, X.; Sanders, J. N.; Aspuru-Guzik, A., "Application of compressed sensing to the simulation of atomic systems". *Proceedings of the National Academy of Science U. S. A.* **2012,** *109* (35).

11. Holland, D. J.; Bostock, M. J.; Gladden, L. F.; Nietlispach, D., "Fast Multidimensional NMR Spectroscopy Using Compressed Sensing". *Angew. Chem.-Int. Edit.* **2011,** *50* (29), 6548-6551.

12. Kazimierczuk, K.; Orekhov, V. Y., "Accelerated NMR Spectroscopy by Using Compressed Sensing". *Angew. Chem.-Int. Edit.* **2011,** *50* (24), 5556-5559.

13. Sanders, J. N.; Saikin, S. K.; Mostame, S.; Andrade, X.; Widom, J. R.; Marcus, A. H.; Aspuru-Guzik, A. n., "Compressed Sensing for Multidimensional Spectroscopy Experiments". *The Journal of Physical Chemistry Letters* **2012,** *3* (18), 2697-2702.

14. Anna, J. M.; King, J. T.; Kubarych, K. J., "Multiple Structures and Dynamics of CpRu(CO)(2) (2) and CpFe(CO)(2) (2) in Solution Revealed with Two-Dimensional Infrared Spectroscopy". *Inorganic Chemistry* **2011,** *50* (19), 9273-9283.

15. Anna, J. M.; Kubarych, K. J., "Watching solvent friction impede ultrafast barrier crossings: A direct test of Kramers theory". *Journal of Chemical Physics* **2010,** *133* (17), 174506.

16. Anna, J. M.; Ross, M. R.; Kubarych, K. J., "Dissecting Enthalpic and Entropic Barriers to Ultrafast Equilibrium Isomerization of a Flexible Molecule Using 2DIR Chemical Exchange Spectroscopy". *Journal of Physical Chemistry A* **2009,** *113* (24), 6544-6547.

17. Zheng, J. R.; Kwak, K.; Asbury, J.; Chen, X.; Piletic, I. R.; Fayer, M. D., "Ultrafast dynamics of solute-solvent complexation observed at thermal equilibrium in real time". *Science* **2005,** *309* (5739), 1338-1343.

18. King, J. T.; Baiz, C. R.; Kubarych, K. J., "Solvent-Dependent Spectral Diffusion in a Hydrogen Bonded "Vibrational Aggregate"". *Journal of Physical Chemistry A* **2010,** *114* (39), 10590-10604.

19. King, J. T.; Ross, M. R.; Kubarych, K. J., "Ultrafast alpha-Like Relaxation of a Fragile Glass-Forming Liquid Measured Using Two-Dimensional Infrared Spectroscopy". *Physical Review Letters* **2012,** *108* (15), 157401.

20. Khalil, M.; Demirdoven, N.; Tokmakoff, A., "Vibrational coherence transfer characterized with Fourier-transform 2D IR spectroscopy". *Journal of Chemical Physics* **2004,** *121* (1), 362-373.

21. King, J. T.; Anna, J. M.; Kubarych, K. J., "Solvent-hindered intramolecular vibrational redistribution". *Physical Chemistry Chemical Physics* **2011,** *13* (13), 5579-5583.

22. King, J. T.; Ross, M. R.; Kubarych, K. J., "Water-Assisted Vibrational Relaxation of a Metal Carbonyl Complex Studied with Ultrafast 2D-IR". *Journal Physical Chemistry B* **2012,** *116* (12), 3754-3759.

23. Pisliakov, A. V.; Mancal, T.; Fleming, G. R., "Two-dimensional optical three-pulse photon echo spectroscopy. II. Signatures of coherent electronic motion and exciton population transfer in dimer two-dimensional spectra". *Journal of Chemical Physics* **2006,** *124* (23), 234505.

24. Demirdoven, N.; Khalil, M.; Golonzka, O.; Tokmakoff, A., "Correlation effects in the two-dimensional vibrational spectroscopy of coupled vibrations". *Journal of Physical Chemistry A* **2001,** *105* (34), 8025-8030.

25. Khalil, M.; Demirdoven, N.; Tokmakoff, A., "Coherent 2D IR spectroscopy: Molecular structure and dynamics in solution". *Journal of Physical Chemistry A* **2003,** *107* (27), 5258-5279.

26. Ozaktas, H. M.; Ankan, O.; Kutay, M. A.; Bozdagi, G., "Digital computation of the fractional Fourier transform". *IEEE Transactions on Signal Processing* **1996,** *44* (9).

27. Cooley, J. W.; Lewis, P. A. W.; Welch, P. D., "FINITE FOURIER TRANSFORM". *IEEE Transactions on Audio and Electroacoustics* **1969,** *AU17* (2).

28. Candes, E. J.; Wakin, M. B., "An introduction to compressive sampling". *IEEE Signal Processing Magazine* **2008,** *25* (2).

29. Anna, J. M.; Nee, M. J.; Baiz, C. R.; McCanne, R.; Kubarych, K. J., "Measuring absorptive two-dimensional infrared spectra using chirped-pulse upconversion detection". *Journal of the Optical Society of America B-Opt. Phys.* **2010,** *27* (3), 382-393.

30. Nee, M. J.; Baiz, C. R.; Anna, J. M.; McCanne, R.; Kubarych, K. J., "Multilevel vibrational coherence transfer and wavepacket dynamics probed with multidimensional IR spectroscopy". *The Journal of chemical physics* **2008,** *129* (8), 084503.

31. Nee, M. J.; McCanne, R.; Kubarych, K. J.; Joffre, M., "Two-dimensional infrared spectroscopy detected by chirped pulse upconversion". *Optics Letters* **2007,** *32* (6), 713-715.

32. van den Berg, E.; Friedlander, M. P., "PROBING THE PARETO FRONTIER FOR BASIS PURSUIT SOLUTIONS". *Siam Journal on Scientific Computing* **2008,** *31* (2).

33. Ori Katz, J. M. L., and Yaron Silberberg, "Compressive Fourier Transform Spectroscopy". **2011**.

34. Roberts, S. T.; Loparo, J. J.; Tokmakoff, A., "Characterization of spectral diffusion from two-dimensional line shapes". *Journal of Chemical Physics* **2006,** *125* (8), 084502.

Chapter Four

Synthesis and Characterization of the (Cholesteryl Benzoate) Chromium Tricarbonyl Vibrational Label

The work of this chapter was possible with the help of:

Josef A. Dunbar, Jacob G. Lapping, and Aaron M. White

4.1 Introduction

The lipid membrane, and its interface with water, is central to many chemical reactions critical for life including photosynthesis, ADP oxidation, and the initiation of cell signaling cascades. Understanding the dynamical properties of the lipid membrane and the interfacial water are essential if biochemical reactions at the lipid membrane are to be understood. Vibrational spectroscopy and its ability to measure ultrafast dynamics presents an ideal technique in measuring the dynamics of a lipid membrane and interfacial water, but requires the development of novel spectroscopic labels that can adequately probe these dynamics.

Vibrational spectroscopy methods—including FTIR[1-4], polarized-ATR[5, 6], and ultrafast pump-probe spectroscopies[7-9]—have long been powerful tools in disentangling complex biophysical processes. Active development of two-dimensional infrared spectroscopy (2D-IR) has revealed many aspects of biomolecular dynamics due to the method's ability to correlate the vibrational frequency of a chromophore during two separate time periods. Despite the additional information available with 2D-IR, its nonlinear nature requires a vibrational probe to have a strong intrinsic infrared transition strength in an uncluttered region of the spectrum, while being highly sensitive of the local environment. In the case of membrane components, there are few natural options, limited largely to the phosphate head group of some lipids, which occurs at roughly 1250 cm^{-1}, which is clearly not a background-free region of the infrared spectrum. Unlike the case of proteins or nucleobases, there are no strong carbonyl modes that can be accessed to probe lipid membranes. The O-H stretch of water in D_2O has been used to measure the dynamics of lipid membrane interfacial water[10-14] but these experiments are limited to the confined water of reverse micelles and found that the dynamics of interfacial water of reverse micelles are highly dependent on the size of the reverse micelles and the solvent[10, 11]. One potential motif is the metal carbonyl organometallic complex that has played a pivotal role in the development of 2DIR experiments used to study intramolecular vibrational energy redistribution[15, 16], chemical exchange[17, 18], energy relaxation[16], and spectral diffusion[19, 20]. In biology, metal carbonyls have found many uses including: Carbon monoxide releasing molecules (CORM) that release physiological levels of carbon monoxide either

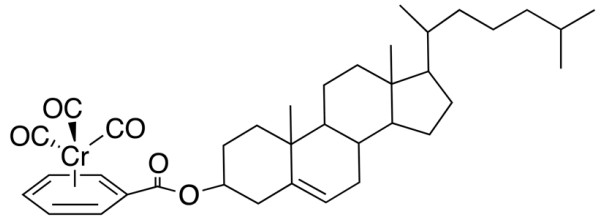

Figure 4.1 (cholesteryl benzoate) chromium tricarbonyl (chol-BCT) is synthesized by the hydroxyl group of cholesterol acting as a nucleophile in a Steglich esterification

spontaneously or upon photo excitation[21-23], the Fe-CO motif that is commonly used to probe the hemoglobin and myoglobin active sites[24-27], a derivative of 17 β-etradiol that is capable of measuring hormone receptor concentration[28, 29], and a rhenium tricarbonyl complex that was shown to image the Golgi apparatus of breast cancer cells[30, 31]. Recently, using 2DIR, the a surface-bound metal carbonyl complex has successfully measured protein flexibility and the hydration dynamics of globular proteins[32, 33] and a cyclopentadienyl rhenium carbonyl was shown to be a robust protein label for 2DIR, but additional labels are needed to probe a more diverse range of biological systems.

We propose a novel label to probe the lipid membrane-water interface, (cholesteryl benzoate) chromium tricarbonyl, based on the benzene chromium tricarbonyl (BCT) piano stool complex (**Fig. 4.1**). Here, we establish a simple protocol to synthesize chol-BCT and embed it in a lipid membrane, characterize the chol-BCT complex, and then using FTIR and polarized-ATR measurements we determine the location and relative orientation of chol-BCT once embedded in the lipid bilayer. To demonstrate the robustness of the chol-BCT label, we label both a small unilaminar vesicle (SUV)[34, 35], a spherical lipid bilayer with both an external and enclosed aqueous region, as well as a bicelle[36, 37] that is a planar lipid bilayer composed of a lipid forming

the edges of the bicelle and another lipid making the bilayer. These experiments demonstrate that chol-BCT is a useful probe of both lipid environments. Using 2DIR and a similar four wave-mixing experiment, rapidly acquired spectral diffusion (RASD), we test ability of chol-BCT to probe water at the interface of a lipid membrane in these experiments and find chol-BCT to be an excellent probe for ultrafast dynamical studies.

4.2 Experimental Methods

4.2.1 Materials. (ethyl benzoate) chromium tricarbonyl was purchased from Sigma Aldrich and was used without further purification. 1-palmitoyl-2-oleoyl-sn-glycero-3-phosphocholine (POPC), 1,2-Dimyristoyl-*sn*-Glycero-3-Phosphocholine (DMPC), and 1,2-Dihexanoyl-*sn*-Glycero-3-Phosphocholine (DHPC) suspended in chloroform were purchased from Avanti lipids and used without further purification.

4.2.2 Bicelle preparation. The DMPC:DHPC:chol-BCT molar ratio was 65:24:1. Lipids and chol-BCT label were cosolublized in chloroform. The chloroform was subsequently removed by evaporation and was then placed under vacuum for two hours. The mixture was solubilized with a phosphate buffer at pH 7.2 to give a final lipid concentration of 120 mM. Bicelles were formed by a series of five freeze (-78 °C) thaw (30 °C) cycles.

4.2.3 SUV preparation. Two SUV preparation protocols were used. For the polarized FTIR experiments, the POPC:POPG:chol-BCT molar ratio was 8.2:2.7:1. The mixture was cosolublized in chloroform, dried, and re-solubilized with a phosphate buffer at pH 7.2

as above to give a final lipid concentration of 25 mM. After a 1 hour sonication of the mixture, a clear suspension of SUV's was obtained. The above bicelle protocol was also used to produce a sample where choline is the only lipid head group to adequately compare the bicelle and SUV samples (Fig. 5). The POPC:chol-BCT molar ratio used in these mixtures was 10:1.

4.2.4 Polarized-ATR. Polarized attenuated total reflectance (ATR) spectroscopy was used to measure the orientation of the probe relative to the lipid surface. Polarized-ATR spectroscopy measurements were made with a Jasco FT/IR-4100 spectrometer with a ZnSe 10 internal reflections crystal (Pike Technologies) accessory. The SUVs containing the chol-BCT probe were prepared as described above and were allowed to deposit on the crystal surface for two hours. Once the SUV is deposited onto the ATR plate, we measure the amplitude of the *s* and *p* polarizations separately to determine the order parameter of the transition dipole moment[5]:

$$S_\theta = \frac{\left(E_x^2 - R^{ATR}E_y^2 + E_z^2\right)}{\left(E_x^2 - R^{ATR}E_y^2 - 2E_z^2\right)} \qquad (1)$$

Where E_x, E_y, and E_z are the amplitudes of the evanescent waves at the surface of the ATR plate and have been derived elsewhere[38] and R_{ATR} is the ratio of the *s* and *p* amplitudes, $R_{ATR} = \frac{A_p}{A_s}$. The order parameter is related to the orientation of the transition dipole moment through:

$$S_\theta = \frac{\left(3\left\langle \cos^2\theta \right\rangle - 1\right)}{2} \qquad (2)$$

Where q is the angle between the transition dipole moment and the vector normal to the

surface of the ATR crystal and the brackets indicate the orientational ensemble average.

4.2.5 Four-wave mixing experiments. The experimental setups of two dimensional infrared spectroscopy (2DIR)[39] and rapidly acquired spectral diffusion (RASD)[40] used to test the utility of chol-BCT as an ultrafast dynamical probe are described elsewhere.

4.2.6 DFT calculations. All calculations were performed in Gaussian 09[41] software suite using the B3LYP functional and 6-31+G(d) basis set for all atoms with symmetry disabled. The (ethyl benzoate) chromium tricarbonyl was first minimized before the sodium ion was introduced to the calculations. Geometry was optimized while keeping fixed the sodium ion to chromium atom distance, and was followed by frequency calculations.

4.3 Synthesis and Characterization

Locating chromium tricarbonyl at the water interface of a lipid membrane is achieved by labeling cholesterol with (benzoic acid) chromium tricarbonyl and then embedding the labeled cholesterol into the lipid membrane (**Fig. 4.2**). The (benzoic acid) chromium tricarbonyl was synthesized with a simple hydrolysis reaction of (ethyl benzoate) chromium tricarbonyl[42]. A mixture of 240 mg of (ethyl benzoate) chromium tricarbonyl and 400 mg of sodium hydroxide in 30 ml of deionized water is stirred in the dark at room temperature for 16 hrs. The progress of the reaction can be monitored as the orange colored (ethyl benzoate) chromium tricarbonyl is insoluble and the red colored (benzoic acid) chromium tricarbonyl product is soluble. The unreacted (ethyl benzoate) chromium tricarbonyl is removed through ether extraction, the product, (benzoic acid)

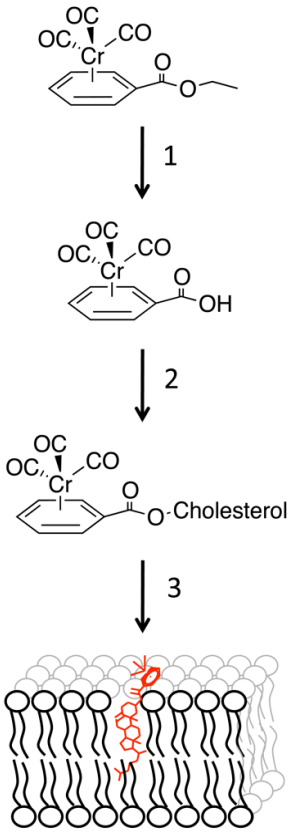

Figure 4.2. Synthesis process used to introduce the chromium tricarbonyl motif to the lipid-water interface

chromium tricarbonyl, is then precipitated out of solution by acidifying the remaining mixture with hydrochloric acid to pH 2.0, and isolated through a second round of ether extraction.

(Cholesteryl benzoate) chromium tricarbonyl (chol-BCT) was synthesized using a Steglich esterification[43]. A mixture of 700 mM cholesterol, 30 mM (benzoic acid) chromium tricarbonyl, 4 mM 4-dimethylaminopyradine, and 11 mL of N,N′-diisopropylcarbodiimide in 100 mL chloroform was placed on ice for 5 minutes and was then stirred in the dark for 3 hrs at room temperature. The product was subsequently purified through column chromatography using alumina as the stationary phase and a

3:1 mixture of heptane and ethyl acetate as the mobile phase. The light yellow colored chol-BCT is the first product through the column and is isolated from the solvent using a rotary evaporator. The N,N'-diisopropylcarbodiimide exits the column simultaneously with the chol-BCT; to ensure that the N,N'-diisopropylcarbodiimide is removed from the sample, the product is left on the rotary evaporator for an additional 20 min after the solvent is removed. The presence of N,N'-diisopropylcarbodiimide can be assessed by monitoring its C=N=C stretch at 2100 cm^{-1}.

We confirmed the synthesis of chol-BCT with EI+ mass spectroscopy; the molecular ion peaks at 626.3 m/z and 542.3 m/z are of chol-BCT and chol-BCT without the carbonyls respectively. Further characterization of the product was accomplished using melting point analysis, TGA, and IR. The melting point was measured at 165 °C where as the decomposition, measured with thermogravimetric analysis, began at a much higher temperature of about 290 °C. The IR spectrum of the product – 3097, 2932, 1958, 1881, 1730, 1524, 1499, 1441, 1415, and 1370 cm^{-1} – contains the peaks of both cholesterol and (benzoic acid) chromium tricarbonyl with the exception of the O-H stretch at 3350 cm^{-1} of cholesterol.

4.4 Results and Discussion

To assess the sensitivity of the chromium tricarbonyl to the solvent environment, we measure the FTIR spectra of the carbonyl's degenerate asymmetric modes and the symmetric mode, 1928 and 1992 cm^{-1} in hexane respectively, in multiple solvents with varying polarities (**Fig. 4.3**).

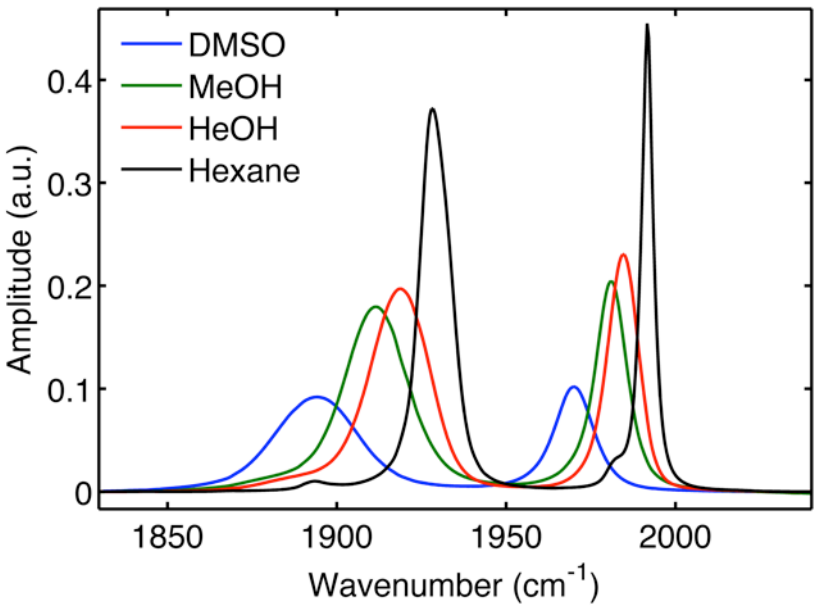

Figure 4.3. The asymmetric and symmetric modes of (benzyl) chromium tricarbonyl in a series of solvents. An increase in solvent polarity tends to red shift both asymmetric and symmetric modes

Both symmetric and asymmetric stretches of BCT are red-shifted with increased polarity, as is observed in many metal carbonyl complexes[19, 44]. The symmetric and asymmetric stretches in the most polar solvent examined, dimethyl sulfoxide, are red shifted 22 cm^{-1} and 34 cm^{-1} respectively relative to the least polar solvent, hexane. In all measured solvents, the asymmetric peak is broader than the symmetric band, but we do not see noticeable splitting of the degenerate modes in the solvent presented here.

We assess the location of the chol-BCT carbonyls in a small unilaminar vesicle (SUV) and a bicelle by measuring their FTIR spectrum and comparing them to the spectrum of the chol-BCT in hexane (**Fig. 4.4**). The symmetric stretch of chol-BCT in the SUV and the bicelle are red-shifted relative to chol-BCT in hexane by 25 cm^{-1} and 17 cm^{-1} respectively indicating that the probe in both the SUV and the bicelle are in a more polar environment than hexane. Because lipid bilayers are composed of two regions, the

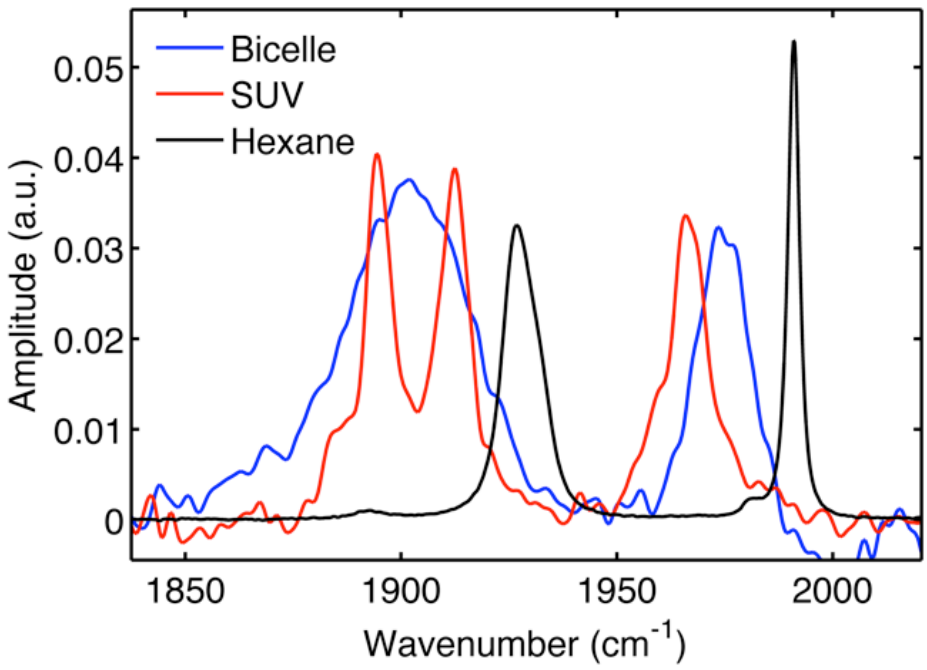

Figure 4.4. The chol-BCT label in a bicelle, and small unilaminar vesicle in water and chol-BCT in a hexane. chol-BCT in both bilayers is red shifted relative to the hexane indicating the probe is situated in the more polar head groups and the splitting of the asymmetric bands in the SUV suggests the label in an SUV is situated near an ion.

non-polar alkane chains and the polar head groups at the water interface, the relative red shift of the carbonyls of the chol-BCT probe in the SUV and the bicelle suggests that the carbonyls are situated near the more polar head groups and the water at the interface. **Fig. 4.4** also shows that the degenerate asymmetric stretch in the SUV exhibits distinct splitting that we attribute to the carbonyl's proximity to an ion. We verify the ion's role in splitting the degenerate bands by performing DFT calculations on (ethyl benzoate) chromium tricarbonyl at a fixed distance from a sodium ion. The smaller size of (ethyl benzoate) chromium tricarbonyl allows for shorter computational time relative to that required for chol-BCT yet it is an adequate model of chol-BCT. We performed all calculations in vacuum, which enhances the effect of degeneracy splitting; if a solvent were to be introduced, we would expect the additional atoms to

Charge Distance	S	A1	A2	Splitting
No Charge	2057 cm^{-1}	2005 cm^{-1}	1998 cm^{-1}	7 cm^{-1}
5 Å	2071 cm^{-1}	2030 cm^{-1}	1835 cm^{-1}	195 cm^{-1}
10 Å	2050 cm^{-1}	1999 cm^{-1}	1979 cm^{-1}	20 cm^{-1}

Table 4.1. The DFT calculated vibrational frequencies of the three carbonyl modes of (ethyl benzoate) chromium tricarbonyl with a sodium ion fixed 5 and 10 Å from the chromium atom and without a sodium ion.

shield the probe from the ion making the distance at which the probe senses the ion and the magnitude of the splitting to be much smaller. When the sodium ion is excluded from the calculation, the ethyl benzoate alone is capable of breaking the symmetry and splits the degenerate band by 7 cm^{-1} (**Table 4.1**). The sodium ion located 5 Å from the chromium atom splits the band by 195 cm^{-1}, while a 10 Å distance results in a 20 cm^{-1} splitting. Hence, the pronounced splitting appears to be indicative of local electrostatics due to charges associated with the membrane, though in a real solution, the solvent will shield local charges to some extent.

Given that the SUV-bound label exhibits pronounced splitting whereas bicelle-bound label does not, it is likely that the labels are in different environments in the two cases. The oleoyl and palmitoyl alkane chains of the POPC SUV are longer and less saturated, 18:1 and 16:0 respectively, than the two myristoyl alkane chains, 14:0, of DMPC used in the bicelles. Although the shape of the SUV is spherical while the bicelle is planar, the splitting remains when the SUV is deposited on a planar surface (**Fig. 5**) and therefore the curvature of the SUV is not the origin of the degenerate splitting. Thus, we propose that the lack of splitting in the bicelle is due to its shorter and

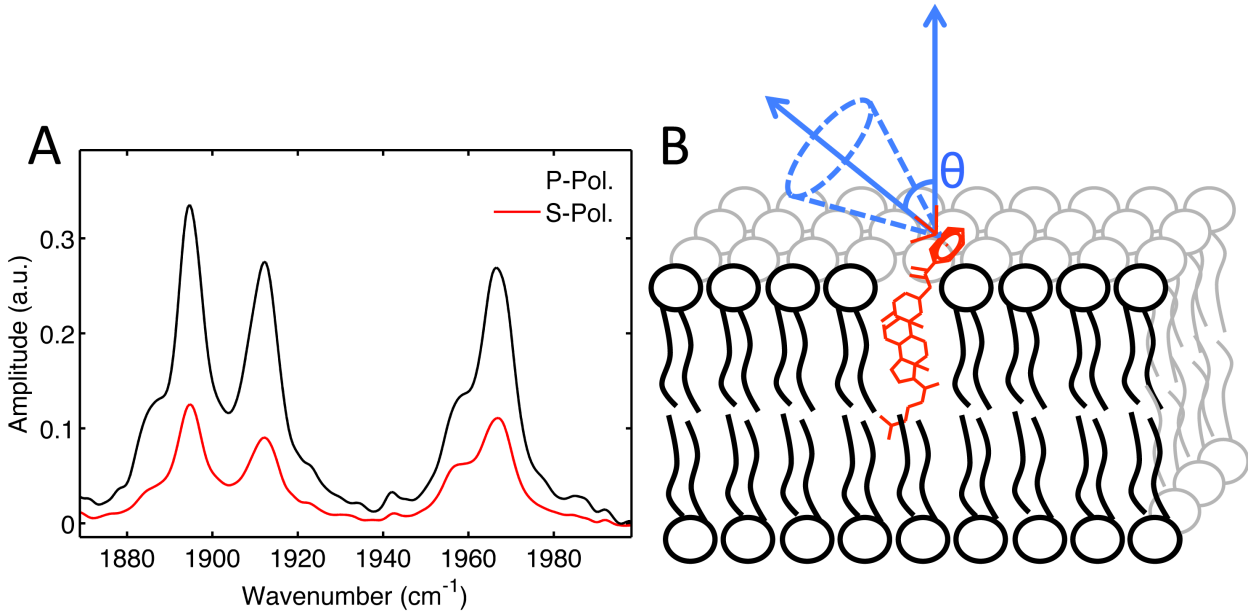

Figure 4.5. We measured the relative s and p polarized amplitudes of the symmetric stretch using a ATR plate (A) to determine the relative orientation of the carbonyls. These measurements suggest that the vector perpendicular to the benzene ring is at an angle of 46° from the vector normal to the membrane surface.

saturated alkane chains pushing the carbonyls of chol-BCT further into the aqueous solvent reducing their proximity to the charged head groups.

Although the FTIR experimental data gives information on the location of the carbonyls in the membranes, it does not give information on the relative orientation of the carbonyls; this is determined using polarized-ATR (**Fig. 4.5**). We measure the *p* and *s* polarization amplitudes of the symmetric mode and then utilizing eq. 1 and eq. 2, we determine the orientation of the transition dipole moment of the symmetric mode relative to the ATR crystal surface. Because the lipid bilayer is deposited onto the surface of the ATR trough and the transition dipole moment of the symmetric stretch is perpendicular to the benzyl ring, measuring the ratio of the *s* and *p* polarization amplitudes of the symmetric stretch is a measure of the orientation of the of the benzyl ring relative to the lipid membrane. We measure the ratio of *p* and *s* amplitudes, A_p/A_s,

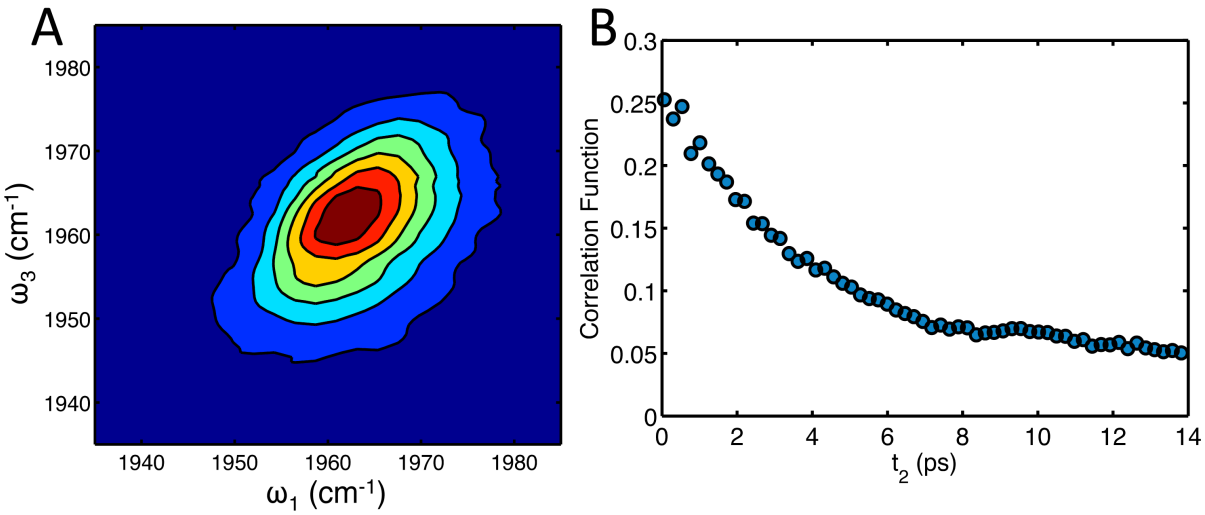

Figure 4.6. The chol-BCT label embedded in a bicelle bilayer was probed using the four wave mixing experiments 2DIR (A) and RASD (B). The signal to noise levels of these experiments suggest that chol-BCT is an adequate probe of the lipid-water interface.

to be 2.5, indicating the vector perpendicular to the benzyl ring makes an angle of 46° relative to the vector normal to the membrane surface (**Fig. 4.5b**). The structure of the chol-BCT probe is flexible about the ester bond allowing for a distribution of probe orientations, hence the angle of 46° represents the average orientation.

We test the capabilities of chol-BCT as a dynamical probe of the membrane-water interface by analyzing two different four-wave mixing experiments on the symmetric stretch in a bicelle at 1973 cm^{-1}. The 2DIR spectrum is noticeably elongated along the diagonal indicating the band is inhomogeneously broadened due to a distribution of local environments, and is capable of measuring the microenvironment dynamics near the tricarbonyls of chol-BCT (**Fig. 4.6a**). We use rapidly acquired spectral diffusion (RASD) to measure the frequency-frequency correlation function (FFCF) of the label (**Fig. 4.6b**), and fitting the FFCF of the chol-BCT label in the lipid membrane to an exponential with an offset, $A \cdot exp(-t/\tau_c) + B$, gives the spectral diffusion time constant of 3.76 ps ± 0.075 ps, which compares favorably to that of CN^- in water[45] and a metal

carbonyl probe at the surface of lysozyme[32] suggesting that chromium tricarbonyl is indeed situated at the interface of the lipid membrane with water. Given the slightly slower spectral diffusion relative to the protein surface, it is possible that either the water dynamics are in fact slower near the membrane, or that the probe adopts a conformation such that it is partially shielded from the water. Nevertheless, in the case of water near DNA, slowdowns factors of 2-3 have been reported[46, 47], which are consistent with the measurements found here for the bicelle/water interface. Clearly the signal to noise ratios are sufficient to enable a broad range of 2D-IR and RASD measurements of membrane and hydration dynamics using the BCT vibrational probe.

4.5 Conclusion

The inherent nonlinear capabilities of 2D-IR spectroscopy allows 2D-IR to be a measure of the ultrafast dynamical studies, yet labels adequate for these experiments are limited. The strong intrinsic infrared transition strength and high sensitivity to local environment of (cholesteryl benzoate) chromium tricarbonyl (chol-BCT) suggests that chol-BCT is an ideal probe of the membrane-water interface. Here, we have developed a protocol for placing the chromium tricarbonyl motif at the interface of water and the lipid membrane by first synthesizing (cholesteryl benzoate) chromium tricarbonyl (chol-BCT) and then embedding the chol-BCT label in the lipid membrane. We characterized the chol-BCT label with mass spectroscopy, FTIR spectroscopy, melting point, and thermogravimetric analysis and determined the location and orientation of the chromium tricarbonyl relative to the lipid membrane through FTIR and polarized-

ATR spectroscopies. These experiments suggest that the chromium tricarbonyl motif is positioned at the membrane-water interface. The measurements of chol-BCT with the two different nonlinear infrared experiments 2D-IR and RASD suggest that chol-BCT is a useful label of interfacial dynamics. We have also used the synthesis protocol presented here to label multiple hydroxyl groups not included in this manuscript including glyceryl 1,3-dipamitate, 1-palmitoyl-2-oleoyl-sn-glycero-3-phosphoglycerol, and n-butanol suggesting this protocol can be used in diverse settings. Potentially, with the use of other similar piano stool metal carbonyl complexes (e.g. cyclopentadienyl manganese tricarbonyl), multiple chemical groups of a lipid bilayer can be labeled with the different metal carbonyl complexes allowing for additional experiments including bilayer aggregation, where different probes can observe distinct components in parallel.

4.6 References

1. Jackson, M.; Mantsch, H. H., "THE USE AND MISUSE OF FTIR SPECTROSCOPY IN THE DETERMINATION OF PROTEIN-STRUCTURE". *Critical Reviews in Biochemistry and Molecular Biology* **1995,** *30* (2), 95-120.

2. Lydakis-Simantiris, N.; Hutchison, R. S.; Betts, S. D.; Barry, B. A.; Yocum, C. F., "Manganese stabilizing protein of photosystem II is a thermostable, natively unfolded polypeptide". *Biochemistry* **1999,** *38* (1), 404-414.

3. Offenbacher, A. R.; Chen, J.; Barry, B. A., "Perturbations of Aromatic Amino Acids Are Associated with Iron Cluster Assembly in Ribonucleotide Reductase". *Journal of the American Chemical Society* **2011,** *133* (18), 6978-6988.

4. Krimm, S.; Bandekar, J., "VIBRATIONAL SPECTROSCOPY AND CONFORMATION OF PEPTIDES, POLYPEPTIDES, AND PROTEINS". *Advances in Protein Chemistry* **1986,** *38*, 181-364.

5. Tamm, L. K.; Tatulian, S. A., "Infrared spectroscopy of proteins and peptides in lipid bilayers". *Quarterly Reviews of Biophysics* **1997,** *30* (4), 365-429.

6. Gazit, E.; Miller, I. R.; Biggin, P. C.; Sansom, M. S. P.; Shai, Y., "Structure and orientation of the mammalian antibacterial peptide cecropin P1 within phospholipid membranes". *Journal of Molecular Biology* **1996,** *258* (5), 860-870.

7. Vogel, R.; Siebert, F., "Vibrational spectroscopy as a tool for probing protein function". *Current Opinion in Chemical Biology* **2000,** *4* (5), 518-523.

8. Mathies, R. A.; Lin, S. W.; Ames, J. B.; Pollard, W. T., "FROM FEMTOSECONDS TO BIOLOGY - MECHANISM OF BACTERIORHODOPSINS LIGHT-DRIVEN PROTON PUMP". *Annual Review of Biophysics and Biophysical Chemistry* **1991,** *20*, 491-518.

9. Woutersen, S.; Emmerichs, U.; Bakker, H. J., "Femtosecond Mid-IR Pump-Probe Spectroscopy of Liquid Water: Evidence for a Two-Component Structure". *Science* **1997,** *278* (5338), 658-660.

10. Fenn, E. E.; Wong, D. B.; Fayer, M. D., "Water dynamics in small reverse micelles in two solvents: Two-dimensional infrared vibrational echoes with two-dimensional background subtraction". *Journal of Chemical Physics* **2011,** *134* (5).

11. Fenn, E. E.; Wong, D. B.; Giammanco, C. H.; Fayer, M. D., "Dynamics of Water at the Interface in Reverse Micelles: Measurements of Spectral Diffusion with Two-Dimensional Infrared Vibrational Echoes". *J. Phys. Chem. B* **2011,** *115* (40), 11658-11670.

12. Levinger, N. E.; Costard, R.; Nibbering, E. T. J.; Elsaesser, T., "Ultrafast Energy Migration Pathways in Self-Assembled Phospholipids Interacting with Confined Water". *The Journal of Physical Chemistry A* **2011,** *115* (43), 11952-11959.

13. Costard, R.; Levinger, N. E.; Nibbering, E. T. J.; Elsaesser, T., "Ultrafast Vibrational Dynamics of Water Confined in Phospholipid Reverse Micelles". *The Journal of Physical Chemistry B* **2012,** *116* (19), 5752-5759.

14. Moilanen, D. E.; Fenn, E. E.; Wong, D.; Fayer, M. D., "Water Dynamics at the Interface in AOT Reverse Micelles". *The Journal of Physical Chemistry B* **2009,** *113* (25), 8560-8568.

15. King, J. T.; Anna, J. M.; Kubarych, K. J., "Solvent-hindered intramolecular vibrational redistribution". *Physical Chemistry Chemical Physics* **2011,** *13* (13), 5579-5583.

16. Khalil, M.; Demirdoven, N.; Tokmakoff, A., "Coherent 2D IR spectroscopy: Molecular structure and dynamics in solution". *Journal of Physical Chemistry A* **2003,** *107* (27), 5258-5279.

17. Anna, J. M.; Kubarych, K. J., "Watching solvent friction impede ultrafast barrier crossings: A direct test of Kramers theory". *Journal of Chemical Physics* **2010,** *133* (17).

18. Cahoon, J. F.; Sawyer, K. R.; Schlegel, J. P.; Harris, C. B., "Determining transition-state geometries in liquids using 2D-IR". *Science* **2008,** *319* (5871).

19. King, J. T.; Baiz, C. R.; Kubarych, K. J., "Solvent-Dependent Spectral Diffusion in a Hydrogen Bonded "Vibrational Aggregate"". *Journal of Physical Chemistry A* **2010,** *114* (39), 10590-10604.

20. King, J. T.; Ross, M. R.; Kubarych, K. J., "Ultrafast alpha-Like Relaxation of a Fragile Glass-Forming Liquid Measured Using Two-Dimensional Infrared Spectroscopy". *Physical Review Letters* **2012,** *108* (15).

21. Clark, J. E.; Naughton, P.; Shurey, S.; Green, C. J.; Johnson, T. R.; Mann, B. E.; Foresti, R.; Motterlini, R., "Cardioprotective actions by a water-soluble carbon monoxide-releasing molecule". *Circ.Res.* **2003,** *93* (2), E2-E8.

22. Foresti, R.; Hammad, J.; Clark, J. E.; Johnson, T. R.; Mann, B. E.; Friebe, A.; Green, C. J.; Motterlini, R., "Vasoactive properties of CORM-3, a novel water-soluble carbon monoxide-releasing molecule". *British Journal of Pharmacology* **2004,** *142* (3), 453-460.

23. Sawle, P.; Foresti, R.; Mann, B. E.; Johnson, T. R.; Green, C. J.; Motterlini, R., "Carbon monoxide-releasing molecules (CO-RMs) attenuate the inflammatory response elicited by lipopolysaccharide in RAW264.7 murine macrophages". *British Journal of Pharmacology* **2005,** *145* (6), 800-810.

24. Caughey, W. S.; Shimada, H.; Choc, M. G.; Tucker, M. P., "DYNAMIC PROTEIN STRUCTURES - INFRARED EVIDENCE FOR 4 DISCRETE RAPIDLY INTERCONVERTING CONFORMERS AT THE CARBON-MONOXIDE BINDING-SITE OF BOVINE HEART MYOGLOBIN". *Proceedings of the National Academy of Sciences of the United States of America-Biological Sciences* **1981,** *78* (5), 2903-2907.

25. Lim, M. H.; Jackson, T. A.; Anfinrud, P. A., "Ultrafast rotation and trapping of carbon monoxide dissociated from myoglobin". *Nature Structural Biology* **1997,** *4* (3), 209-214.

26. Tsubaki, M.; Srivastava, R. B.; Yu, N. T., "RESONANCE RAMAN INVESTIGATION OF CARBON-MONOXIDE BONDING IN (CARBON MONOXY) HEMOGLOBIN AND (CARBON MONOXY) MYOGLOBIN - DETECTION OF FE-CO STRETCHING AND FE-C-O BENDING VIBRATIONS AND INFLUENCE OF THE QUATERNARY STRUCTURE CHANGE". *Biochemistry* **1982,** *21* (6), 1132-1140.

27. Alben, J. O.; Caughey, W. S., "AN INFRARED STUDY OF BOUND CARBON MONOXIDE IN HUMAN RED BLOOD CELL ISOLATED HEMOGLOBIN AND HEME CARBONYLS". *Biochemistry* **1968,** *7* (1), 175-&.

28. Jaouen, G.; Vessieres, A.; Top, S.; Ismail, A. A.; Butler, I. S., "METAL-CARBONYL FRAGMENTS AS A NEW CLASS OF MARKERS IN MOLECULAR-BIOLOGY". *Journal of the American Chemical Society* **1985,** *107* (16).

29. Top, S.; Jaouen, G.; Vessieres, A.; Abjean, J. P.; Davoust, D.; Rodger, C. A.; Sayer, B. G.; McGlinchey, M. J., "CHROMIUM TRICARBONYL COMPLEXES OF ESTRADIOL DERIVATIVES - DIFFERENTIATION OF ALPHA-DIASTEREOISOMER AND BETA-DIASTEREOISOMERS USING ONE-DIMENSIONAL AND TWO-DIMENSIONAL NMR-SPECTROSCOPY AT 500-MHZ". *Organometallics* **1985,** *4* (12), 2143-2150.

30. Clede, S.; Lambert, F.; Sandt, C.; Gueroui, Z.; Refregiers, M.; Plamont, M.-A.; Dumas, P.; Vessieres, A.; Policar, C., "A rhenium tris-carbonyl derivative as a single core multimodal probe for imaging (SCoMPI) combining infrared and luminescent properties". *Chemical Communications* **2012,** *48* (62), 7729-7731.

31. Policar, C.; Waern, J. B.; Plamont, M.-A.; Clede, S.; Mayet, C.; Prazeres, R.; Ortega, J.-M.; Vessieres, A.; Dazzi, A., "Subcellular IR Imaging of a Metal-Carbonyl Moiety Using Photothermally Induced Resonance". *Angew. Chem.-Int. Edit.* **2011,** *50* (4), 860-864.

32. King, J. T.; Kubarych, K. J., "Site-Specific Coupling of Hydration Water and Protein Flexibility Studied in Solution with Ultrafast 2D-IR Spectroscopy". *Journal of the American Chemical Society* **2012,** *134* (45), 18705-18712.

33. King, J. T.; Ross, M. R.; Kubarych, K. J., "Water-Assisted Vibrational Relaxation of a Metal Carbonyl Complex Studied with Ultrafast 2D-IR". *J. Phys. Chem. B* **2012,** *116* (12), 3754-3759.

34. Pitcher, W. H.; Huestis, W. H., "Preparation and analysis of small unilamellar phospholipid vesicles of a uniform size". *Biochemical and Biophysical Research Communications* **2002,** *296* (5), 1352-1355.

35. Szoka, F. C.; Milholland, D.; Barza, M., "EFFECT OF LIPID-COMPOSITION AND LIPOSOME SIZE ON TOXICITY AND INVITRO FUNGICIDAL ACTIVITY OF LIPOSOME-INTERCALATED AMPHOTERICIN-B". *Antimicrobial Agents and Chemotherapy* **1987,** *31* (3), 421-429.

36. Sanders, C. R.; Prosser, R. S., "Bicelles: a model membrane system for all seasons?". *Structure with Folding & Design* **1998,** *6* (10), 1227-1234.

37. Vold, R. R.; Prosser, R. S.; Deese, A. J., "Isotropic solutions of phospholipid bicelles: A new membrane mimetic for high-resolution NMR studies of polypeptides". *Journal of Biomolecular Nmr* **1997,** *9* (3), 329-335.

38. Harrick, N. J.; Beckmann, K. H., "INTERNAL REFLECTION SPECTROSCOPY AND ELLIPSOMETRY FOR STUDY OF THIN FILMS". *J. Electrochem. Soc.* **1968,** *115* (3), C61-&.

39. Nee, M. J.; Baiz, C. R.; Anna, J. M.; McCanne, R.; Kubarych, K. J., "Multilevel vibrational coherence transfer and wavepacket dynamics probed with multidimensional IR spectroscopy". *The Journal of chemical physics* **2008,** *129* (8), 084503.

40. Osborne, D. G.; Kubarych, K. J., "Rapid and Accurate Measurement of the Frequency,ÄìFrequency Correlation Function". *The Journal of Physical Chemistry A* **2012**.

41. M. J. Frisch, G. W. T., H. B. Schlegel, G. E. Scuseria, M. A. Robb, J. R. Cheeseman, G. Scalmani, V. Barone, B. Mennucci, G. A. Petersson, H. Nakatsuji, M. Caricato, X. Li, H. P. Hratchian, A. F. Izmaylov, J. Bloino, G. Zheng, J. L. Sonnenberg, M. Hada, M. Ehara, K. Toyota, R. Fukuda, J. Hasegawa, M. Ishida, T. Nakajima, Y. Honda, O. Kitao, H. Nakai, T. Vreven, J. A. Montgomery, Jr., J. E. Peralta, F. Ogliaro, M. Bearpark, J. J. Heyd, E. Brothers, K. N. Kudin, V. N. Staroverov, R. Kobayashi, J. Normand, K. Raghavachari, A. Rendell, J. C. Burant, S. S. Iyengar, J. Tomasi, M. Cossi, N. Rega, J. M. Millam, M. Klene, J. E. Knox, J. B. Cross, V. Bakken, C. Adamo, J. Jaramillo, R. Gomperts, R. E. Stratmann, O. Yazyev, A. J. Austin, R. Cammi, C. Pomelli, J. W. Ochterski, R. L. Martin, K. Morokuma, V. G. Zakrzewski, G. A. Voth, P. Salvador, J. J. Dannenberg, S. Dapprich, A. D. Daniels, Ö. Farkas, J. B. Foresman, J. V. Ortiz, J. Cioslowski, and D. J. Fox *Gaussian 09 A.02*, Gaussian, Inc.: Wallingford CT, 2009.

42. Nicholls, B.; Whiting, M. C., "THE ORGANIC CHEMISTRY OF THE TRANSITION ELEMENTS .1. TRICARBONYLCHROMIUM DERIVATIVES OF AROMATIC COMPOUNDS". *Journal of the Chemical Society* **1959,** (FEB), 551-556.

43. Neises, B.; Steglich, W., "4-DIALKYLAMINOPYRIDINES AS ACYLATION CATALYSTS .5. SIMPLE METHOD FOR ESTERIFICATION OF CARBOXYLIC-ACIDS". *Angewandte Chemie-International Edition in English* **1978,** *17* (7), 522-524.

44. Creaser, C. S.; Fey, M. A.; Stephenson, G. R., "Environment sensitivity of IR-active metal carbonyl probe groups". *Spectrochimica Acta Part A: Molecular Spectroscopy* **1994,** *50* (7), 1295-1299.

45. Kozinski, M.; Garrett-Roe, S.; Hamm, P., "Vibrational spectral diffusion of CN- in water". *Chem. Phys.* **2007,** *341* (1-3), 5-10.

46. Szyc, Ł.; Yang, M.; Nibbering, E. T. J.; Elsaesser, T., "Ultrafast Vibrational Dynamics and Local Interactions of Hydrated DNA". *Angewandte Chemie International Edition* **2010,** *49* (21), 3598-3610.

47. Yang, M.; Szyc, Å.; Elsaesser, T., "Decelerated Water Dynamics and Vibrational

Couplings of Hydrated DNA Mapped by Two-Dimensional Infrared Spectroscopy". *The Journal of Physical Chemistry B* **2011,** *115* (44), 13093-13100.

Chapter Five

Spectral Diffusion as an Entropic Probe

The work of this chapter has been published as the following article:

Derek G. Osborne, John T. King, Josef A. Dunbar, Aaron M. White, and Kevin J. Kubarych "Ultrafast 2DIR Probe of a Host-Guest Inclusion Complex: Structural and Dynamical Constraints of Nanoconfinement" Journal of Chemical Physics (In press)

5.1 Introduction

Small molecule vibrational probes based on transition metal carbonyl complexes have the promise to significantly broaden the toolset of spectroscopic sensors of structure and dynamics in complex environments. With their exceptionally strong infrared transition moments and Raman cross sections, the carbonyl bands facilitate the use of nonlinear optical techniques, such as two-dimensional IR (2DIR) spectroscopy, that require multiple interactions with individual molecules to generate a signal. A wide variety of metal carbonyl complexes are suitable for straightforward incorporation into larger chemical contexts such as proteins and membranes using simple conjugation chemistry; their relatively small sizes minimize structural perturbations. Ultrafast

visible and IR spectroscopy has been an established means of studying metal carbonyl photochemical reaction dynamics[1, 2], vibrational relaxation[3-5], and, more recently, solvation and vibrational energy redistribution[6]. Metal carbonyl complexes are particularly well suited to 2DIR spectroscopy because of the rich intramolecular coupling that leads to vibrational exciton bands that are largely homogeneously broadened, resulting in relatively sharp spectral features that nevertheless exhibit some degree of inhomogeneous broadening in polar solvents. These vibrational transitions offer a convenient compromise between spectral resolution and environmental sensitivity, making them useful probes of local structure and dynamics.

Metal carbonyl complexes have played a central role in the development of 2DIR spectroscopy, primarily as models of vibrational coupling[7, 8], energy relaxation and redistribution[4], as well as serving as probes of equilibrium solvation dynamics[9, 10]. Since some metal carbonyl complexes are structurally flexible and may exist in several conformations, it is possible to probe reaction dynamics at equilibrium using 2DIR chemical exchange spectroscopy. Specifically, chemical exchange spectroscopy has revealed the transition state and reaction kinetics of Berry pseudorotation in the fluxional $Fe(CO)_5$ complex[11] as well as both the barriers to isomerization between two conformers of $Co_2(CO)_8$ and the solvent friction dependence of the activated crossing[1, 12]. Recently, we have used 2DIR spectroscopy to disentangle four different isomers of $[CpRu(CO)_2]_2$ dimers[13]. Using transient IR echo spectroscopy, it is also possible to identify distinct geminate rebinding products following photodissociation of the Mo–Mo bond of $[CpMo(CO)_3]_2$ dimers, showing that the rebinding proceeds through only

one of the two thermodynamically stable isomers on the sub-50 ps time scale[2]. Additionally, small-molecule models of hydrogenase enzymes have been studied in detail using equilibrium and transient 2DIR spectroscopy, revealing complex solvation and energy relaxation dynamics[14]. In a series of systematic studies of dimanganese decacarbonyl ($Mn_2(CO)_{10}$, DMDC), dynamics in linear alcohols, we found a simple correlation between solvation dynamics and solvent viscosity[10]. In contrast, the rates of intramolecular vibrational redistribution (IVR) exhibited a pronounced non-monotonic solvent dependence reflecting the local hydrogen bonding solvation shell structure identified by molecular dynamics simulations[9]. Many of these observations and their interpretations are often completely absent from linear Fourier transform IR spectra, only becoming evident through the enhanced dynamical capabilities of 2D spectroscopy. One particularly striking example is our recent observation of non-exponential and non-Arrhenius spectral diffusion dynamics in a fragile glass forming liquid approaching the glass transition temperature[15]. In that case, the linear FTIR spectrum exhibited no temperature dependence, highlighting its blindness to the glassy dynamics clearly exposed by 2DIR spectroscopy. The ultrafast nature of 2DIR spectroscopy has the capability to probe the complex nonreactive dynamics of a solution[16].

One particularly well-studied organometallic carbonyl complex that is promising as a vibrational probe is the piano-stool cyclopentadienyl manganese tricarbonyl (CMT)[17-20], also known as cymantrene (**Fig 5.1a**). Due to the versatility of its Cp ring[21], CMT is readily functionalized using chemistry adapted from ferrocene. CMT and its

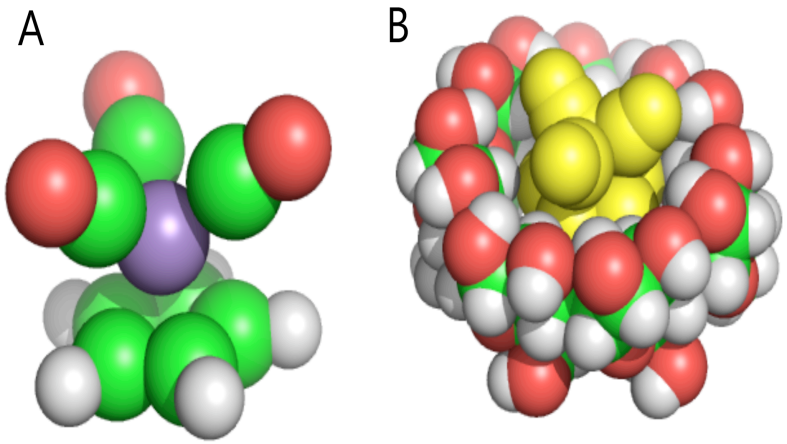

Figure 5.1. Three dimensional view of (A) cyclopentadienyl manganese tricarbonyl (CMT) and (B) β-cyclodextrin CMT (cdCMT) complex where the cyclopentadienyl ring of CMT is centered in the hydrophobic cavity.

derivatives are stable, finding use as an anti-knocking additive in gasoline[22]. CMT has been investigated in the form of bioconjugates with biotin[23-25] and with cell penetrating peptides as a means of introducing cytotoxic carbon monoxide to cancer cells. We are investigating the suitability of a suite of metal carbonyl complexes for use as biophysical probes, including cymantrene due to its relatively wide array of proven applications.

In addition to using 2DIR to characterize the solvent-dependent dynamics of CMT in a range of alcohols, we have also taken advantage of the fact that CMT and other organometallic metal carbonyls with cyclopentadienyl and benzyl ligands form stable inclusion complexes with various cyclodextrin hosts. Specifically, CMT binds strongly to β-cyclodextrin (β-CD)[19, 26-28], which serves as a single-molecule cavity allowing us to characterize the dynamical consequences of nanoscale partial confinement. Cyclodextrins are versatile hosts capable of solubilizing nonpolar guests by virtue of the amphiphilic nature of their hydrophobic cavities and hydrophilic exteriors. The 1:1 inclusion complex between β-CD and CMT (denoted here cdCMT)

provides an essentially minimal model of a binding site, while still enabling the same systematic variation of solvent in order to isolate the influence of confinement (**Fig. 5.1b)**. Although a crystal structure does not currently exist, we characterize the cdCMT structure with the carbonyls being exposed to the solvent.

To assess and calibrate the range of structure and dynamics that can be monitored using metal carbonyl probes, here we report investigations using ultrafast 2DIR spectroscopy to systematically characterize cymantrene in a series of linear alcohols. We have also characterized the influence of forming a 1:1 inclusion complex with β-CD as a model for nanoconfinement. In both cases, although we find the FTIR spectrum to depend only weakly on the alcohol chain length, the time scales of spectral diffusion show a clear viscosity dependence as revealed by 2DIR spectroscopy. The formation of the inclusion complex induces no discernible changes to the carbonyl spectral bands, but it does accelerate the sampling of the available microscopic solvation environments while maintaining the viscosity dependence of the uncomplexed CMT. It would thus appear that solvation dynamics, as reported by the spectral diffusion of the vibrational probe, is composed of a dynamical component governed by motional fluctuations as well as a topological contribution due to the size of the environmental phase space. This latter contribution should be a measure of the configurational entropy, and we attempt to make a simple model that can correlate solvent accessibility to configurational entropy.

We find that the spectral diffusion of the cdCMT complex is faster than that of CMT in three different alcohol solvents, despite simulation results showing the

reorientation of alcohol molecules to be slower in the vicinity of β-CD. We attribute this surprising finding to changes in the size of the solvation conformational space, which we argue is proportional to the number of solvent molecules in the solvation shell. Adequately determining the number of solvent molecules that contribute to the microenvironment is a complex problem; as a proxy we use a geometric property of the probe, the solvent-accessible surface area (SASA). In order to test the consistency of this theory, we compare these results to previous work on another manganese carbonyl, dimanganese decacarbonyl ($Mn_2(CO)_{10}$, DMDC), finding that spectral diffusion of the larger SASA of DMDC is indeed slower in comparison to CMT and cdCMT over a series of alcohol solvents, which is consistent with our geometrical model. The ability to associate a purely geometrical factor with spectral diffusion will allow us to use spectral diffusion in general solvents—which may not be amenable to systematic variation—as an essentially quantitative proxy for the local viscosity, having modeled and removed the shape-dependent non-dynamical component. Applications of this approach should be particularly suitable for studies of biological membranes or protein aggregates using bioconjugated metal carbonyl vibrational probes.

5.2 Experimental and Simulation Methods

5.2.1 2DIR. Experimental 2DIR methodology and its theoretical foundations have previously been described elsewhere[30-33]. The aspect of the technique that is most relevant to the present study is the ability to monitor the decay of transient spectral inhomogeneity by constructing the so-called *inhomogeneity index*, I_{in}. When implemented

using a fully non-collinear beam geometry, three input electric fields E_1, E_2, and E_3, separated by delays t_1, t_2, and t_3 produce two different background-free signals $E_{\pm}$, with wavevectors $k_{\pm} = \pm k_1 \mp k_2 + k_3$, corresponding to the rephasing (–) or non-rephasing (+) responses. It is well established that a properly phased linear combination of the complex rephasing and non-rephasing signal fields yields an absorptive 2D spectrum. Often the full rephasing spectrum contains more information than is needed in order to characterize the spectral dynamics, particularly in the case of the relatively well-resolved bands of metal carbonyl complexes. Since only the rephasing signal is capable of producing a photon echo, the frequency memory of a probed transition can be monitored by computing the normalized difference between rephasing amplitude (A_-) and nonrephasing amplitude (A_+) signals as[34]:

$$I_{in} = \frac{A_- - A_+}{A_- + A_+} \tag{1}$$

We measure the rephasing and nonrephasing amplitudes by integrating the absolute value signal over w_1 and w_3 between 1910 cm^{-1} and 1960 cm^{-1}. I_{in} is proportional to the normalized frequency-frequency correlation function (FFCF) that underlies the optical line shape function and relates directly to microscopic solvation dynamics. In the condensed phase, microscopically distinct environments can induce transient frequency shifts, and as an excited molecule stochastically samples the available sub-ensembles, it loses correlation with its initially excited frequency. This loss of correlation is often modeled by a narrowing term and a sum of exponential decays as[35, 36]:

$$C(t) = \langle \delta\omega(0)\delta\omega(t) \rangle = \frac{\delta(t)}{T_2} + \sum_i \Delta_i^2 \, exp\left(\frac{-t}{\tau_i}\right) \tag{2}$$

where $dw(t)$ is the instantaneous frequency fluctuation from the average, and the angled brackets denote an ensemble average. The narrowing term, T_2, incorporates the motional narrowing, pure-dephasing, vibrational lifetime, and orientational relaxation. The number of exponential contributions needed to properly fit the FFCF is an indication of the complexity of the system.

We studied CMT and the inclusion complex with b-cyclodextrin (cdCMT) in a series of solvents. For CMT alone, 2DIR spectra were recorded in linear alcohols ranging from methanol to 1-hexanol, and cdCMT was studied in methanol, ethanol, and 1-butanol only, since b-cyclodextrin was found to be insoluble in 1-pentanol and 1-hexanol. In the case of CMT in methanol, which shows the most rapid spectral diffusion, rephasing and nonrephasing 2DIR data were collected in waiting time (t_2) steps of 100 fs from 0.1 to 1 ps, and in steps of 250 fs from 1 to 5 ps, and in steps of 500 fs from 5 ps to 15 ps. In all other solvents, spectra were recorded with waiting time steps of 250 fs. A full description of the fitting methods is provided in the Supplemental Information.

5.2.2 Sample preparation. CMT and β-cyclodextrin were purchased from Sigma Aldrich and were used without further purification as were all solvents. The sample cell consisted of a 100 μm Teflon spacer with 3-mm thick CaF_2 windows. Samples were prepared to give ~3 mM concentration. Inclusion complexes of CMT in b-CD were made by following a previously published protocol[26]. Differential thermal gravimetry was used to confirm the effectiveness of the protocol (**Fig. 5.2**). β-CD decomposes at two temperatures separated by more than 200°C, the lower temperature decomposition is thought to

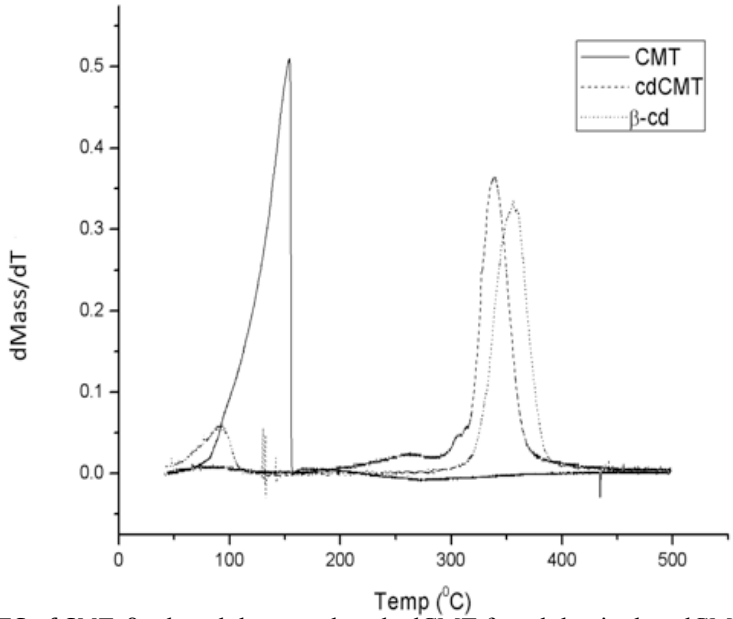

Figure 5.2 The DTG of CMT, β-cd, and the complexed cdCMT found that in the cdCMT complex the CMT decomposes at a temperature 200°C hotter than that of lone CMT.

be the dehydration of the β-CD cavity, while CMT decomposes at a single temperature comparable to the β-CD dehydration. The cdCMT also decomposes at a single temperature that is comparable to the higher temperature β-CD decomposition. The CMT displaces the water from β-CD cavity and the β-CD protects the CMT from decomposition until the β-CD itself decomposes. While in solution, the stability of the complex was determined using the 1650 cm^{-1} band, which appears only for the complex (**Fig. 5.3**). A conjugated C=C diene produces a strong peak at 1650 cm^{-1} while an aromatic ring has no such peak. The confining constraints of the β-CD breaks the aromatic nature of the cyclopentadienyl ring symmetry forcing the ring to take the characteristics of a conjugated diene producing the 1650 cm^{-1} peak.

The structure of the cdCMT is not yet known, but due to the simplicity of β-CD, we can deduce the structure of cdCMT. β-CD is a cyclic hepta dextrin where the inner

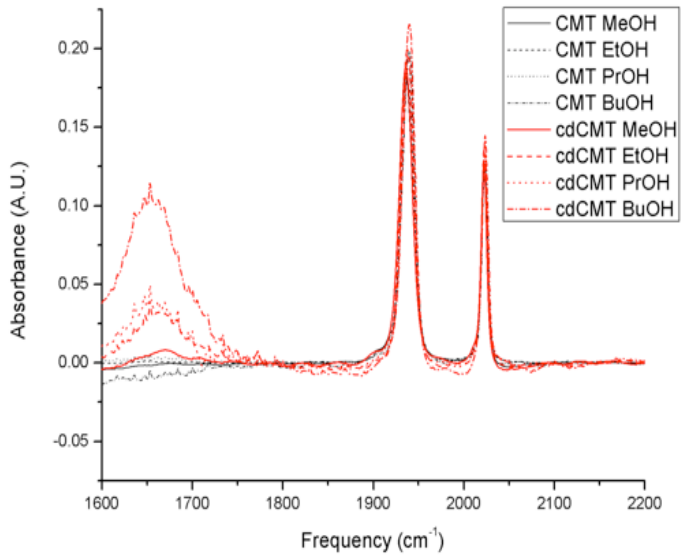

Figure 5.3 The FTIR spectrum of the carbonyl modes have only minimal changes with the introduction of the β-CD. Yet, there is an additional peak at 1650 cm^{-1} that is thought to arise from the confining space of β-CD breaking the cyclopentadienyl symmetry.

core is a hydrophobic core while the rims of the β-CD is lined with primary and secondary hydroxyl groups, making the overall structure hydrophobic. Due to the hydrophobic nature of the cyclopentadienyl ring, it is presumed that the cyclopentadienyl ring sits in the hydrophobic cavity leaving the carbonyls exposed to the solvent. The similarities of the FTIR of CMT and cdCMT in various solvents and the similar linear spectral diffusion time constant trends suggest that the carbonyls are indeed exposed to the solvent. Additionally, we see that cdCMT introduces a peak at 1650 cm^{-1} (**Fig. 5.3**) not found in CMT that we assign to the broken symmetry of the cyclopentadienyl ring that arises from the cyclopentadienyl ring being situated in the b-CD cavity. Calculating cdCMT's SASA, we assume the depth of cyclopentadienyl ring is centered in the hydrophobic core of β-CD with the carbonyls exiting the larger opening. Since β-CD is only partially soluble in alcohols, the concentration is limited by saturation. Before data collection, cdCMT samples were centrifuged and filtered to limit scattering.

5.2.3 Molecular dynamics. We implemented MD simulations of β-CD in methanol to test the dependence of the reorientation time scales on the presence of β-CD. Prior to production MD simulations, the methanol/β-CD box was energetically minimized, followed by a 100 ps NPT simulation utilizing the CHARMM software package[37]. Production simulations were run for 200 ps at 2 fs time steps that produced a trajectory with 10 fs time steps. Methanol was previously parameterized[38] and we obtained the β-CD parameters using the Multipurpose Atom-Typer for CHARMM (MATCH)[39].

5.2.4 SASA calculations. All SASA calculations were performed in VMD 1.8.7[40]. For the cdCMT SASA where the crystal structure is unknown, we assume the depth of the hydrophobic cyclopentadienyl to be centered in the β-CD cavity.

5.2.5 Fitting Procedures. We fit the data presented in this paper to a single exponential, $I.I. = \exp(-t/\tau_{sd}) + c$ using the Origin 8 software package. Excluding methanol, we collected the t_2 data at 250 fs time steps beginning at 0, and extending to 15ps. We did not include $t_2 = 0$ in the exponential fits due to the unreliability of overlapping pulses. Due to the fast decay of methanol, we sampled early times of methanol at 150fs t_2 time steps and 250 t_2 time steps at latter times. The data recorded with uneven spacing were interpolated to avoid biasing the exponential fits to early t_2 times.

5.2.6 Simulations. One of the goals of this work is to link 2D-IR observables such as spectral widths and spectral diffusion to conformational entropy. Essentially, we seek to establish spectral diffusion as a means to quantify the extent of the solvation configuration space using a minimal model of a quasi-dipolar solvent shell. This simple

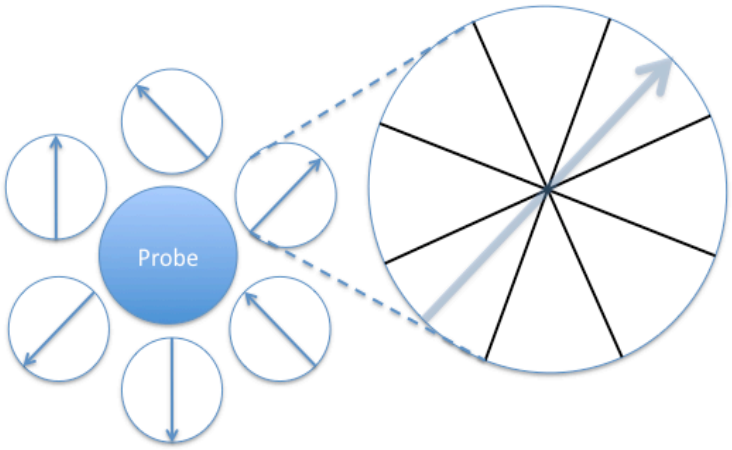

Figure 5.4 To facilitate the use of the dipole orientation, $\varphi_{k,\tau}$, in computing the microenvironment, the dipole orientation is represented as discrete steps. Although realistic solvent molecules do not have finite orientations, due to computational time constraints and the need to enumerate all possible solvent configurations, we limit the dipole orientation to range from -10 to 10.

model relies on purely geometric aspects of the isolated components, such as the number of solvent molecules participating in the creation of the microenvironment. From such a model we extract apparently general requirements that must be met in order to reproduce the experimentally observed solvent dependent spectral diffusion measurements reported here. In the present study, we need to treat separately three distinct aspects of the system. The first is the solvent exposure of each solute molecule: that is, the ten terminal carbonyls in DMDC, the three carbonyls in CMT, and the three partially confined carbonyls in cdCMT. The second aspect is the solvent molecular size, which becomes larger with increasing chain length. The third consideration is the dynamics of the solvent, which if characterized by relative viscosity, slows with increasing chain length. To summarize the experimental results, for each solute, the relative spectral diffusion time scales follow the viscosity trend through a series of solvents; comparing different solutes in the same solvent, the time scales correlate to solvent accessibility. Hence, we require a model that allows us to consider in isolation

the role solvent accessibility plays in determining the overall spectral diffusion dynamics.

We model the trend of spectral diffusion time scales while altering the number of participating solvent molecules in order to capture the variation in solvent accessibility among the three solutes studied. To simulate the trends of spectral diffusion time scales, we implemented the following simple model. All solvent molecules are equally distant from the probe, a single variable $\varphi_{k,\tau}$ represents the orientation of a given dipole (**Fig. 5.4**), and the energy surface of the dipole transitions is flat and smooth. Under these assumptions, only the orientation of the solvent dipole alters the solute's local environment, and therefore the spectral diffusion timescales. The dipole orientation is modeled as a site-correlated Gaussian Markov process. We represent the angular velocity ω of the solvent molecule *k* at discrete time steps, τ, according to equation 3:

$$\omega_{k,\tau} = \mu \cdot \omega_{k,\tau-1} + \boldsymbol{W}_{k,\tau} \tag{3}$$

where μ represents the memory level of the system and $\boldsymbol{W}_{k,\tau}$ is the random Gaussian process; correlation between solvent molecules is built into $\boldsymbol{W}_{k,\tau}$ by multiplying the Cholesky decomposition of the covariance matrix $\mathbf{M}_{i,j}$ (eq. 4) by a set of uncorrelated Gaussian distributed random fluctuations, **s** (eq. 5). The reorientation correlation of neighboring dipoles arises through energetic constraints[41], and can be modeled with a Monte Carlo simulation. To mimic a dipolar liquid with a distance-dependent intermolecular interaction, we set the covariance matrix's off diagonal elements proportional to the inverse distance between solvent molecules. There is an overall scaling factor, α. $\boldsymbol{W}_{k,\tau}$ is defined such that it has a mean of zero, variance of σ^2, a

temporal correlation of $\langle W_{k,0} W_{k,t} \rangle = \delta(t)$, and the correlation between solvent molecules is given by the covariance matrix $\mathbf{M}_{i,j}$.

$$M_{ij} = \delta_{ij} + \left(1 - \delta_{ij}\right) \frac{\alpha}{r_{ij}} \tag{4}$$

so that

$$W_{k,\tau} = chol\left(\boldsymbol{M}_{ij}\right) \cdot \boldsymbol{s} \tag{5}$$

The orientation of solvent molecules begin the simulations at $\theta_{initial}$, making the trajectory of a specific solvent molecule's orientation, $\theta_k(t)$, the sum of $\omega_{k,\tau}$ from $\tau = 0$ to $\tau = t$:

$$\theta_k(t) = \sum_{\tau=0}^{t} \omega_{k,\tau} + \theta_{initial} \tag{6}$$

θ has rigid boundary conditions enforced such that the projection $\theta_k(t) > \theta_{max}$ is corrected to $2\theta_{max} - \theta_k(t)$ (as is the boundary condition at θ_{min}) and the subsequent movements, $\omega_{k,\tau>t}$, are reversed. Since we ultimately analyze the time dependence of the microenvironment distribution, we must encode each microenvironment uniquely. This encoding requires the orientation of each solvent molecule to be represented as an integer, which is accomplished by binning the values of $\theta_k(t)$, producing $\varphi_{k,\tau}$. The number of bins is arbitrary, but the maximum number of bins is limited by the computational time required. For our simulations $10 > \varphi_k(t) > -10$. $\varphi_k(t)$ contains the solvent molecule orientations at each time step and is then used to determine the microenvironment the probe experiences. We define the microenvironment through two different methods. In the first, which we denote arrangement *independent* (AI), we

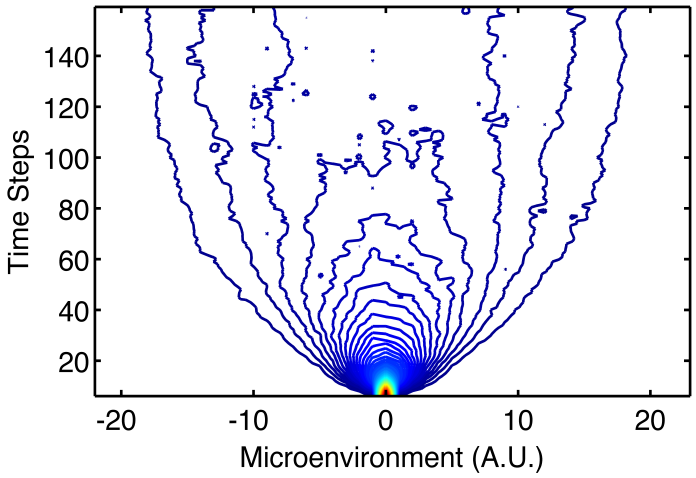

Figure 5.5 The microenvironment distribution function, $D(m;t)$, plotted against time. All simulations begin with the same microenvironment but diffuse away from it through the course of the simulation. We use R(t), Eq. (7), to measure extent of the microenvironment diffusion.

perform a simple sum over all the solvent orientations: $E(t) = \sum_k \varphi_{k,t}$. The second treatment is arrangement *dependent* (AD), where each distinct arrangement of orientations is considered a distinct microenvironment and inherently produces a larger number of distinct microenvironments.

Simulations were run iteratively, producing an ensemble of microenvironment trajectories. Figure 5.5 shows the AI microenvironment distribution function $D(m;t)$, where m represents a specific microenvironment and at time t. At t = 0, $D(m;t)$ is a delta function at $\theta_{initial}$ and broadens over time. Spectral diffusion is extracted from $D(m;t)$ through the sum of the residuals between the distribution at each time step and the distribution at equilibrium $D(m;\infty)$

$$R(t) = \sum_m |D(m;t) - D(m;\infty)| \tag{7}$$

The relaxation, $R(t)$, is the measure of how the microenvironment ensemble diffuses away from the initially prepared state at $t = 0$ and we use the half life of $R(t)$ as a

measure of spectral diffusion.

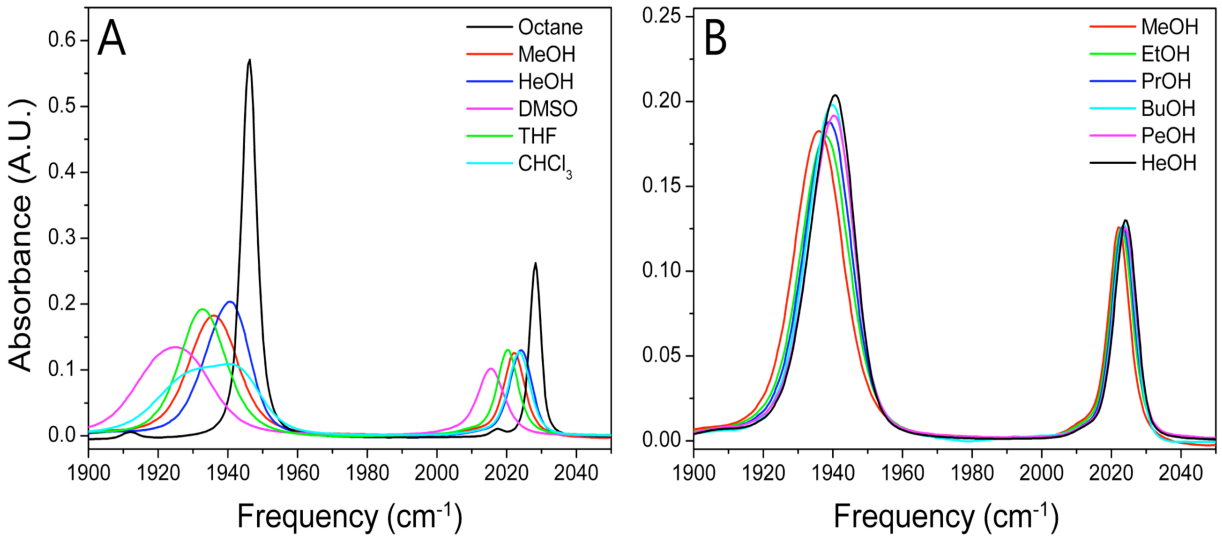

Figure 5.6 Area-normalized experimentally measured FTIR spectrum of CMT in various solvents.

5.3 Results and Discussion

5.3.1 CMT and cdCMT in linear alcohols. To assess the general solvent sensitivity of CMT, we measured FTIR spectra of CMT in multiple solvents with varying polarities (**Fig. 5.6a**). In these solvents, CMT exhibits the expected red shift with increased polarity observed in many metal carbonyl complexes. In dimethyl sulfoxide, the most polar solvent examined, the symmetric stretch band is shifted 13 cm^{-1} to the red relative to its position in octane, the least polar solvent studied, and the asymmetric band is shifted by 21 cm^{-1}. In all measured solvents, the asymmetric peak is both broader and greater in amplitude than the symmetric band. The difference in amplitude is attributed to the fact that the asymmetric band is composed of two nominally degenerate modes. With the exception of $CHCl_3$, we see no noticeable splitting of the degenerate asymmetric band in the solvents measured. This lack of resolvable splitting may simply be due to the fact that the spectral broadening is a more pronounced effect than is the splitting induced by

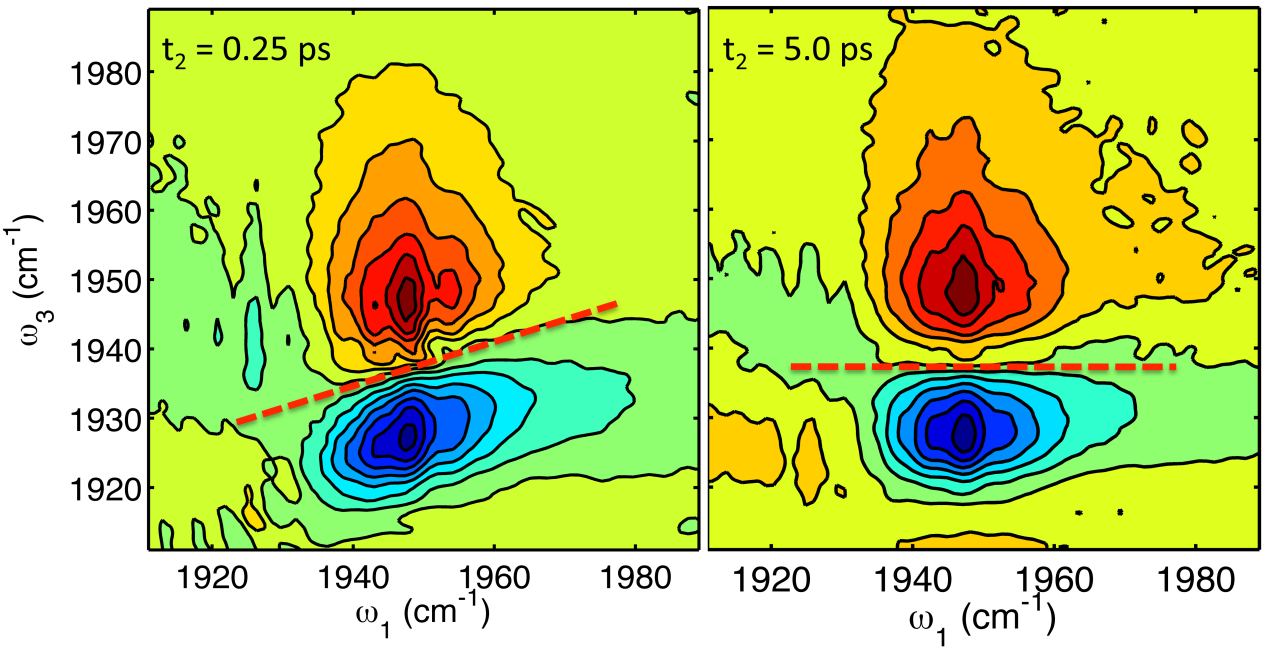

Figure 5.7 2DIR Spectra of CMT's asymmetric peak in methanol at t_2 time steps of (A) 0.25 ps and (B) 5 ps. Each spectrum consists of 2 peaks, a positive valued fundamental peak at 1947 cm^{-1} and the anharmonic peak at 1928 cm^{-1}. At early times, the nodal line (NL) in red is slanted due to inhomogeneous broadening. At later times, the NL has no slope due to a loss of memory of the original vibrational frequency.

disorder. It is worth noting here that all three of CMT's carbonyl vibrations are IR active in the gas phase, so there are no modes that are exclusively Raman active that could become IR active by the symmetry lowering induced by the polar solvents[42, 43]. This latter point is in contrast to our observations in DMDC, which has 4 nominally IR active modes, 6 Raman active modes, and no modes that are both IR and Raman active.

While the linear alcohols follow the same polarity trend (**Fig. 5.6b**), the band shifts are far less pronounced. Relative to 1-hexanol, in methanol CMT's symmetric and asymmetric bands are shifted only 2 cm^{-1} and 5 cm^{-1}, respectively. The asymmetric band widths in methanol and in hexanol differ by less than 2 cm^{-1}, and differences are essentially absent for the symmetric band. At the level of one-dimensional spectroscopy, the lack of apparent sensitivity of CMT would appear to limit its utility as

a probe of its local environment. As has been shown in several other examples, however, 2DIR spectroscopy reveals the dynamical differences that are hidden in 1D spectra[10, 15] The 2DIR spectrum spreads information over two frequencies exposing spectral features which can then evolve with increased waiting time (t_2).

Figure 5.7 shows the 2D spectrum of CMT in methanol, focused on the diagonal region of the spectrum corresponding to the asymmetric band at 1947 cm^{-1}. The region of the spectrum with negative amplitude contours (mostly red) correspond to the ground state bleach and stimulated emission pathways, and reflects the transitions probed in the linear FTIR spectrum. The band of opposite sign, immediately below the diagonal, corresponds to excited state absorption with frequencies red-shifted due to vibrational anharmonicity. In methanol, at early t_2, the nodal line (NL) separating the positive and negative features is slanted, reflecting an inhomogeneously broadened contribution to the absorption line-shape. The NL slope indicates that the solvation environment around the CMT solute is capable of shifting the fundamental transition frequency, leading to a temporary correlation between excited and detected frequencies. Increasing the waiting time decreases the slope as the probe samples the full range of solvation environments and loses its initial frequency correlation. This loss of memory of the original frequency is caused by spectral diffusion.

We measure the vibrational lifetime of CMT in hexane by fitting the rephasing peak volume to a to a biexponential giving two decay times of ~1 ps and 42 ps, with the slower decay constant assigned to the vibrational lifetime. Previously we have measured somewhat longer ~70 ps vibrational lifetimes for DMDC in alcohols, where

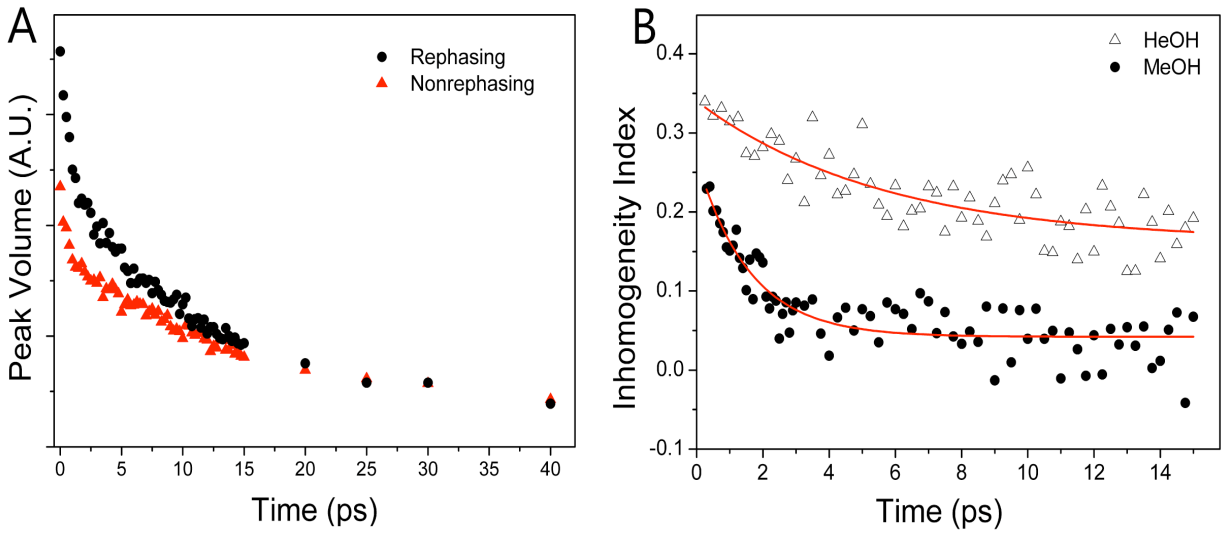

Figure 5.8 (A) The asymmetric peak volumes of the rephasing and nonrephasing spectra measured by integrating the signal absolute value over ω_1 and ω_3 between 1910 cm^{-1} and 1960 cm^{-1}, which are used in Eq. 1 to calculate (B) the inhomogeneous index at each t_2 time step. The inhomogeneous index of HeOH decays noticeably slower than that of MeOH and is offset for ease of viewing.

the carbonyls stretches are spectrally isolated and only very weakly coupled to the lower frequency modes of the molecule. In CMT, however, there is a more direct coupling between the CO units and the cyclopentadienyl ring through a bending mode that involves the Cp hydrogens and the CO ligands. A similar mode is present in the benzyl chromium analog, h^6-$C_6H_6Cr(CO)_3$ which also shows a <50 ps vibrational lifetime even in nonpolar solvents.

We use the rephasing and nonrephasing peak volumes to extract spectral diffusion time scales by computing the inhomogeneity index (Eq. 1). At early waiting times, there is an imbalance between the peak volumes of the rephasing and nonrephasing spectra that is due to the frequency memory still present in the ensemble of oscillators (**Fig. 5.8**). At later t_2 times, the imbalance in peak volume between the rephasing and nonrephasing spectra becomes indistinguishable, indicating the oscillators have fully sampled the available microenvironments. Plotting the

inhomogeneity index curves for CMT dissolved in methanol and 1-hexanol reveals the distinct solvation environments and associated difference in dynamical timescales of spectral diffusion. In this paper, all inhomogeneous index curves are fit to single exponential ($A\exp[-t/\tau_{\text{spec. diff.}}] + B$) decays starting at waiting times of 0.25 ps. A summary of the extracted spectral diffusion time constants is shown as a function of solvent viscosity in **Figure 5.9**. Although the decay rate of the inhomogeneity index is dependent on the solvent, an understanding of what factors contribute to spectral diffusion are still unclear and will be explored further below. Using DMDC in the same linear alcohol series, we have previously found the spectral diffusion time constants to depend linearly on viscosity[10]. Here, CMT follows the same trend of slowed spectral diffusion with increased viscosity, indicating the solute's ability to sample solvation environments is hindered by solvent friction. We also see a general trend where the standard error of the exponential fit increases as spectral diffusion time constant increases. This is not surprising; as t_2 increases, the signal to noise ratio will decrease due to the vibrational lifetime of CMT, which is essentially solvent independent. If the spectral diffusion time constant is larger, the additional noise at latter t_2 measurements will reduce the signal to noise ratio of the extracted inhomogeneous index.

Cyclodextrin host-guest inclusion complexes have been studied extensively as models for nanoconfinement, mimicking the hydrophobic active sites of enzymes, and as delivery vehicles for nonpolar drug molecules. In order to determine the viability of CMT as a probe, we measured the FTIR spectra and spectral diffusion time constants of CMT complexed with β-CD. Although structurally different, β-CD and linear alcohols

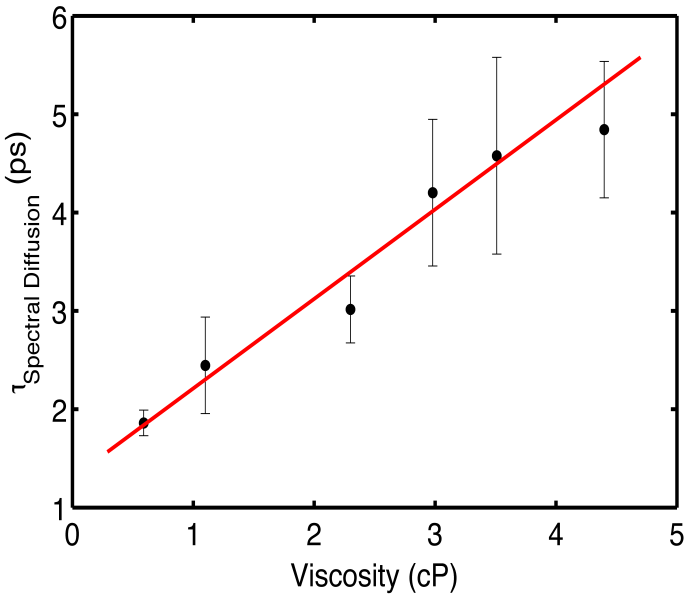

Figure 5.9 The spectral diffusion time scales of CMT in a series of alcohol solvents plotted against viscosity of the solvent with the corresponding linear fit (red). The standard error tends to increase as the spectral diffusion time constant increases.

are chemically quite similar. The lone hydroxyl functional group on its alkane chain is a hydroxyl group, while the sugars of β-CD are composed of simple alkane chains and hydroxyl groups with ethers connecting adjacent sugars. From the series of four alcohols (cdCMT is insoluble in alcohols with five or more carbons), which can be considered a spectral and dynamical calibration, we expect few, if any, changes in the FTIR spectrum upon formation of the inclusion complex. Indeed, the formation of an inclusion complex has a negligible effect on the linear FTIR spectrum in the carbonyl region (**Fig. 5.10**). Interestingly, there is a pronounced change in the region of the spectrum associated with aromatic ring modes(**Fig. 5.3**), which might reflect some distortion of the Cp ring. It is surprising that distortions of the ring do not manifest themselves through any changes in the carbonyl frequencies. Moreover, these bands do not appear to influence the vibrational dynamics of the terminal carbonyl stretches since

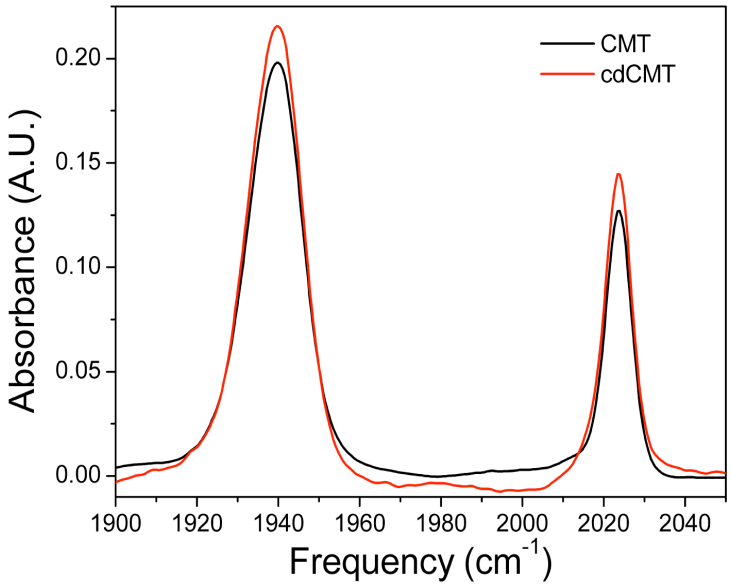

Figure 5.10 The FTIR of CMT (black) has only minimal differences when complexed with β-cyclodextrin (red), demonstrating the insensitivity of the linear IR spectrum of the carbonyl modes to the presence of the inclusion complex.

the measured vibrational lifetimes are unaffected by the presence or absence of the inclusion complex (26.9 and 27.6 ps for CMT and cdCMT respectively).

In contrast to the FTIR spectrum's lack of sensitivity to complexation, we might expect to observe changes in the spectral diffusion dynamics because of both the partial nanoconfinement of the β-CD cavity as well as its structural and dynamical perturbation of the solvent. In the vicinity of the hydroxyl groups, the availability of accessible hydrogen bond donors and acceptors may impose minor disruptions to the alcohol hydrogen bonding network. Similar to both CMT and DMDC, inhomogeneity index decays in the accessible solvents (**Fig. 5.11**) show that spectral diffusion of the inclusion complex generally exhibits linear viscosity dependence. For the case of cdCMT in ethanol, where there is substantial deviation from the linear trend, we found the spectral diffusion time constant to be dependent on the age of the solution.

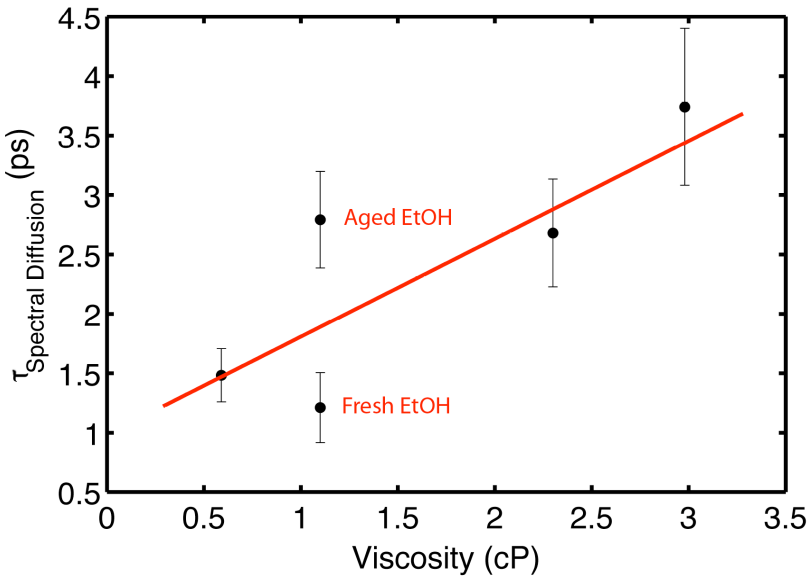

Figure 5.11 The spectral diffusion time constant of cdCMT in a series of alcohol solvents plotted against viscosity of the solvent with its corresponding linear fit (red). The fit constant of ethanol is plotted for both the fresh (immediate after mixing) and aged (~3 hours) samples.

Measurement of the spectral diffusion in ethanol immediately after the complex was dissolved resulted in time constants that were much smaller (faster) than all non-ethanol samples observed. We note that we require 90 minutes to record 120 2DIR spectra used in the analysis. After waiting ~3 hours, the spectral diffusion time was found to increase to a value comparable to that of CMT alone in ethanol. A sample saved for one week formed a precipitate. Ethanol has previously been shown to form a unique complex with β-CD where one ethanol sits in the cavity and two ethanol molecules form a cap on the β-CD[44]. Thus it is possible that the differences in spectral diffusion are due to the process of the ethanol expelling CMT from the cavity and forming this unique complex. Although this observation is interesting, since it involves a particular structural transformation of the inclusion complex resulting in a loss of our probe, we will not address this issue further. When computing a fit for the cdCMT complex, ethanol was not included.

	Solvent	$\tau_{spec.\ diff.}$ (ps)	Standard Error
DMDC	Methanol	2.67	0.38
	Ethanol	2.98	0.6
	Propanol	4.13	0.79
	Butanol	4.67	0.5
	Pentanol	5.04	0.47
	Hexanol	5.33	0.6
CMT	Methanol	1.86	0.13
	Ethanol	2.44	0.49
	Propanol	3.01	0.34
	Butanol	4.2	0.75
	Pentanol	4.58	1.04
	Hexanol	4.84	0.69
cdCMT	Methanol	1.48	0.22
	Ethanol (0 hrs)	1.21	0.29
	Ethanol (>3 hrs)	2.79	0.41
	Propanol	2.68	0.45
	Butanol	3.74	0.66

Table 5.1 The spectral diffusion time constant fits and the correspond standard errors of DMDC, CMT, and cdCMT in all solvents. Note, the standard errors tend to increase with the spectral diffusion time scales.

Comparing the spectral diffusion time constant of the probes in the same solvents, we find the trend CMT > cdCMT in every solvent examined, excluding cdCMT in ethanol, discussed above. In methanol, the error bars of the spectral diffusion time constants are distinctly separated (Fig 5.12), but in all other measured solvents the standard errors begin to overlap (Table 5.1). The standard error of the fits tend to increase with the spectral diffusion time constant because a larger spectral diffusion time constant is dependent on measurements at latter t_2 delays and the signal to noise ratio decreases at latter t_2 delays due to the vibrational life time of the probe. Although

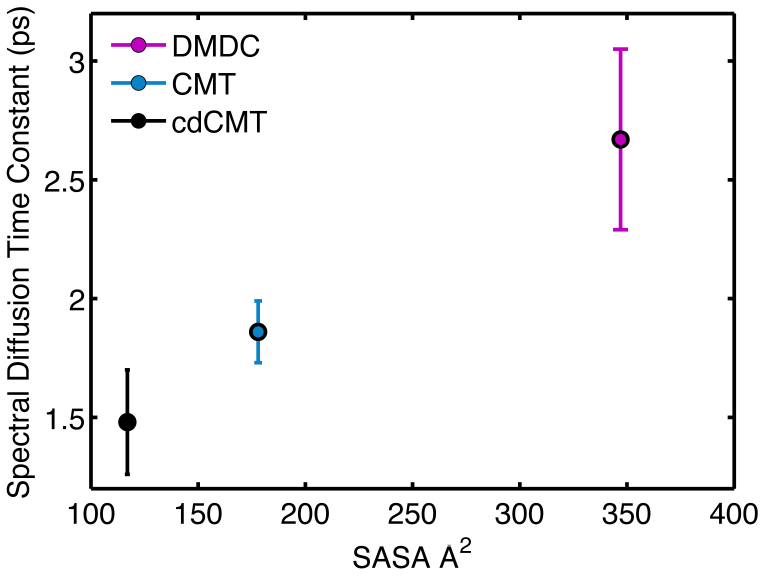

Figure 5.12 The spectral diffusion time constants of cdCMT, CMT, and DMDC in methanol and their standard errors. Because of the fast spectral diffusion, the three time constants are significantly distinct. Due to the vibrational lifetime, as time constants increase the standard errors correspondingly increase creating overlap in the measurements (Table 5.1).

the error bars overlap in non-methanol solvents, the consistency of the CMT > cdCMT trend give further confidence to the trend. To quantify this trend, we collect the linear fits for our results for alcohol-dependent spectral diffusion of CMT, and cdCMT in Table 5.2, which highlights that while the slopes are nearly identical (2% difference), the intercept of CMT is nearly 50% larger than that of cdCMT. Hence, we propose that the slope reflects the viscosity dependence of solvent dynamics, whereas the intercept is linked to the diversity of microscopic solvation environments experienced by the probe. In the following sections, we eliminate the possibility that solutes themselves distort the solvent dynamics to create the observed trends and we use a simple model of solvation to motivate an intuitive interpretation of these results, specifically the importance of the zero-viscosity offset and its relation to the probe's solvent-accessible surface area (SASA).

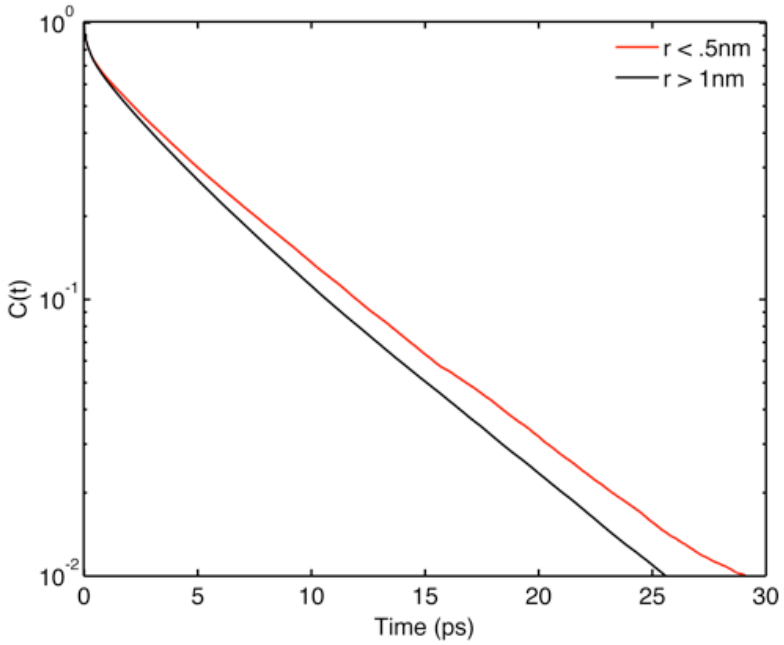

Figure 5.13 The reorientational correlation function of methanol near β-CD and neat methanol calculated with MD simulations.

To understand how the introduction of the β-CD distorts the spectral diffusion time constant, we examine how the b-CD could distort the solvent dynamics near the probe. Two solute attributes that have been shown to alter the solvent dynamics near the solute are the ratio of the solute and solvent Van der Waals volumes[45-46] and the non-bonded interactions between the probe and solvent[47-51]. Increasing the Van der Waals volume of the probe and increasing the strength of interactions between the probe and solvent tend to slow the dynamics of the solvent molecules. The Van der Waals volume[52] of cdCMT is substantially larger, 1117 Å^3, than that of CMT, 163 Å^3. Although the difference in size between cdCMT and CMT is substantial enough to change the solvent dynamics, we would expect the size of cdCMT to slow the dynamics of solvent molecules. Instead, the experimental data indicates that cdCMT exhibits the

faster spectral diffusion than CMT.

To test the influence of the large β-CD and its non-bonding interactions on its immediate solvation environment, we implemented MD simulations, focusing on how β-CD alters the reorientation dynamics of methanol (Fig 5.13). These MD simulations are of β-CD alone because of the difficulty in producing accurate parameters for CMT. We use the correlation function $C_2(t) = \langle P_2[\boldsymbol{e}(t) \cdot \boldsymbol{e}(0)] \rangle$ as a measure of the reorientation dynamics of surface and bulk methanol, where **e** represents the vector that defines the OH bond, and P_2 is the second Legendre polynomial. We differentiate between surface and bulk methanol by the distance *r* between the methanol oxygen and the nearest b-CD atom at t = 0 of the section of the trajectory used for the correlation function. A "surface" methanol is defined such that r < 0.5 nm and a "bulk" methanol such that r > 1 nm. Fitting the correlation functions to biexponentials, the slow time constants yield 6.36 ps and 5.71 ps for surface and bulk solvent molecules respectively, which compares favorably to the 5 ps reorientation of bulk methanol observed with NMR[53-55]. We found the reorientation of methanol near b-CD to be ~10% slower than neat methanol; in contrast, the spectral diffusion in the presence of b-CD (cdCMT) is actually ~20% faster than CMT in neat methanol.

The relative Van der Waals volumes and the MD simulations suggest that the addition of the b-CD would slow the dynamics near the probe, yet we see that the b-CD speeds the spectral diffusion. Here, we propose that the faster spectral diffusion time scale of cdCMT is due to the b-CD reducing the number of solvent molecules participating in the creation of the probe's microenvironment. We take the solvent

accessible surface area (SASA) to be a proxy measure of the number of participating solvent molecules. Although the x-ray crystal structure of cdCMT has not yet been obtained, we have determined that b-CD and CMT form a complex and the relative orientation of CMT exposes the carbonyls to the solvent. Assuming the hydrophobic arene ring of CMT to be situated in the center of the b-CD, the SASA of cdCMT carbonyls is 117 Å^2, which is significantly lower than that of CMT, 178 Å^2.

	Intercept (ps)	Slope (ps/cP)	R^2	SASA (Å^2)
DMDC	2.67±.07	0.84±.03	0.997	347
CMT	1.30±.25	0.92±.11	0.950	178
cdCMT	0.87±.42	0.90±.19	0.943	117

Table 5.2 Parameters of linear fits to the alcohol solvent dependent spectral diffusion time scales, with the corresponding solute solvent accessible surface area.

5.3.2 Comparison to DMDC. We test the role of SASA in altering the spectral diffusion time scale by comparing the spectral diffusion of CMT and cdCMT to dimanganese decacarbonyl ($Mn_2(CO)_{10}$, DMDC) with a SASA of 347 Å^2 in the same solvents. In all solvents, DMDC has a larger spectral diffusion time constant than both CMT and cdCMT, which preserves correlation between the SASA and the spectral diffusion time constant. In methanol, the favorably short spectral diffusion permits statistically significance in the solute-dependent spectral diffusion times, (**Fig. 5.12**), but in all other solvents the error bars begin to overlap (Table 5.1). Again, to quantify the spectral diffusion time constants in all solvents, we fit the measurements to a linear fit Table 5.2. The slope of the fit is within 10% of CMT and cdCMT while the y-intercept of the

DMDC fit is nearly double that of cdCMT.

Although DMDC is distinctly different than CMT, the portion of both molecules probed in our IR measurements are manganese carbonyls suggesting the non-bonding interactions of these regions will be comparable and will have minimal impact in the spectral diffusion time scales. The increase in the number of carbonyls of DMDC compared to CMT, 10 and 3 respectively, has the potential to alter the spectral diffusion time scales due the ability of carbonyls to excitonically couple. It is common to model vibrational eigenstates as excitonically coupled local modes, and we have found this approach to work particularly well for the carbonyl stretches in transition metal complexes[10]. In the case of DMDC, we have found good agreement between the predicted and measured linear absorption spectrum using simple stochastic Gaussian site energy disorder, including faithful reproduction of the disorder-induced IR activity of otherwise IR-inactive modes. One of the universal features of excitonic systems, whether vibrational or electronic, is the effective shielding from environmental fluctuations by virtue of exchange narrowing[56]. Site fluctuations become partially mitigated due to the coupling between the local

sites, resulting in exciton energy distributions with narrower energy widths than those of the constituent sites. The degree of exchange narrowing is proportional to the extent of exciton delocalization.

Since exchange narrowing is more effective at damping the site fluctuations in a 10-mer (DMDC) metal carbonyl complex than for a trimer (CMT), it is possible that the size of the exciton space is actually responsible for the apparent differences in spectral

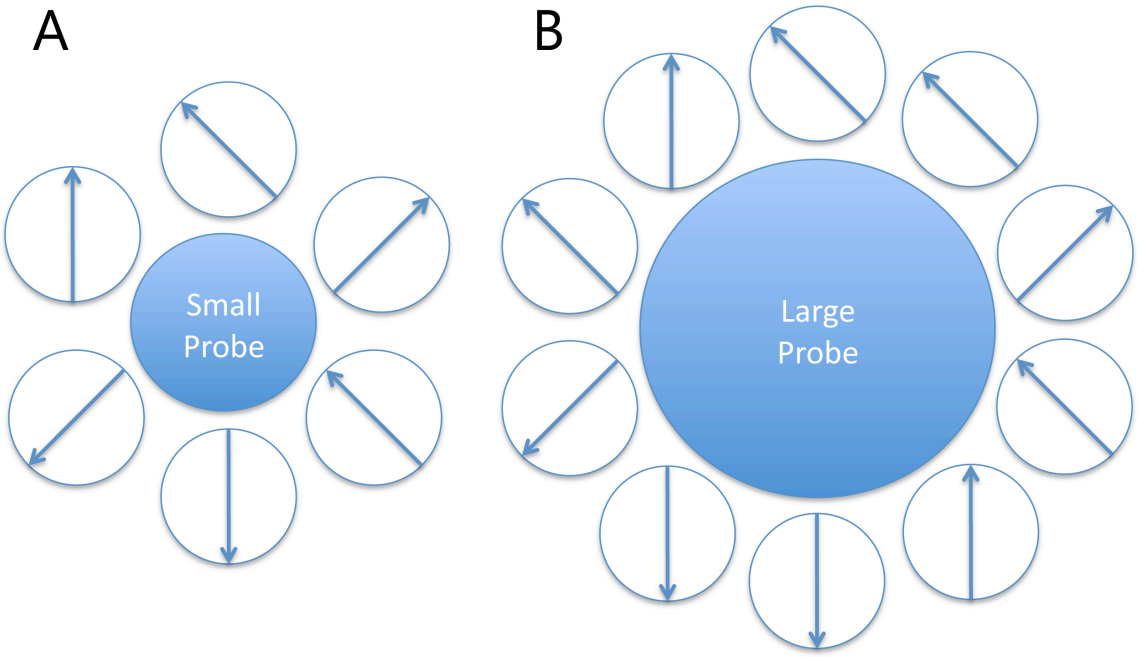

Figure 5.14 A probe with a small IR active surface area (A) has fewer dipoles participating in the microenvironment than does a probe with a larger IR active surface area (B).

diffusion time scales. While it is certainly intriguing to imagine another geometrical contribution to spectral diffusion dynamics beyond the surface area picture we explore in this manuscript, the fact that we find different overall spectral diffusion time scales for cdCMT and free CMT suggests that the topology of the exciton states is not responsible for the dynamical differences. Both are trimers, so one would expect the same degree of exchange narrowing. Indeed, the FT-IR spectra of the carbonyl bands are indistinguishable, but the spectral diffusion of cdCMT is faster than that of CMT, which seems to be consistent with the difference in the solvent accessible surface areas. Delocalization is typically quantified by the participation ratio, which equals the number of sites involved in a given eigenstate[57]. Since exciton delocalization varies according to the specific eigenstate, in future studies it may be possible to compare spectral diffusion in complexes with different SASA values but with similar exciton

delocalization in order to isolate the influence of exchange narrowing on spectral diffusion dynamics.

5.3.3 Simulations. Our experimental results suggest spectral diffusion is dependent on SASA, where the SASA is a measure of the number solvent molecules participating in the probe's microenvironment (**Fig. 5.14**), and we implement novel simulations to test this correlation. Typically, spectral diffusion models rely on mapping vibrational frequencies to electrostatic interactions in conjunction with classical molecular dynamics (MD) simulations to propagate trajectories. To generate this map, the electrostatic interaction and vibrational frequency, calculated using standard *ab initio* methods, are calculated for multiple conformational snap shots extracted from MD simulations. A correlation between electrostatic interaction and vibrational frequency is then determined using regression analysis. Depending on the spectroscopically relevant species, mapping can range from simple electric field projections along the bond axis, to multisite evaluations of the electrostatic potential. Although this approach has proven successful in calculating spectral diffusion in various contexts, its effectiveness is dependent on the accuracy of the solvent parameters, reliability of the mapping, and the simulation methods.

Because reliable electrostatic interaction to vibrational frequency maps and MD parameters for DMDC and CMT are not available, we developed a new, albeit highly simplified, model to test the dependence of spectral diffusion on the SASA. To do this, we simulate the reorientation of the solvent molecular dipoles with a Gaussian Markov model. We reduce the complexity of solvation dynamics by simulating the solvent as

dipoles[58] on a two dimensional surface. The electrostatic interaction experienced by the probe due to the dipole is dependent on the relative orientation of the dipole and the probe's microenvironment, and therefore the probes instantaneous vibrational frequency, is created by the cumulative interactions of the surrounding dipoles. How the microenvironment will shift the instantaneous vibrational frequency is dependent on the nature of the probe, and can be broken into two extremes we denote arrangement *independent* (AI) and arrangement *dependent* (AD). An example of an AI treatment is where the probe's vibrational frequency is linearly mapped to the electric field along the stretch of interest; different configurations of solvent molecules may produce identical vibrational frequencies as long as the electric field along the spectroscopically active bond remains the same. When such an approach is adopted, it is often denoted "Stark spectroscopy." In the second approach, AD, each distinct arrangement of orientations is counted as a distinct solvation microstate, regardless of its projection onto the solute probe. This heterogeneous model necessarily produces a much larger number of distinct microenvironments.

An example of the importance of such arrangement *dependence* is found in methyl thiocyanate and acetonitrile[59, 60]. Cho *et al*. showed that there does not exist a linear relationship between the electric field parallel to the CN bond and its vibrational frequency ultimately determining that the vibrational frequency is sensitive to the non-uniform electrostatic interactions of the solvent. The authors suggest the complex electrostatic dependence may be due to the ability of the CN triple bond to form a both a s hydrogen bond and a p hydrogen bond. The successful map of the vibrational

frequency to an electrostatic interaction was based on calculating the electric potential at 17 sites around the CN functional group. These extra sites captured the unique, spatially heterogeneous arrangements of the solvent molecules. With the mapping proposed by Cho, symmetry still allows different configurations to produce identical vibrational frequencies, whereas in our simulations we adopt a limiting alternative where each arrangement of dipole orientation values constitutes a unique microenvironment. Models of real systems will necessarily lie somewhere between our AI and AD approaches. The chemical similarities between CN and CO and the multiple carbonyls of CMT and DMDC suggests that they would more closely resemble the AD approach. Indeed, our own attempts to reproduce linear absorption line shapes and spectral diffusion dynamics using a simple map for the CO site energies as inputs to our otherwise successful excitonic hamiltonian resulted in qualitatively poor agreement with experiment. A full description of the dipole simulation methods and microenvironment computation can be found in the methods section.

Here, we compare simulations with one to four dipoles for both the AD and AI microenvironment sensitivity. The maximum number of dipoles is limited by the computational time required for the AD simulations, but because we only attempt to determine the relationship between the number of solvent dipoles and spectral diffusion, four data points are sufficient to demonstrate this trend.

When the microenvironment is arrangement *independent* (AI), additional dipoles speed up the spectral diffusion (**Fig. 5.15a**). An increase in the number of dipoles narrows the probability distribution of the microenvironments requiring less time for a

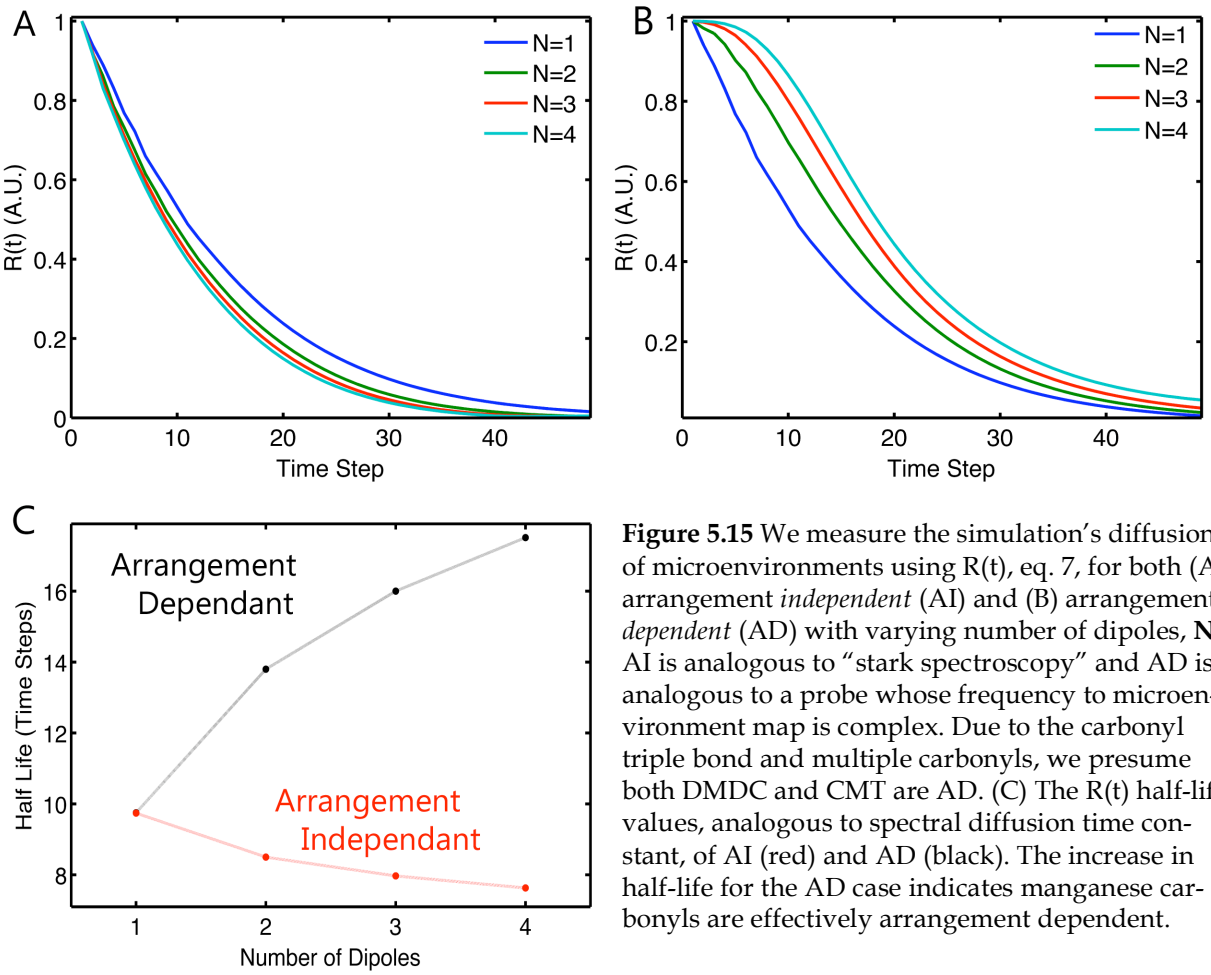

Figure 5.15 We measure the simulation's diffusion of microenvironments using R(t), eq. 7, for both (A) arrangement *independent* (AI) and (B) arrangement *dependent* (AD) with varying number of dipoles, **N**. AI is analogous to "stark spectroscopy" and AD is analogous to a probe whose frequency to microenvironment map is complex. Due to the carbonyl triple bond and multiple carbonyls, we presume both DMDC and CMT are AD. (C) The R(t) half-life values, analogous to spectral diffusion time constant, of AI (red) and AD (black). The increase in half-life for the AD case indicates manganese carbonyls are effectively arrangement dependent.

probe to search the accessible configuration space. Conversely, when the microenvironment is arrangement *dependent* (AD), the additional dipoles slow the spectral diffusion (Fig 5.15b). As the number of dipoles increases, the number of available solvation environments grows exponentially requiring more time for the probe to search the possible microenvironments. This correlation between spectral diffusion and the number of participating dipoles matches the correlation between spectral diffusion and solvent accessible surface area in our experimental data (Table 5.2). Being AD suggests that the vibrational frequencies of these manganese carbonyls are dependent on more than a single additive electrostatic interaction.

To compare the diffusion of the AD and AI models directly, the half-life of each

simulation is plotted in Figure 5.15c. With only one dipole, there is no distinction between AD and AI. With increased dipole numbers, however, the half-life values for the AI microenvironments decrease monotonically. This behavior seems to be intuitive since increasing the number of dipoles to infinity, for example, would cause the probability distribution of available solvation environments to narrow to a delta function matching the original starting position; fluctuations away from the most probable microenvironment would be found only very rarely. This limit is analogous to the thermodynamic limit; when the number of particles approaches infinity, fluctuations away from the most probable microstate are nearly impossible. When defined as AD, however, the half-life values increase logarithmically, the difference in half-life between 1 and 2 dipoles is the same as between 2 and 4 dipoles.

5.3.4 A dynamical entropy probe. Since spectral diffusion is a consequence of dynamically sampling available configurations, one goal of our analysis is to establish a link between spectral diffusion and conformational entropy. At first glance, it might be tempting to use other observables available from 2DIR spectroscopy, such as the inhomogeneous spectral width, as a proxy for entropy. Unfortunately, however, spectral widths—both homogeneous and inhomogeneous—are often determined largely by solvent polarity, making it difficult to link such an observable to a measure of the configuration space. For example, it is quite common to find <3 cm^{-1} bandwidth infrared transitions for metal carbonyl complexes in nonpolar solvents, with no discernible inhomogeneous broadening. Surely this spectroscopic feature does not indicate an absence of configurational entropy. Rather, the lack of solvent polarity

renders the probe vibration blind to its local solvent environment. Often there do appear to be correlations between inhomogeneous broadening and spectral diffusion, but there are nevertheless clear examples of pronounced deviations. In our own work, for example, we have used mixtures of solvents to produce identical linear absorption line shapes, while observing spectral diffusion that tracks the viscosity of the solvent mixture[10]. More recently, we have found a striking example using the metal carbonyl probe $Re_2(CO)_{10}$ in the fragile glass former 1,2-hexanediol. In that case we measured FTIR and 2DIR spectra as a function of temperature, finding that although the FTIR spectra were completely temperature insensitive, the spectral diffusion was both non-exponential and its temperature dependence was non-Arrhenius[15]. Hence, essentially static quantities such as the inhomogeneous width can be both incomplete and even misleading.

In this work, the inhomogeneous widths of CMT and cdCMT show minimal differences yet the spectral diffusion time scales of cdCMT are faster than those of CMT. The similarities in the inhomogeneous line widths between CMT and cdCMT are due to the similarities in solvent polarity, while the differences in spectral diffusion of $Mn_2(CO)_{10}$, CMT, and cdCMT arise from changes in the size of conformational space available to the probe. Here, we find that the conformational space available to $Mn_2(CO)_{10}$, CMT, and cdCMT is dependent on the number of solvent molecules that participate in creating the probe's microenvironment, which can be estimated by computing the solvent accessible surface area of the probe's carbonyl ligands.

5.4 Conclusion

Using a piano-stool metal carbonyl complex to probe dynamics both alone in solution and partially nanoconfined in a cyclodextrin host, we have examined solvent dependent spectral dynamics using ultrafast 2DIR spectroscopy. Combined with our previous results for DMDC in the same linear alcohol series, we observe a remarkable trend where spectral diffusion time constants correlate linearly with viscosity, extrapolating to finite zero-viscosity intercepts. That the slopes of the correlations are essentially equal within our ability to fit the data, we conclude that the solvent dynamics are roughly indistinguishable between probes. The differences in intercepts, however, arise due to variation in the size of the solvation environment's configuration space, which we link to the solvent-accessible surface areas of the three probe solutes. To model the effect due solely to solvent access, we implemented a Markov chain simulation of spectral diffusion. This model allows us to estimate the time required to sample the solvent configuration space independently of any actual dynamical considerations. Experimentally such a separation is not possible using a solvent series because one finds inevitable correlations between a solvent's molecular volume and its viscosity. Instead, we compare the results of the simulation with the probe molecule's solvent accessible surface area, which can be varied while still presenting a similar chemical interface with the solvent. Our simple model shows that there are two ingredients that are essential in order to reproduce our experimental trend. Besides the rather obvious requirement for correlations among the dipole orientations, we also find that we must enumerate the solvation environments in such a way that we retain the full spatial

arrangement of dipoles, regardless of the resulting projection of their sum. This effect has been observed previously in the computational treatment of vibrational frequencies of, for example, alyklnitriles in solution, where the spatial arrangement of solvent molecules is required to accurately reproduce the observed linear spectrum. It is not surprising that a similarly spatially heterogeneous solvation environment is needed in our case, since the carbonyl modes are inherently delocalized over two to three local CO sites. This work attempts to make more concrete the analogy between spectral and translational diffusion in order to motivate further efforts to use frequency correlation functions as reporters of conformational entropy. The ability to estimate site-specific conformational entropies will enable detailed probes of important chemical processes on surfaces and interfaces, within membranes, and in proteins.

Acknowledgements

This work was supported by the National Science Foundation (Grant No. CHE-0748501) and the Camille & Henry Dreyfus Foundation.

References

1. Anna, J. M.; Kubarych, K. J., "Watching solvent friction impede ultrafast barrier crossings: A direct test of Kramers theory". *Journal of Chemical Physics* **2010,** *133* (174506).

2. Baiz, C. R.; McCanne, R.; Kubarych, K. J., "Structurally Selective Geminate Rebinding Dynamics of Solvent-Caged Radicals Studied with Nonequilibrium Infrared Echo Spectroscopy". *Journal of the American Chemical Society* **2009,** *131* (38), 13590.

3. Khalil, M.; Demirdoven, N.; Tokmakoff, A., "Coherent 2D IR spectroscopy: Molecular structure and dynamics in solution". *Journal of Physical Chemistry A* **2003,** *107* (27), 5258-5279.

4. Khalil, M.; Demirdoven, N.; Tokmakoff, A., "Vibrational coherence transfer characterized with Fourier-transform 2D IR spectroscopy". *Journal of Chemical Physics* **2004,** *121* (1), 362-373.

5. Tokmakoff, A.; Sauter, B.; Fayer, M. D., "TEMPERATURE-DEPENDENT VIBRATIONAL-RELAXATION IN POLYATOMIC LIQUIDS - PICOSECOND INFRARED PUMP-PROBE EXPERIMENTS". *Journal of Chemical Physics* **1994,** *100* (12), 9035-9043.

6. King, J. T.; Ross, M. R.; Kubarych, K. J., "Water-Assisted Vibrational Relaxation of a Metal Carbonyl Complex Studied with Ultrafast 2D-IR". *Journal of Physical Chemistry B* **2012,** *116* (12), 3754-3759.

7. Demirdoven, N.; Khalil, M.; Golonzka, O.; Tokmakoff, A., "Correlation effects in the two-dimensional vibrational spectroscopy of coupled vibrations". *Journal of Physical Chemistry A* **2001,** *105* (34), 8025-8030.

8. Golonzka, O.; Khalil, M.; Demirdoven, N.; Tokmakoff, A., "Coupling and orientation between anharmonic vibrations characterized with two-dimensional infrared vibrational echo spectroscopy". *Journal of Chemical Physics* **2001,** *115* (23), 10814-10828.

9. King, J. T.; Anna, J. M.; Kubarych, K. J., "Solvent-hindered intramolecular vibrational redistribution". *Physical Chemistry Chemical Physics* **2011,** *13* (13), 5579-5583.

10. King, J. T.; Baiz, C. R.; Kubarych, K. J., "Solvent-Dependent Spectral Diffusion in a Hydrogen Bonded "Vibrational Aggregate"". *Journal of Physical Chemistry A* **2010,** *114* (39), 10590-10604.

11. Cahoon, J. F.; Sawyer, K. R.; Schlegel, J. P.; Harris, C. B., "Determining transition-state geometries in liquids using 2D-IR". *Science* **2008,** *319* (5871).

12. Anna, J. M.; Ross, M. R.; Kubarych, K. J., "Dissecting Enthalpic and Entropic Barriers to Ultrafast Equilibrium Isomerization of a Flexible Molecule Using 2DIR Chemical Exchange Spectroscopy". *Journal of Physical Chemistry A* **2009,** *113* (24), 6544-6547.

13. Anna, J. M.; King, J. T.; Kubarych, K. J., "Multiple Structures and Dynamics of CpRu(CO)(2) (2) and CpFe(CO)(2) (2) in Solution Revealed with Two-Dimensional Infrared Spectroscopy". *Inorganic Chemistry* **2011,** *50* (19), 9273-9283.

14. Stewart, A. I.; Clark, I. P.; Towrie, M.; Ibrahim, S. K.; Parker, A. W.; Pickett, C. J.; Hunt, N. T., "Structure and vibrational dynamics of model compounds of the FeFe -hydrogenase enzyme system via ultrafast two-dimensional infrared spectroscopy". *Journal of Physical Chemistry B* **2008,** *112* (32), 10023-10032.

15. King, J. T.; Ross, M. R.; Kubarych, K. J., "Ultrafast alpha-Like Relaxation of a Fragile Glass-Forming Liquid Measured Using Two-Dimensional Infrared Spectroscopy". *Physical Review Letters* **2012,** *108* (15).

16. Stratt, R. M.; Maroncelli, M., "Nonreactive dynamics in solution: The emerging molecular view of solvation dynamics and vibrational relaxation". *Journal of Physical Chemistry* **1996,** *100* (31).

17. Full, J.; Daniel, C.; Gonzalez, L., "Ultrafast non-adiabatic laser-induced photodissociation dynamics of CpMn(CO)(3). An ab initio quantum chemical and dynamical study". *Physical Chemistry Chemical Physics* **2003,** *5* (1), 87-96.

18. Picciochi, R.; Canongia Lopes, J. N.; Diogo, H. P.; Minas da Piedade, M. E., "Experimental and Molecular Dynamics Simulation Study of the Sublimation Energetics of Cyclopentadienyltricarbonylmanganese (Cymantrene)". *Journal of Physical Chemistry A* **2008,** *112* (41), 10429-10434.

19. Forrow, N. J.; Walters, S. J., "Transition metal half-sandwich complexes as redox mediators to glucose oxidase". *Biosensors & Bioelectronics* **2004,** *19* (7), 763-770.

20. Borissova, A. O.; Antipin, M. Y.; Lyssenko, K. A., "Mutual Influence of Cyclopentadienyl and Carbonyl Ligands in Cymantrene: QTAIM Study". *Journal of Physical Chemistry A* **2009,** *113* (40), 10845-10851.

21. Biehl, E. R.; Reeves, P. C., "CONVENIENT, HIGH-YIELD SYNTHESIS OF CARBOXYLIC-ACID DERIVATIVES OF FERROCENE AND CYCLOPENTADIENYLMANGANESE TRICARBONYL". *Synthesis-Stuttgart* **1973,** (6), 360-361.

22. Oudijk, G., "The Rise and Fall of Organometallic Additives in Automotive Gasoline". *Environ. Forensics* **2010,** *11* (1-2), 17-49.

23. Splith, K.; Neundorf, I.; Hu, W.; N'Dongo, H. W. P.; Vasylyeva, V.; Merz, K.; Schatzschneider, U., "Influence of the metal complex-to-peptide linker on the synthesis and properties of bioactive CpMn(CO)(3) peptide conjugates". *Dalton Transactions* **2010,** *39* (10), 2536-2545.

24. Remy, I.; Brossier, P., "ATOMIC-ABSORPTION SPECTROMETRIC DETECTION OF BIOTIN-CYMANTRENE AS A METALLO-TRACER FOR THE AVIDIN-BIOTIN SYSTEM". *Analyst* **1993,** *118* (8), 1021-1025.

25. Remy, I.; Brossier, P.; Lavastre, I.; Besancon, J.; Moise, C., "POTENTIALITY OF AN ORGANOMETALLIC LABELED STREPTAVIDIN BIOTIN SYSTEM IN METALLOIMMUNOASSAY". *Journal of Pharmacological Biomedical Analysis* **1991,** *9* (10-12), 965-967.

26. Song, L. X.; Meng, Q. J.; You, X. Z., "STUDY ON THE INCLUSION COMPOUND OF BETA-CYCLODEXTRIN WITH (ETA(5) CYCLOPENTADIENYL) TRICARBONYLMANGANESE". *Chinese Journal of Chemistry* **1995,** *13* (4), 311-317.

27. Song, L. X.; Meng, Q. J.; You, X. Z., "PREPARATION AND PROPERTIES OF INCLUSION COMPOUND OF CYCLOPENTADIENYLMANGANESE TRICARBONYL COMPLEX WITH A BETA-CYCLODEXTRIN DIMER". *Journal of Organometallic Chemistry* **1995,** *498* (1), C1-C5.

28. Lu, C. S.; Zhang, W. W.; Ren, X. M.; Hu, C. J.; Zhu, H. Z.; Meng, Q. J., "Intramolecular photo-substitution in the inclusion compound of mono 6-deoxy-6-(2-butenedinitrile-2,3-dimercapto sodium salt) -beta-cyclodextrin with cyclopentadienyl manganese tricarbonyl in DMF solution". *Journal of the Chemical Society-Dalton Transactions* **2001,** (20), 3052-3055.

29. Supplemental Information.

30. Anna, J. M.; Nee, M. J.; Baiz, C. R.; McCanne, R.; Kubarych, K. J., "Measuring absorptive two-dimensional infrared spectra using chirped-pulse upconversion detection". *Journal of the Optical Society of America B-Opt. Phys.* **2010,** *27* (3), 382-393.

31. Nee, M. J.; McCanne, R.; Kubarych, K. J.; Joffre, M., "Two-dimensional infrared spectroscopy detected by chirped pulse upconversion". *Optics Letters* **2007,** *32* (6), 713-715.

32. Ogilvie, J. P.; Kubarych, K. J., Multidimensional Electronic and Vibrational Spectroscopy: An Ultrafast Probe of Molecular Relaxation and Reaction Dynamics. In *Advances in Atomic, Molecular, and Optical Physics, Vol 57*, Arimondo, E.; Berman, P. R.; Lin, C. C., Eds. Elsevier Academic Press Inc: San Diego, 2009; Vol. 57, pp 249-321.

33. Hamm, P. a. Z., Martin, *Concepts and Methods of 2D Infrared Spectroscopy*. Cambridge University Press: 2011; p 286.

34. Roberts, S. T.; Loparo, J. J.; Tokmakoff, A., "Characterization of spectral diffusion from two-dimensional line shapes". *Journal of Chemical Physics* **2006,** *125* (8), 084502.

35. Kwak, K.; Park, S.; Finkelstein, I. J.; Fayer, M. D., "Frequency-frequency correlation functions and apodization in two-dimensional infrared vibrational echo spectroscopy: A new approach". *Journal of Chemical Physics* **2007,** *127* (12), 124503.

36. Kwak, K.; Rosenfeld, D. E.; Fayer, M. D., "Taking apart the two-dimensional infrared vibrational echo spectra: More information and elimination of distortions". *Journal of Chemical Physics* **2008,** *128* (20), 204505.

37. Brooks, B. R.; Brooks, C. L., III; Mackerell, A. D., Jr.; Nilsson, L.; Petrella, R. J.; Roux, B.; Won, Y.; Archontis, G.; Bartels, C.; Boresch, S.; Caflisch, A.; Caves, L.; Cui, Q.; Dinner, A. R.; Feig, M.; Fischer, S.; Gao, J.; Hodoscek, M.; Im, W.; Kuczera, K.; Lazaridis, T.; Ma, J.; Ovchinnikov, V.; Paci, E.; Pastor, R. W.; Post, C. B.; Pu, J. Z.; Schaefer, M.; Tidor, B.; Venable, R. M.; Woodcock, H. L.; Wu, X.; Yang, W.; York, D. M.; Karplus, M., "CHARMM: The Biomolecular Simulation Program". *Journal of Computational Chemistry* **2009,** *30* (10), 1545-1614.

38. MacKerell, A. D.; Bashford, D.; Bellott, M.; Dunbrack, R. L.; Evanseck, J. D.; Field, M. J.; Fischer, S.; Gao, J.; Guo, H.; Ha, S.; Joseph-McCarthy, D.; Kuchnir, L.; Kuczera, K.; Lau, F. T. K.; Mattos, C.; Michnick, S.; Ngo, T.; Nguyen, D. T.; Prodhom, B.; Reiher, W. E.; Roux, B.; Schlenkrich, M.; Smith, J. C.; Stote, R.; Straub, J.; Watanabe, M.; Wiorkiewicz-Kuczera, J.; Yin, D.; Karplus, M., "All-atom empirical potential for molecular modeling and dynamics studies of proteins". *Journal of Physical Chemistry B* **1998,** *102* (18), 3586-3616.

39. Yesselman, J. D.; Price, D. J.; Knight, J. L.; Brooks, C. L., III, "MATCH: An Atom-Typing Toolset for Molecular Mechanics Force Fields". *Journal of Computational Chemistry* **2012,** *33* (2), 189-202.

40. Humphrey, W.; Dalke, A.; Schulten, K., "VMD: Visual molecular dynamics". *Journal of Molecular Graphics & Modelling* **1996,** *14* (1), 33-38.

41. Nguyen, C. N.; Stratt, R. M., "Preferential solvation dynamics in liquids: How geodesic pathways through the potential energy landscape reveal mechanistic details about solute relaxation in liquids". *Journal of Chemical Physics* **2010,** *124503* (12).

42. Bencze, E.; Mink, J.; Nemeth, C.; Herrmann, W. A.; Lokshin, B. V.; Kuhn, F. E., "Vibrational spectroscopic and force field studies of (eta(5)-Cp)ML3-type complexes (M = Mn, Re; L = CO, O)". *Journal of Organometallic Chemistry* **2002,** *642* (1-2), 246-258.

43. Parker, D. J., "VIBRATIONAL-SPECTRA OF TRICARBONYL(PI-CYCLOPENTADIENYL)MANGANESE, BIS- TRICARBONYL(PI-CYCLOPENTADIENYL)MOLYBDENUM , AND THEIR DEUTERIATED DERIVATIVES". *Journal of the Chemical Society-Dalton Transactions* **1974,** (2), 155-162.

44. Aree, T.; Chaichit, N., "Crystal form III of beta-cyclodextrin-ethanol inclusion complex: layer-type structure with dimeric motif". *Carbohydrate Research* **2008,** *343* (13), 2285-2291.

45. Su, S. G.; Simon, J. D., "IMPORTANCE OF MOLECULAR-SIZE ON THE DYNAMICS OF SOLVENT RELAXATION". *Journal of Physical Chemistry* **1989,** *93* (2), 753-758.

46. Chapman, C. F.; Fee, R. S.; Maroncelli, M., "MEASUREMENTS OF THE SOLUTE DEPENDENCE OF SOLVATION DYNAMICS IN 1-PROPANOL - THE ROLE OF SPECIFIC HYDROGEN-BONDING INTERACTIONS". *Journal of Physical Chemistry* **1995,** *99* (13), 4811-4819.

47. Alavi, D. S.; Hartman, R. S.; Waldeck, D. H., "A TEST OF CONTINUUM MODELS FOR DIELECTRIC FRICTION - ROTATIONAL DIFFUSION OF PHENOXAZINE DYES IN DIMETHYLSULFOXIDE". *Journal of Chemical Physics* **1991,** *94* (6), 4509-4520.

48. Dote, J.; Kivelson, D.; Schwartz, R. N., "A MOLECULAR QUASI-HYDRODYNAMIC FREE-SPACE MODEL FOR MOLECULAR ROTATIONAL RELAXATION IN LIQUIDS". *Journal of Physical Chemistry* **1981,** *85* (15), 2169-2180.

49. Kurnikova, M. G.; Balabai, N.; Waldeck, D. H.; Coalson, R. D., "Rotational relaxation in polar solvents. Molecular dynamics study of solute-solvent interaction". *Journal of the American Chemical Society* **1998,** *120* (24), 6121-6130.

50. Spears, K. G.; Steinmetz, K. M., "SOLVENT INTERACTIONS WITH ANIONS BY REORIENTATION STUDIES OF RESORUFIN". *Journal of Physical Chemistry* **1985,** *89* (17), 3623-3629.

51. Williams, A. M.; Jiang, Y.; Benamotz, D., "MOLECULAR-REORIENTATION DYNAMICS AND MICROSCOPIC FRICTION IN LIQUIDS". *Journal of Chemical Physics* **1994,** *180* (2-3), 119-129.

52. Zhao, Y. H.; Abraham, M. H.; Zissimos, A. M., "Fast calculation of van der Waals volume as a sum of atomic and bond contributions and its application to drug compounds". *Journal of Organic Chemistry* **2003,** *68* (19), 7368-7373.

53. Ludwig, R.; Gill, D. S.; Zeidler, M. D., "MOLECULAR-REORIENTATION IN LIQUID METHANOL". *Zeitschrift Fur Naturforschung Section a-a Journal of Physical Sciences* **1991,** *46* (1-2), 89-94.

54. Ludwig, R.; Rusbuldt, C.; Bopp, P. A.; Zeidler, M. D., "THE ANISOTROPY OF THE MOLECULAR REORIENTATIONAL MOTIONS IN LIQUID

METHANOL". *Zeitschrift Fur Naturforschung Section a-a Journal of Physical Sciences* **1995,** *50* (2-3), 211-216.

55. Ludwig, R.; Zeidler, M. D., "MOLECULAR-DYNAMICS IN LOWER ALCOHOLS". *Zeitschrift Fur Physikalische Chemie-International Journal of Research in Physical Chemistry & Chemical Physics* **1995,** *189*, 19-27.

56. Knapp, E. W., *Journal of Chemical Physics* **1984,** *85*, 73-82.

57. L. D. Bakalis, J. K., *Journal of Chemical Physics* **1999,** *103*, 6620-6628.

58. Stratt, R. M., "THE STATISTICAL-MECHANICS OF A LIQUID OF 2-STATE MOLECULES". *Journal of Chemical Physics* **1984,** *80* (11).

59. Choi, J. H.; Oh, K. I.; Lee, H.; Lee, C.; Cho, M., "Nitrile and thiocyanate IR probes: Quantum chemistry calculation studies and multivariate least-square fitting analysis". *Journal of Chemical Physics* **2008,** *128* (13), 8.

60. Oh, K. I.; Choi, J. H.; Lee, J. H.; Han, J. B.; Lee, H.; Cho, M., "Nitrile and thiocyanate IR probes: Molecular dynamics simulation studies". *Journal of Chemical Physics* **2008,** *128* (15), 10.

Chapter Six

The Rigid Rotor Solvent Dependence of (Benzyl) Chromium Tricarbonyl

The work of this chapter was performed jointly with Ian Nilsen

6.1 Introduction

Synthetic molecular rotors have been studied due to the wide variety of their applications in areas such as nano-engineering[1, 2]. Recent advances such as monitoring microviscosity in living cells[3, 4], which has been implicated in disease, as well as unidirectional motion[5], have been achieved with synthetic molecular rotors. One study using ultrafast fluorescence suggests that optical control of the excited state can be used to modulate unidirectional torsional motion of light-activated molecular rotors[6]. Such studies have provided a firm foundation for how to drive a rotor in one direction, but little has been studied about the additional important interaction between the rotor and the bath. At equilibrium, the laws of thermodynamics dictate that unidirectional motion cannot be achieved[7]. However, equilibrium conditions provide the interesting

opportunity to watch rotors with low barriers rotate with energy entirely derived from the environment. In order to build a highly efficient synthetic molecular rotor operating near fundamental limits, it is important to understand the dynamical properties of the simplest possible rotors at the molecular scale. Viewed another way, it is essential to consider the dynamics of the passive elements of nanoscale machinery, since they are most likely to deviate from the behavior of familiar ballistic macroscopic devices.

Piano-stool complexes are model systems for studying molecular rotors due to their small size, simplicity, and ability to undergo rotation about an arene-metal bond[8-10]. Early NMR studies of (benzyl) chromium tricarbonyl ($C_6H_6Cr(CO)_3$, BCT) and its analogues investigated the effect of bulky side chains intended to slow motion along the reaction coordinate. Debates regarding the nature of restricted rotation about the arene-chromium bond initiated the study of torsional motion in BCT[11-13]. A later study combining high-field NMR for dynamics with x-ray crystallography for structure settled the debate by finding "unequivocal proof" of a slowed torsional reaction coordinate[14]. The study found that bulky side chains could slow the tripodal rotation, but did not investigate unsubstituted BCT since the rotation takes place faster than the NMR time scale. Experimental studies of BCT and the debate regarding the rotation about the arene-metal bond and structure of the molecule have been reviewed[15].

As computing power has continued to increase, studies have shifted to trying to define the reaction coordinate of BCT and its analogues using quantum chemistry. Multiple density functional theory studies have been conducted on BCT to determine the structure of the molecule using a variety of methods[16-18]. One study found that DFT

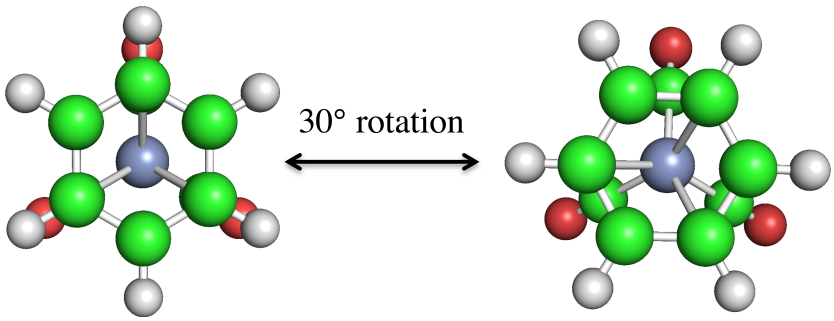

Figure 6.1. The BCT internal reaction coordinate is defined by the benzene rotation with respect to the tricarbonyl.

optimized the structure of BCT better than Møller–Plesset second-order calculations (MP2) by comparing the bond lengths and angles to microwave data[17]. A later study of BCT using DFT calculations with higher level basis sets optimized the two stable isomers and found they were separated by a barrier roughly half of k_BT[18]. The study did not create a potential surface for the torsional coordinate or investigate solvent interactions on the torsional frequencies, both of which are presented here.

In this paper, we study the reaction dynamics of BCT defined as the torsional motion of the benzene ring with respect to the tricarbonyl portion of the molecule (**Fig. 6.1**). We determine the potential energy surface using DFT and extract the carbonyl vibrational frequencies for the two stable conformations, staggered and eclipsed, along the reaction coordinate. The calculated barrier to isomerization is significantly less than k_BT, and suggests that interconversion between the two states happens on ultrafast timescales, on the order of picoseconds. Using a new variation of heterodyne detected photon echo spectroscopy, we are able to monitor the reaction dynamics of BCT using the frequency-frequency correlation function (FFCF), finding there to be no correlation between alkane chain length and reaction time. The structural interconversion between the two isomeric forms is primarily responsible for the decay in the FFCF, since apolar

solvents do not appreciably modulate the electric field of the isomerizing molecule. This knowledge is coupled with DFT calculations that show the symmetric stretch is broadened by only two bands, corresponding to the staggered and eclipsed isomers. Due to the extremely low barrier height of isomerization from eclipsed to staggered (~0.03kT), a three-state kinetic model can be applied to the system approximating the eclipsed isomer as a transition state. Using the classical Arrhenius equation we find that a significant fraction of the isomerizing molecules are in the eclipsed state; however, these molecules are rapidly interconverting so the time spent in the higher energy eclipsed state is significantly less than the staggered and as such can be approximated as a transition state. This approximation involves treating the isomerizing molecule as fluxional[19], isomerizing through the eclipsed state to equivalent staggered conformers. We find that in a series of alkane solvents ranging in viscosity from 0.3 to 3.8 cP, the reaction rate constant does not change, suggesting virtually frictionless motion of the molecular rotor.

6.2 Experimental and Computational Methods

Sample Preparation. Benzene chromium tricarbonyl (BCT) was purchased from Sigma-Aldrich and used as received. Sample cells consisted of a 100 μm Teflon spacer placed between two 3 mm thick calcium fluoride windows. The solutions were mixed thoroughly and filtered. If necessary, sonication was used to aid in solvation of the solid BCT. Samples were prepared at low concentrations, near 5 mM. Linear alkane and alcohol solvents were used as received, with no further purification.

Quantum Chemistry. The structure of BCT at various points along the torsional

coordinate was optimized using density functional theory (DFT). The calculations were performed in GAUSSIAN03[20] using the B3LYP functional for geometry optimizations and BP86 for frequency calculations with the 6-311+G(d,p) basis set for the carbon, oxygen and hydrogen atoms. The LANL2DZ basis set and pseudopotential was used for the chromium atom to account for the added electron density; this is consistent with modeling approaches for other metal carbonyl structures[21]. The choice of basis and functional is consistent with a past study for hexacarbonylchromium, which showed B3LYP and BP86 give similar results for geometry optimizations; however, BP86 tends to optimize vibrational frequencies closer to the experimental values[16]. The optimized structures not located at saddle points on the potential energy surface were calculated by constraining the dihedral angles between the carbonyls and the benzene ring while optimizing the geometry with respect to the other degrees of freedom. For optimized coordinates of the optimized energy minima, please consult the supporting information[22]. Frequency calculations were done on the stable isomers, but due to limitations in the computational method, frequency calculations of non-minima or saddle points for this molecule proved unreliable. Molecular volumes of the BCT stable states were also computed. To test the solvent dependence of the torsional coordinate frequency of BCT, calculations implementing a polarizable continuum model (PCM) were performed using built in solvent models of n-hexane, n-nonane, n-dodecane, and n-pentane. PCM calculations were performed using GAUSSIAN09[23].

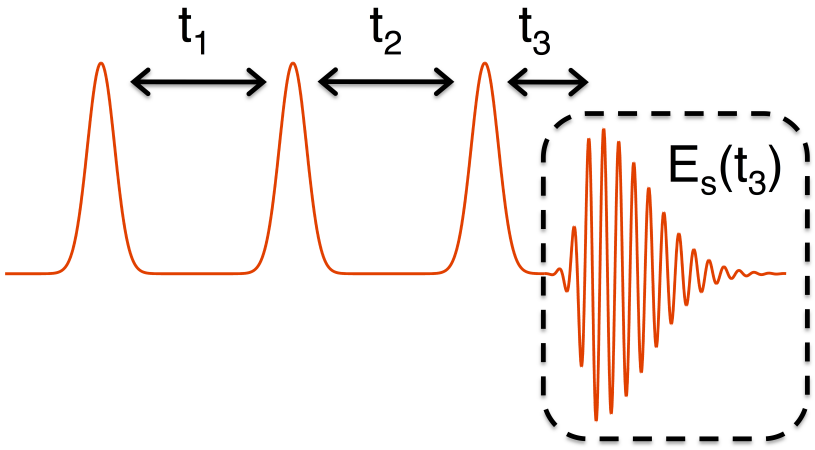

Figure 6.2. The time ordering of pulses for RASD; $E_s(t_3)$ is the signal measured by the CCD camera via heterodyne detection with an external local oscillator.

6.2.1 Data acquisition. When multiple conformations are available to a probe, each inducing fluctuations in the vibrational frequency, we observe a broadening in the linear FTIR spectrum; the temporal correlation of these vibrational frequency fluctuations is known as the frequency-frequency correlation function (FFCF). The FFCF is commonly represented as:

$$\langle \delta\omega(t)\delta\omega(0)\rangle = \frac{\delta(t)}{T_2} + \sum_i \Delta_i^2 exp\left(\frac{-t}{\tau_i}\right) \quad (1)$$

Where $\delta\omega(t)$ is the frequency fluctuations away from the mean, $\delta(t)$ is the delta function, T_2 is the pure-dephasing time, Δ_i is the amplitude of the frequency fluctuations, and τ_i is the spectral diffusion time constant. Due to the simplicity of our system, we represent the FFCF as a single exponential.

Typically chemical exchange can be monitored using 2D-IR spectroscopy measuring the cross peak volumes, but due to the relative proximity of the frequencies representing the two conformations, a 2.1 cm^{-1} splitting, a different approach is

required. In this experiment, we use the FFCF to observe the diagonal peaks: there are only two conformations broadening the symmetric band, thus any loss of correlation results from motion of the molecule.

Recently a new third order nonlinear method was proposed, t_1-resolved transient grating (TRTG), to measure the FFCF[24]. The TRTG method fixes the first coherence time, t_1 (see **Fig. 6.2** for time conventions), while scanning t_2, also known as the waiting time. The method proposed is homodyne detected where the rephasing and nonrephasing signals are measured simultaneously with photodiodes. Previous methods have proven adept at measuring the FFCF, such as three pulse photon echo peak shift and various analyses of two dimensional spectra[25-27], but require a relatively large acquisition times due to the necessity of scanning t_1 for each t_2 data point, twice in the case of background-free Fourier transform 2D spectroscopy. Although TRTG is related to the FFCF and requires a shorter data acquisition time, it does not ideally approximate the FFCF. Recently, we have developed a novel method similar to that of TRTG but that more faithfully monitors the FFCF[28].

The experimental setup and data acquisition for the methods have been presented elsewhere[29]. Briefly, the signal, $E_s(t_3)$, and a slightly delayed local oscillator are measured using a spectrometer equipped with a 1340x100 pixel CCD camera to detect the spectrum of $E_s(t_3)$ and the local oscillator after they are converted to the visible by chirped pulse upconversion. Single shot detection enables either t_1 or t_2 to be scanned continuously during data acquisition.

Previously, the ability to measure the FFCF from 2DIR spectra was studied

utilizing the inhomogeneous index[30]:

$$I.I. = \frac{A_r - A_n}{A_r + A_n} \tag{2}$$

Where A_r and A_n represent the rephasing and nonrephasing peak volumes, respectively, of the mode of interest. Here, we utilize the inhomogeneous index rather than the 2DIR peak volume, A_r and A_n represent the amplitudes of the t_1 resolved heterodyne detected signal. Under the short time approximation, the rapidly acquired spectral diffusion (RASD) is represented as:

$$RASD = \text{erf}\left(t_1 \bar{C}(t_2) \sqrt{\frac{\langle \delta\omega^2 \rangle}{2}}\right) \tag{3}$$

Where $\bar{C}$ is the normalized correlation function. It should be noted that the magnitude of t_1 acts as a scaling factor and is selected to maximize the signal to noise ratio.

6.2.1 Data processing. Both the rephasing and nonrephasing signals contain an oscillatory component that arises from the coherence between the asymmetric and symmetric stretch during t_2. In order to enhance the decay of the FFCF, we remove these oscillatory features using a band-stop filter. The acquired data is further processed using a moving average to account for random noise. Data was normalized in order to better show differences in spectral diffusion time.

6.3 Results and Discussion

Quantum Chemistry. From the optimized BCT structures, the potential energy surface was calculated producing a periodic potential function corresponding to the torsional

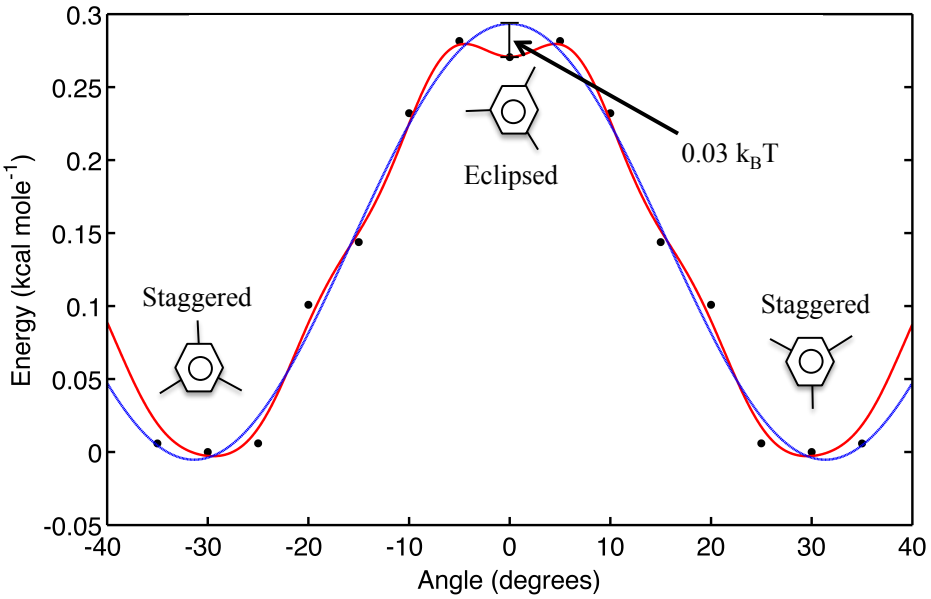

Figure 6.3. A periodic potential function (red) can be used to depict the internal rotation reaction coordinate of BCT. The two stable conformations of BCT are shown as cartoons. In blue, the approximation that the eclipsed conformer is a transition state.

reaction coordinate. The reaction coordinate is one-dimensional, with torsional motion around the metal-benzene bond representing the only variable. From x-ray crystallography[31], BCT was found to have the asymmetric C_{3v} point group due to the non-planar benzene ring. However, the asymmetry is small compared to the effect of the torsional motion so a C_{6v} point group can be used as a good approximation when creating a periodic potential function for BCT.

The surface is characterized by a double-well potential, with the staggered and eclipsed conformers as stable states (**Fig. 6.3** The global minimum staggered state is lower in energy than the eclipsed state by 0.28 kcal/mol, roughly half of k_BT, and is separated by a small reaction barrier roughly one thirtieth of k_BT, making it essentially diffusive relative to the eclipsed conformation. Due to the low barrier nature of the transition between staggered and eclipsed, the interconversion between species will

occur rapidly at room temperature.). For the purpose of kinetic studies used to calculated the reaction rate, the eclipsed state is treated as a transition state due to it having a barrier roughly thirty times smaller than the staggered to eclipsed reaction. Frequency calculations of the symmetric stretch of the staggered and eclipsed isomers revealed a 2.1 cm^{-1} red shift when moving from staggered (1977.4 cm^{-1}) to eclipsed (1979.5 cm^{-1}), which allows us to observe the staggered to eclipsed motion spectroscopically. Molecular volumes of the two states showed a difference of only 4%, 227.8 $Å^3$ and 218.6 $Å^3$ for the staggered and eclipsed isomers respectively. For both the staggered and eclipsed isomers, the frequency calculations yielded only positive frequencies. This implies that the two states are minima, since they have been optimized with respect to all degrees of freedom. Comparison with energy values along the reaction coordinate allows us to designate the staggered isomer as a global minimum and the eclipsed as a local minimum.

Utilizing a polarizable continuum model, frequency calculations performed on the global minimum were repeated with increasing length linear alkanes, selected from those used in the RASD experimental studies, to identify the torsional motion. For low frequency vibrations, our choice of basis and functional has been shown to need only a 1% correction factor[32], which is negligible compared to the vibrations themselves. The frequency of the torsional motion frequency in vacuum, 23.3 cm^{-1}, is slightly larger than that using continuum models for hexane, nonane, dodecane and pentadecane (22.6 cm^{-1}, 22.7 cm^{-1}, 22.8 cm^{-1}, 22.8 cm^{-1} respectively). The agreement of the torsional mode frequency using different polarizable continuum model solvents demonstrates how the

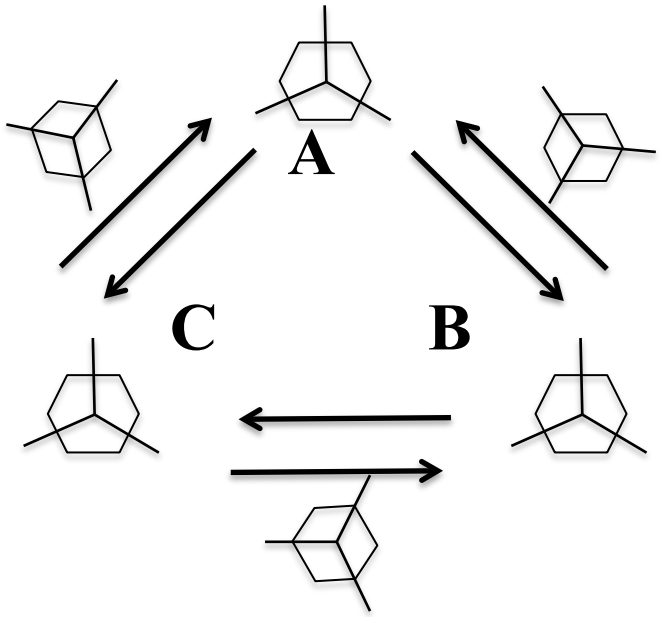

Figure 6.4. Interconversion between staggered states occurs via the eclipsed transition state, which due to the low barriers of both reactions is significantly populated at room temperature. The reaction can be simplified as a three-state kinetics problem due to the periodic nature of the potential.

potential surface for the linear alkanes of interest is independent of solvent.

6.3.1 Kinetics. The torsional motion of BCT can be accurately approximated as a three-state kinetics problem, due to the periodic nature of the potential where the staggered conformer interconverts to another staggered conformer in a similar manner to the "fluxionality" described by Harris[19]. In that work, $Fe(CO)_5$ was found to exchange vibrational energy between different modes of reacting ligands with a $\Delta\omega$ = 22.8 $cm^{-1}$and was measured by interpreting the growth of cross peak intensities over time. The use of cross peaks was appropriate in this case as the modes of interest were sufficiently separated in frequency to be able to discern them. However, in the case of BCT, there is a much smaller $\Delta\omega$ = 2.1 cm^{-1}. The close frequency proximity is typically thought of as spectral diffusion, however in this case it is clear that there are two distinct species typical of a chemical exchange experiment. A further distinction can be made as the

frequency modulation observed in BCT stems from conversion from the staggered to eclipsed state; thus the reaction is not really fluxional, but due to the low barrier of the eclipsed transition state it can be considered as such. Taking staggered state A to be the reference starting point, it can rotate in two directions: to either staggered state B or staggered state C in each case through an eclipsed transition state. Conversely, both B and C contribute to A (**Fig. 6.4**). Due to the high symmetry of the potential, the rate of moving in either direction to any state from A is of magnitude k, with sign determined by motion toward or away from state A. Rate equations can thus be written in matrix form as:

$$\begin{bmatrix} \dot{A} \\ \dot{B} \\ \dot{C} \end{bmatrix} = \begin{bmatrix} A \\ B \\ C \end{bmatrix} \begin{bmatrix} -2k & k & k \\ k & -2k & k \\ k & k & -2k \end{bmatrix} \quad (4)$$

Solving the system yields the following general solution:

$$A(t) = B(t) = C(t) = N * \exp(-3kt) \quad (5)$$

due to the symmetry of the system. The prefactor N is determined from initial conditions. The rate constant in the exponential is modified by a factor of three. This means that the rate constant effectively measured by an experimental setup will be three times larger than for a single staggered to staggered transition, or in other words, the time constant measured for the reaction will be a factor of three shorter compared to the actual rate. Because the time constant is the inverse of the rate, the time constant of the measured spectral diffusion will be a third of the reactions time constant.

6.3.2 FT-IR and spectral diffusion data. The Fourier transform infrared (FTIR) spectra of the BCT carbonyl stretches shows two distinct bands (**Fig. 6.5**), the degenerate

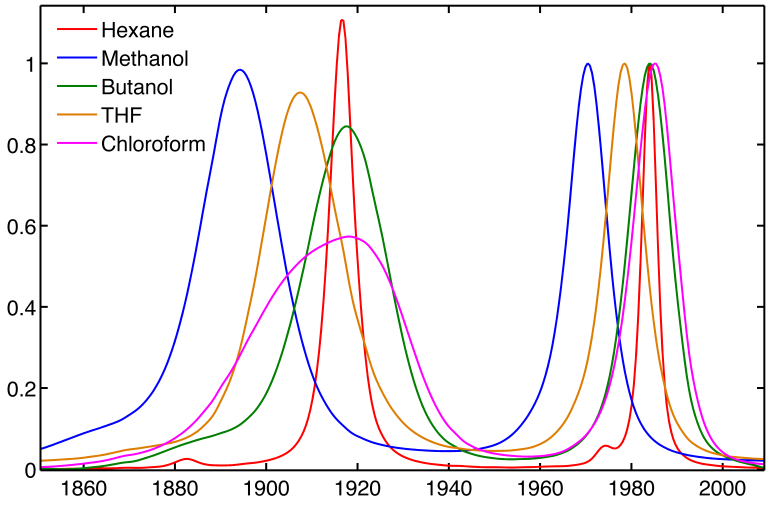

Figure 6.5 Fourier-transform IR spectra of BCT in various solvents showing the lower frequency asymmetric band and a higher frequency symmetric band.

asymmetric lower frequency band and the symmetric band. From the DFT calculations, we found the symmetric band in the staggered and eclipsed conformation to have two distinct frequencies separated by 2.1 cm^{-1} that effectively broaden the symmetric stretch's measured FTIR spectrum. No change was observed in the FWHM of BCT when comparing hexane to pentadecane, suggesting, at least for the alkane series, that the staggered and eclipsed conformations are sampled at similar rates since no motional narrowing is observed. However, in previous work, we have also observed negligible changes in the FTIR spectra of $Co_2(CO)_8$, a flexible molecule that exhibits a solvent viscosity dependence consistent with Kramers theory[33]. The characteristic red shift observed in many experiments as a result of increasing polarity is seen due to the greater Van der Waals forces of longer chain alkanes. The same polarity trend is observed in the alcohol series, as the more polar methanol induces the greatest red shift. The broadening of the symmetric stretch by two states is illustrated by fitting the symmetric stretch in squalane, a highly viscous solvent where molecules cannot

isomerize on timescales sensed by the experiment, with the symmetric stretch of hexane. Because BCT can rapidly isomerize in hexane, the symmetric stretch can be used to approximate one state and fit the squalane data. Varying the fitting parameters, we find that when fixing the distance between the two states 2.1 cm^{-1} apart as in the DFT calculations, the fit is better than allowing the parameters to vary[22].

Alcohols have a more complicated dielectric environment than alkanes allowing the solvent to create multiple microenvironments where each creates a unique spectral shift. The FFCF of BCT in alcohol would be a convolution of the torsional motion and the solvation structure and dynamics; here we seek to characterize only the torsional motion of BCT and therefore restrict our attention to alkanes in the nonlinear experiments. This approach to measuring the frequency fluctuations from the torsional

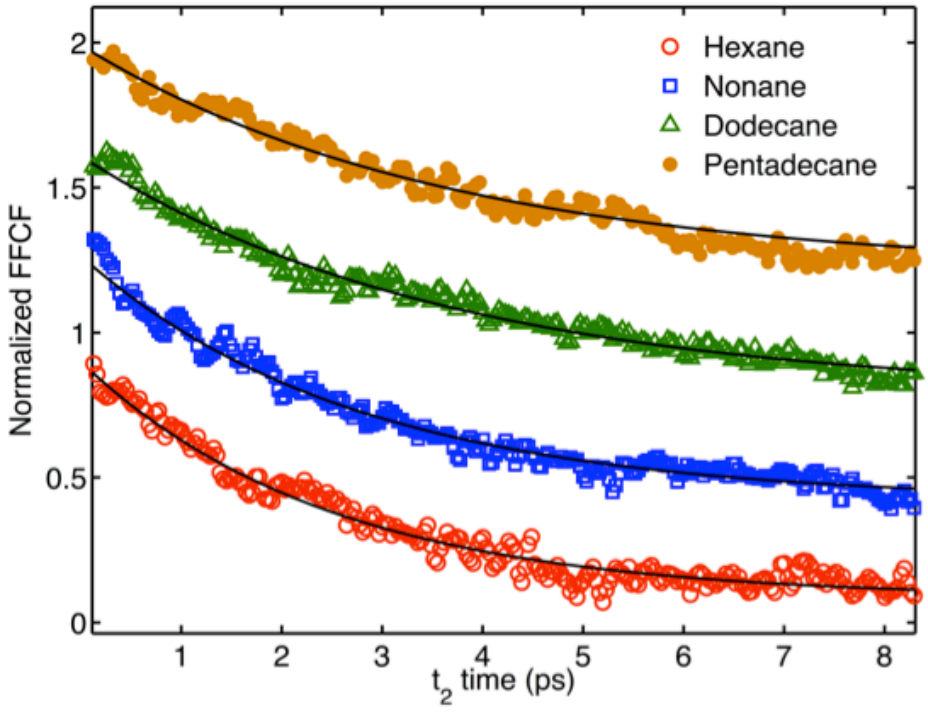

Figure 6.6 The normalized FFCF for each solvent is shown, offset by 0.4 and showing every fourth point for clarity. BCT spectral diffusion is independent of solvent viscosity among our tested set of alkanes.

motion is validated by the DFT calculations, which showed only two bands broadening the symmetric stretch even when running a solvent model for various alkanes.

The FFCF gives information about the reaction dynamics of BCT, as the symmetric band of interest is broadened by sampling the frequencies corresponding to the staggered and eclipsed isomers. By looking at a specific vibration and observing the timescale of frequency memory, we effectively can track the torsional reaction dynamics. Thus, any spectral diffusion observed can be directly linked to torsional motion along the reaction coordinate. We assume that the fluctuations in frequencies correspond to the isomerization, which is supported by the shift in frequency of the symmetric stretch in the DFT calculations. Since the new RASD method allows for data acquisition that is an order of magnitude faster than traditional 2DIR methods, it is possible to obtain more data points and minimize noise through data processing techniques. This capability is especially important for BCT, where the spectral diffusion timescale is on the order of a picosecond. Using traditional 2DIR spectroscopy, it is challenging to accurately determine the spectral diffusion timescale of BCT in the solvent series without adding significant spread to the FFCF decays. The FFCF plots appear to have identical decays across the full range of linear alkanes tested (**Fig 6.6**). The spectral diffusion timescale, found by fitting the decay to a single exponential and extracting the time constant, is roughly 3 ps for all solvents within the fitting error (see Supporting Information for data processing and fitting details) indicating that the time constant of the reaction is 9 ps.

The independence of spectral diffusion to alkane length defies the expected

trend seen in previous work where increases in viscosity correspond to increases in the spectral diffusion time[33,34], or to increases in equilibrium reaction rate constants[21]. A viscosity dependent model suggests that the timescale of interconversion between isomers can be altered by solvent interactions; a more viscous solvent should induce recrossings of the dividing surface, ultimately leading to longer spectral diffusion times. Our data disagrees with this expectation; moving from hexane (0.3 cP) to pentadecane (3.8 cP) there is no detectable change in the spectral diffusion time.

It is clear that the torsional relaxation time of BCT is solvent independent. DFT calculations suggest a possible explanation for the solvent independence when examining the molecular volumes of the two states, which differ by less than 5% in the two isomers. A small change in molecular volume indicates there is little change in solvent packing during the course of the reaction[21], suggesting that the solvent is not directly interacting with the torsional motion and that changes in solvent would not necessarily affect the spectral diffusion time. Changes in solvent-accessible surface area (~1%) are even smaller than molecular volume, further suggesting a weak influence of the solvent on the torsional motion. Because BCT is a small molecule, the linear alkane solvents are hindered by steric interactions and cannot pack close enough to the rotating benzene to damp the torsional motion. Finally, the three-state kinetic data shows that any time constant determined through our experiments is a factor of three too low due to the periodic nature of the system. This means that in reality decay of the FFCF is on the order of 10 ps, indicating there is in fact some significant baseline friction. This baseline friction stems from the approximation that the rotor is a rigid

rotor, when in reality the arene-Cr bond has been observed to change slightly with torsional motion in DFT calculations[17].

Solvent independence has been seen previously. For example, rebinding constants of the two monomer fragments of photodissociated cyclopentadienyl molybdenum(II) tricarbonyl dimer were found to be independent of solvent viscosity[35]. The independence of rebinding time from solvent properties was attributed to a "solvent cage," where the solvent created a cavity inside which the rebinding occurred. Other examples of solvent-independent reaction dynamics include the picosecond isomerization of a synthetic green fluorescent protein (GFP)[36]. Later isoviscosity studies showed that the isomerization rate was dependent on temperature, but only weakly dependent on viscosity[37]. It was suggested a volume conserving "hula-twist" mechanism for the internal conversion, which was used to explain the lack of viscosity dependence on the relaxation. This observation is consistent with our findings since BCT also has a small change in molecular volume and solvent accessible surface area as it progresses along its reaction coordinate.

6.4 Conclusion

By measuring spectral diffusion dynamics of the molecular rotor, BCT, we measured the reaction rate to be 9 ps in all solvents and indicating there to be no solvent dependence in the rotational motion. The FFCF can be used as a direct measure of reaction dynamics to probe motion along a torsional coordinate of BCT, which rapidly interconverts between a staggered and eclipsed structure at room temperature. A potential surface of the reaction coordinate of BCT was generated by DFT calculations

and was determined to be solvent independent by implementing a PCM to model several alkanes used in the experiments. Varying alkane chain length gave nearly identical values for the measured spectral diffusion time, leading us to conclude that the reaction occurs in a frictionless "solvent cage," free from damping by the solvent environment.

The exact mapping of frequencies to positions can be determined through a three-dimensional mapping of each carbonyl frequency and accounting for coupling to other carbonyls along the reaction coordinate. The potential could then be fit using a three-dimensional Morse potential model to determine the exact mapping. While an interesting computational problem, this work seeks mainly to show the solvent independence of a molecular rotor using RASD. The exact mapping of the frequencies to positions is not essential to the effect of the solvent on the torsional motion since relative changes in the timescale of the decay of the FFCF are observed and analyzed.

Future studies are needed to examine the effects of side chains and other groups on the torsional motion. In many cases, the impact of solvent friction on molecular reorientation can be represented using orientational diffusion with boundary conditions ranging from slip to slick limits. We find here that BCT appears to lie in the "slip" regime, where solvent friction does not hinder the rotation, while previous studies have shown that highly substituted BCT can slow the rotation to the NMR time scale, suggesting solvent friction influences the system dynamics or possibly that the barrier to rotation increases with substitution. BCT thus represents a model system for studying how molecular geometry affects the slip-stick properties of a molecule; the

slip-stick properties of BCT and its analogues in turn can be used as a representation of the damping and can explain the rotation timescales. In addition, in order to compare torsional timescales among molecules, other piano-stool complexes can be examined, looking explicitly for torsional motion on the few picosecond timescale.

In order to maximize the efficiency of a molecular rotor, it has been suggested that the time scale of the torsional motion should be significantly faster than the intramolecular vibrational energy redistribution (IVR)[38]. Investigation of ultrafast dynamics, by directly probing the torsional coordinate, will yield new information about the motion of low-barrier rotors especially with regard to interactions between the rotor and the surrounding environment. To create and control highly efficient synthetic molecular machines, we must understand both the active components that guide input energy to drive directional motion as well as the passive elements of the machine that are subject to fluctuations in their surroundings. Macroscopic machines typically require lubrication to overcome friction. This study suggests that for the motion of some nanoscale components, friction may be largely absent.

6.6 References

1. Kottas, G. S.; Clarke, L. I.; Horinek, D.; Michl, J., "Artificial molecular rotors". *Chemical Reviews* **2005,** *105* (4), 1281-1376.

2. Michl, J.; Sykes, E. C. H., "Molecular Rotors and Motors: Recent Advances and Future Challenges". *ACS Nano* **2009,** *3* (Copyright (C) 2012 American Chemical Society (ACS). All Rights Reserved.), 1042-1048.

3. Kuimova, M. K.; Yahioglu, G.; Levitt, J. A.; Suhling, K., "Molecular Rotor Measures Viscosity of Live Cells via Fluorescence Lifetime Imaging". *J. Am. Chem. Soc.* **2008,** *130* (Copyright (C) 2012 American Chemical Society (ACS). All Rights Reserved.), 6672-6673.

4. Haidekker, M. A.; Theodorakis, E. A., "Molecular rotors-fluorescent biosensors for viscosity and flow". *Org. Biomol. Chem.* **2007,** *5* (Copyright (C) 2012 American Chemical Society (ACS). All Rights Reserved.), 1669-1678.

5. Koumura, N.; Zijlstra, R. W.; van, D. R. A.; Harada, N.; Feringa, B. L., "Light-driven monodirectional molecular rotor". *Nature* **1999,** *401* (Copyright (C) 2012 U.S. National Library of Medicine.), 152-5.

6. Conyard, J.; Addison, K.; Heisler, I. A.; Cnossen, A.; Browne, W. R.; Feringa, B. L.; Meech, S. R., "Ultrafast dynamics in the power stroke of a molecular rotary motor". *Nat. Chem.* **2012,** *4* (Copyright (C) 2012 American Chemical Society (ACS). All Rights Reserved.), 547-551.

7. Astumian, R. D., "Thermodynamics and Kinetics of a Brownian Motor". *Science* **1997,** *276* (5314), 917-922.

8. Du Plooy, K. E.; Marais, C. F.; Carlton, L.; Hunter, R.; Boeyens, J. C. A.; Coville, N. J., "Steric effects associated with monosubstituted cyclopentadienyl transition-metal complexes. Synthesis and NMR spectroscopic and molecular mechanics study of [(.eta.5-C5H4Bu-tert)Fe(CO)(L)I] complexes and crystal structure determination of [(.eta.5-C5H4Bu-tert)Fe(CO)(PPh3)I]". *Inorganic Chemistry* **1989,** *28* (20), 3855-3860.

9. Eisenberg, A.; Shaver, A.; Tsutsui, T., "Mechanical spectroscopy: a new technique for measuring ring rotation in organometallic complexes". *Journal of the American Chemical Society* **1980,** *102* (4), 1416-1417.

10. Hansen, V. M.; Batchelor, R. J.; Einstein, F. W. B.; Male, J. L.; Pomeroy, R. K.; Zaworotko, M. J., "Restricted Rotation about the Arene−Iron Bond in (arene)Fe(CO)(SiCl3)2 Complexes". *Organometallics* **1997,** *16* (22), 4875-4881.

11. Gracey, D. E. F.; Jackson, W. R.; Jennings, W. B.; Rennison, S. C.; Spratt, R., "Restricted rotation in some tricarbonyl(arene)chromium compounds". *Chem. Commun. (London)* **1966,** (Copyright (C) 2012 American Chemical Society (ACS). All Rights Reserved.), 231-2.

12. Jackson, W. R.; Jennings, W. B.; Spratt, R., "Restricted rotation in tricarbonyl(arene)chromiums". *Journal of the Chemical Society D: Chemical Communications* **1970,** (10), 593.

13. Jula, T. F.; Seyferth, D., "Nuclear magnetic resonance spectra of some arenechromium tricarbonyl complexes containing trimethyl Group IVb metal substituents". *Inorg. Chem.* **1968,** *7* (Copyright (C) 2012 American Chemical Society (ACS). All Rights Reserved.), 1245-6.

14. Downton, P. A.; Mailvaganam, B.; Frampton, C. S.; Sayer, B. G.; McGlinchey, M. J., "UNEQUIVOCAL PROOF OF SLOWED CHROMIUM TRICARBONYL ROTATION

IN A STERICALLY CROWDED ARENE COMPLEX - AN X-RAY CRYSTALLOGRAPHIC AND VARIABLE-TEMPERATURE HIGH-FIELD NMR-STUDY OF (C6ET5COCH3)CR(CO)3". *Journal of the American Chemical Society* **1990,** *112* (1), 27-32.

15. McGlinchey, M. J., "Slowed Tripodal Rotation in Arene-Chromium Complexes: Steric and Electronic Barriers". **1992,** *34*, 285-325.

16. Spears, K. G., "Density functional study of geometry and vibrational spectra for the isoelectronic V(CO)(6)(-) and Cr(CO)(6) molecules". *Journal of Physical Chemistry A* **1997,** *101* (35), 6273-6279.

17. Low, A. A.; Hall, M. B., "Benzene chromium tricarbonyl revisited: Theoretical study of the structure and dynamics of (eta(6)-C(6)H(6))Cr(CO)(3)". *International Journal of Quantum Chemistry* **2000,** *77* (1), 152-160.

18. Gribanova, T. N.; Minyaev, R. M.; Starikov, A. G.; Minkin, V. I., "pi-Complexes of transition metal tricarbonyls with cyclopolyenes and their boron analogs". *Russian Chemical Bulletin* **2009,** *58* (4), 691-705.

19. Cahoon, J. F.; Sawyer, K. R.; Schlegel, J. P.; Harris, C. B., "Determining Transition-State Geometries in Liquids Using 2D-IR". *Science* **2008,** *319* (5871), 1820-1823.

20. Gaussian 03, Revision C.02,
M. J. Frisch, G. W. Trucks, H. B. Schlegel, G. E. Scuseria,
M. A. Robb, J. R. Cheeseman, J. A. Montgomery, Jr., T. Vreven,
K. N. Kudin, J. C. Burant, J. M. Millam, S. S. Iyengar, J. Tomasi,
V. Barone, B. Mennucci, M. Cossi, G. Scalmani, N. Rega,
G. A. Petersson, H. Nakatsuji, M. Hada, M. Ehara, K. Toyota,
R. Fukuda, J. Hasegawa, M. Ishida, T. Nakajima, Y. Honda, O. Kitao,
H. Nakai, M. Klene, X. Li, J. E. Knox, H. P. Hratchian, J. B. Cross,
C. Adamo, J. Jaramillo, R. Gomperts, R. E. Stratmann, O. Yazyev,
A. J. Austin, R. Cammi, C. Pomelli, J. W. Ochterski, P. Y. Ayala,
K. Morokuma, G. A. Voth, P. Salvador, J. J. Dannenberg,
V. G. Zakrzewski, S. Dapprich, A. D. Daniels, M. C. Strain,
O. Farkas, D. K. Malick, A. D. Rabuck, K. Raghavachari,
J. B. Foresman, J. V. Ortiz, Q. Cui, A. G. Baboul, S. Clifford,
J. Cioslowski, B. B. Stefanov, G. Liu, A. Liashenko, P. Piskorz,
I. Komaromi, R. L. Martin, D. J. Fox, T. Keith, M. A. Al-Laham,
C. Y. Peng, A. Nanayakkara, M. Challacombe, P. M. W. Gill,
B. Johnson, W. Chen, M. W. Wong, C. Gonzalez, and J. A. Pople,
Gaussian, Inc., Wallingford CT, 2004.

21. Anna, J. M.; King, J. T.; Kubarych, K. J., "Multiple Structures and Dynamics of [CpRu(CO)2]2 and [CpFe(CO)2]2 in Solution Revealed with Two-Dimensional Infrared Spectroscopy". *Inorg. Chem. (Washington, DC, U. S.)* **2011,** *50* (Copyright (C) 2012

American Chemical Society (ACS). All Rights Reserved.), 9273-9283.

22. Osborne, D. G.; Kubarych, K. J., "Rapid and Accurate Measurement of the Frequency–Frequency Correlation Function". *The Journal of Physical Chemistry A* **2012**.

23. Gaussian 09, Revision A.02,
M. J. Frisch, G. W. Trucks, H. B. Schlegel, G. E. Scuseria,
M. A. Robb, J. R. Cheeseman, G. Scalmani, V. Barone, B. Mennucci,
G. A. Petersson, H. Nakatsuji, M. Caricato, X. Li, H. P. Hratchian,
A. F. Izmaylov, J. Bloino, G. Zheng, J. L. Sonnenberg, M. Hada,
M. Ehara, K. Toyota, R. Fukuda, J. Hasegawa, M. Ishida, T. Nakajima,
Y. Honda, O. Kitao, H. Nakai, T. Vreven, J. A. Montgomery, Jr.,
J. E. Peralta, F. Ogliaro, M. Bearpark, J. J. Heyd, E. Brothers,
K. N. Kudin, V. N. Staroverov, R. Kobayashi, J. Normand,
K. Raghavachari, A. Rendell, J. C. Burant, S. S. Iyengar, J. Tomasi,
M. Cossi, N. Rega, J. M. Millam, M. Klene, J. E. Knox, J. B. Cross,
V. Bakken, C. Adamo, J. Jaramillo, R. Gomperts, R. E. Stratmann,
O. Yazyev, A. J. Austin, R. Cammi, C. Pomelli, J. W. Ochterski,
R. L. Martin, K. Morokuma, V. G. Zakrzewski, G. A. Voth,
P. Salvador, J. J. Dannenberg, S. Dapprich, A. D. Daniels,
O. Farkas, J. B. Foresman, J. V. Ortiz, J. Cioslowski,
and D. J. Fox, Gaussian, Inc., Wallingford CT, 2009.

24. Park, S.; Park, J.-S.; Joo, T., "Solvation Dynamics by Coherence Period Resolved Transient Grating". *J. Phys. Chem. A* **2011,** *115* (Copyright (C) 2012 American Chemical Society (ACS). All Rights Reserved.), 3973-3979.

25. Joo, T.; Jia, Y.; Yu, J.-Y.; Lang, M. J.; Fleming, G. R., "Third-order nonlinear time domain probes of solvation dynamics". *J. Chem. Phys.* **1996,** *104* (Copyright (C) 2012 American Chemical Society (ACS). All Rights Reserved.), 6089-108.

26. Asbury, J. B.; Steinel, T.; Stromberg, C.; Corcelli, S. A.; Lawrence, C. P.; Skinner, J. L.; Fayer, M. D., "Water Dynamics: Vibrational Echo Correlation Spectroscopy and Comparison to Molecular Dynamics Simulations". *The Journal of Physical Chemistry A* **2004,** *108* (7), 1107-1119.

27. Eaves, J. D.; Loparo, J. J.; Fecko, C. J.; Roberts, S. T.; Tokmakoff, A.; Geissler, P. L., "Hydrogen bonds in liquid water are broken only fleetingly". *Proc. Natl. Acad. Sci. U. S. A.* **2005,** *102* (37), 13019-13022.

28. Osborne, Derek G.; Kubarych, Kevin J. submitted

29. Nee, M. J.; Baiz, C. R.; Anna, J. M.; McCanne, R.; Kubarych, K. J., "Multilevel vibrational coherence transfer and wavepacket dynamics probed with multidimensional IR spectroscopy". *The Journal of chemical physics* **2008,** *129* (8), 084503-11.

30. Roberts, S. T.; Loparo, J. J.; Tokmakoff, A., "Characterization of spectral diffusion from two-dimensional line shapes". *J. Chem. Phys.* **2006,** *125* (Copyright (C) 2012 American Chemical Society (ACS). All Rights Reserved.), 084502/1-084502/8.

31. Field, C. N.; Green, J. C.; Moody, A. G. J.; Siggel, M. R. F., "A photoelectron study of the electronic structure of (eta-C6H6) Cr(CO)(3) and (eta-C5H5) Mn(CO)(3) using variable photon energy". *Chemical Physics* **1996,** *206* (1-2), 211-223.

32. Andersson, M. P.; Uvdal, P., "New Scale Factors for Harmonic Vibrational Frequencies Using the B3LYP Density Functional Method with the Triple-ζ Basis Set 6-311+G(d,p)". *J. Phys. Chem. A* **2005,** *109* (Copyright (C) 2012 American Chemical Society (ACS). All Rights Reserved.), 2937-2941.

33. Anna, J. M.; Kubarych, K. J., "Watching solvent friction impede ultrafast barrier crossings: A direct test of Kramers theory". *J. Chem. Phys.* **2010,** *133* (Copyright (C) 2012 American Chemical Society (ACS). All Rights Reserved.), 174506/1-174506/12.

34. King, J. T.; Baiz, C. R.; Kubarych, K. J., "Solvent-Dependent Spectral Diffusion in a Hydrogen Bonded "Vibrational Aggregate"". *The Journal of Physical Chemistry A* **2010,** *114* (39), 10590-10604.

35. Baiz, C. R., McCanne, R., and Kubarych, K. J., 2011, Ultrafast Phenomena XVII, M. Chergui, D. M. Jonas, E. Riedle, R. W. Schoenlein, A. J. Taylor, eds. (New York: Oxford University Press), p. 400-402.

36. Webber, N. M.; Litvinenko, K. L.; Meech, S. R., "Radiationless relaxation in a synthetic analogue of the green fluorescent protein chromophore". *J. Phys. Chem. B* **2001,** *105* (Copyright (C) 2012 American Chemical Society (ACS). All Rights Reserved.), 8036-8039.

37. Litvinenko, K. L.; Webber, N. M.; Meech, S. R., "Internal Conversion in the Chromophore of the Green Fluorescent Protein: Temperature Dependence and Isoviscosity Analysis". *J. Phys. Chem. A* **2003,** *107* (Copyright (C) 2012 American Chemical Society (ACS). All Rights Reserved.), 2616-2623.

38. Miller, R. J. D., "Photochemistry: Molecular motor speed limits". *Nat Chem* **2012,** *4* (7), 523-525.

Chapter Seven

Rapidly Acquired Spectral Diffusion Tutorial

7.1 Introduction

Rapidly acquired spectral diffusion (RASD) is an accurate and rapid method used to measure spectral diffusion. The theoretical development and comparison to alternative spectral diffusion measurement methods is present in chapter two of this Thesis. Although measuring the spectral diffusion with RASD is useful and time saving, it is important that care is taken in selecting the appropriate t_1 delay (section 7.3) before data is acquired (section 7.4).

7.2 Initializing the Setup

The initialization steps for the RASD experiment are similar to those for the "Box Geometry" 2DIR setup. Begin the experiment by turning the laser on and letting the laser warm up for approximately 30 min. Once the setup is warmed up, adjust the setup to maximize the signal, followed by interfering the signal with the local oscillator.

Aligning the local oscillator is often taken for granted despite its ability to dramatically increase the signal to noise, so take your time with this process. I prefer to maximize the signal first with DMDC, tune to the mode of interest, and then maximize the signal again. After the laser is warmed up and the setup is aligned, I compare the amplitude of the signal after it is left alone for 15 min to test the stability of the setup.

7.3 Determining the t_1 Delay

Selecting the t_1 delay and the location of the rephasing and nonrephasing motors requires multiple steps.

1) Zero the motor positions for the rephasing, nonrephasing, and t_2 motors before the experiment through the DSP A and DSP B interactive programs in LabVIEW. This insures that the motors return to their proper location throughout the experiment.
2) Following the protocol for a standard 2DIR experiment, both the rephasing and nonrephasing wedges must be calibrated.
3) Collect data while scanning the t_1 delay for both the rephasing and nonrephasing motors using the 2DIR data acquisition program in LabVIEW. At the time of this publication, it is named "2D Spectrometer_SITK_Stable". When the t_1 delay is scanned, it is best if k_3 is not overlapped with the other two pulses. To do this, set the base path appropriately under the "Filenames" tab. Next, select "Batch Collection" and "Absorptive" under the "Data Collection" tab, and set "Initial Time," "Final Time," "Num," and "t2 Delay Function" to "0.25", "0.25", "1", and "Linear" respectively. The parameters are set by pushing the "Set Parameters"

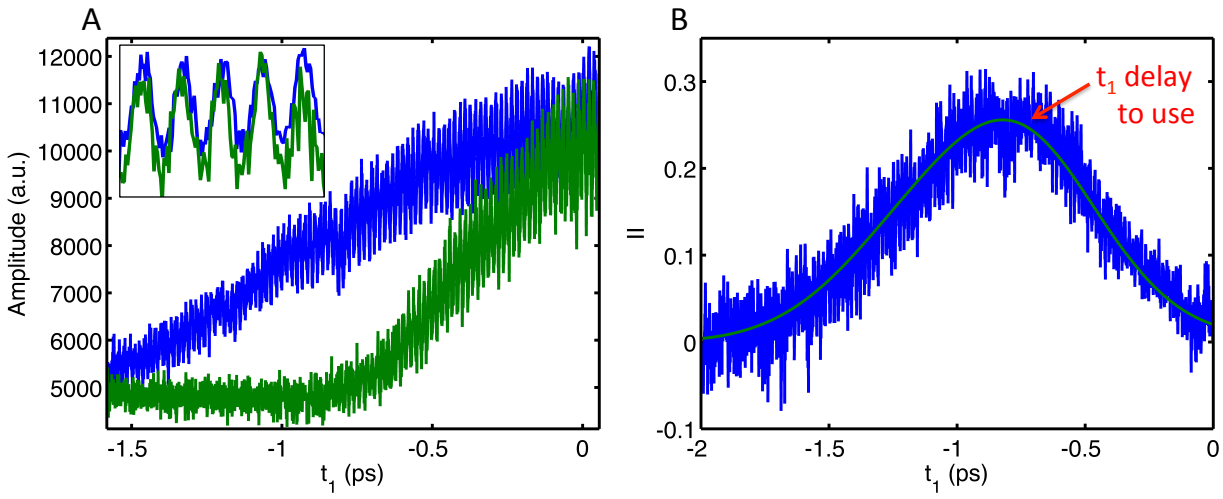

Figure 7.1 (A) The t_1 dependence of the rephasing and nonrephasing signals, and (B) the t_1 dependence of the inhomogeneous index. While using the RASD_t1_calc.m script in matlab, these figures are plotted as "figure 22" and "figure 11" respectively.

button which will cause four "0.25" to appear under "Time Steps". These parameters will cause the program to collect two rephasing and two nonrephasing spectra.

4) The data from the previous set is used to plot the amplitude of the signal as a function of t_1 for both a rephasing and nonrephasing scan. This is done with the "variables" Matlab analysis program that is used for the 2DIR analysis. To accomplish this, run the analysis script for the first two files of the data taken in the previous step with the variable "settings.outputEfield" set to true and selecting the pixel range that corresponds to the mode of interest with the variable "settings.PixStart" and "settings.PixEnd". If you do not know the pixel range of your mode, stop Matlab at line 12 of the gen2Dspec.m function (main.m > analysis.m > gen2Dspec.m). Plot all of the data acquired by typing "imagesc(abs(eField))" in the command window of matlab. I find that the best signal to noise is with a narrow pixel range. Due to the method used to save the

data, if "variables" is run multiple times with different pixel ranges, Matlab with encounter an error. To get around this, change the output base path by changing the "extra" variable.

5) Selecting the appropriate t_1 delay is done with the Matlab program "RASD_t1_calc.m." Begin with the "t1time" and "resp_t1_adjust" set to 0. Using "figure 22" (**Fig. 1A**), adjust the "resp_t1_adjust" variable such that the maximum of both the rephasing and nonrephasing times are overlapped. Due to the interference pattern of the first two pulses in the frequency domain, the decay will have a fast oscillating component. These peaks must be overlapped as well (**Fig. 1A inset**). In "figure 11" (**Fig. 1B**), select the t_1 time that has the maximum inhomogeneous index. Generally, there will be a range of t_1 delays that will have the same magnitude of inhomogeneous index; I prefer to choose the smallest t_1 delay of that range to maximize the signal to noise. It is important that the high frequency oscillations are overlapped at the t_1 delay that will be used. If they are not overlapped, an error has occurred in the wedge calibration process.
6) The location for the rephasing and nonrephasing delays will be outputted in the Matlab Command window as "rep_clicks" and "non_clicks." Always note the t_1 delay and both of the rephasing and nonrephasing clicks used in the experiment in your lab notebook.

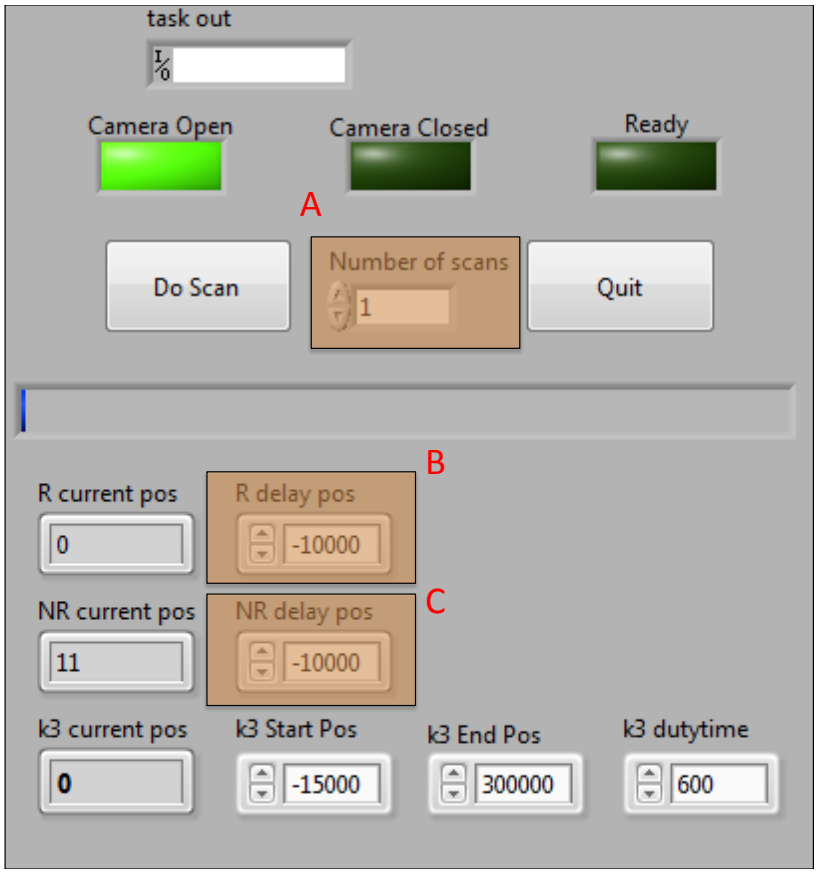

Figure 7.2 The front panel of the "RASD_Stable_DO" program in LabVIEW. Before using this program, it is important to determine the rephasing and nonrephasing positions using the steps in section 7.3.

7.4 Data Acquisition and Analysis

1) The program "RASD_Stable_DO" in LabVIEW is used to acquire the RASD data. When initializing the "RASD_Stable_DO" program, the experiment number should be reset to zero and a correct path needs to be set. "rep_clicks" and "non_clicks" should be inputted at their appropriate places, **Figure 2 B** and **C** respectively. The variable "number of scans" (**Fig 2C**) controls how many scans the experiment is averaged over. For example, If "number of scans" is 4, the rephasing and nonrephasing motors will both scan four times.
2) Analysis of RASD is carried out with the "fast_spectral_diffusion" script in

matlab. In the analysis script, appropriatly set the "path.inputbasepath," "expNum", "settings.PixStart" and "setting.PixEnd." The analysis script will save the data in "path.inputbasepath" as "fsd_out(exp num)".

7.5 Laser Drift

It is possible that during the course of data acquisition the laser will drift, changing the optical path lengths of the laser generated pulses causing the t_1 delays to change. If this happens, the offsets cannot be used. It is possible to set up a "phase locked" system to prevent this problem but has not been initiated in the Kubarych lab.

Chapter Eight

Conclusion

8.1 Introduction

The cytosol of a living cell is a complex and crowded space containing a diverse group of biological macromolecules that include polypeptides, tRNA, mRNA, ribosomes, and lipid membranes[1]. Each biological macromolecule will disrupt the hydrogen bonding network water often leaving the interfacial water with hanging hydrogen bonds[2] and causing the time scales for hydrogen bond reorganization of the interfacial water to differ from that of bulk water[3-5]. Because the dynamics of water have a strong influence on many biological reactions and processes, it is critical to study how biological macromolecules alter the dynamics of water if *in vivo* reactions are to be fully understood[3-7].

The focus of this thesis is the development of ultrafast vibrational techniques, in particular spectral diffusion, capable of robustly studying the dynamics of interfacial water and can be broken into three categories: the development of spectroscopic and

data processing techniques that accelerate data acquisition, the synthesis and characterization of the chol-BCT metal carbonyl label capable of measuring the hydrogen bond reorganization times scales at the lipid membrane-water interface, and lastly a standardization of spectral diffusion's dependence on nanoconfinement. This work demonstrates that the spectral diffusion data acquisition time can be greatly accelerated while maintaining high accuracy, a metal carbonyl in a biological macromolecule is an ideal label of the interfacial water's dynamics, and spectral dynamics could potentially be a measure of thermodynamic properties.

8.2 Rapidly Acquired Spectral Diffusion

The measurements of 2DIR spectra at a series of t_2 delays have the ability to measure the spectral diffusion along with the intermolecular vibrational energy redistribution (IVR), and chemical exchange[8], but the data acquisition and processing time for these experiments are often long[9]. Chapter two of this thesis demonstrates that the pulse sequence used for 2DIR can be slightly modified – scanning the t_2 delay while maintaining a constant t_1 delay – to accelerate the data acquisition and processing of spectral diffusion measurements. Along with a reduction in data acquisition time, nearly an order of magnitude faster, rapidly acquired spectral diffusion (RASD) also increases the number of data points, approximately 50 fold. We test the ability of RASD to reproduce spectral diffusion measurements by comparing its results to 2DIR, and find RASD accurately reproduces the 2DIR measured spectral diffusion time scales, which suggests that RASD is an ideal method for measuring spectral diffusion.

8.3 Compressed Sensing

Although RASD accelerates the data acquisition of spectral diffusion measurements, it does not have the ability of 2DIR to simultaneously measure IVR and chemical exchange and their ability to give further insight into the hydrogen bonding network[10] and solvent dynamics[11]. In chapter three, we test the ability of a novel data processing technique, compressed sensing (CS), to replicate 2DIR measurements, while maintaining the 2DIR pulse sequence and its ability to measure IVR and chemical exchange. The CS processing technique assumes the data measured in the time domain is sparse in the frequency domain[12, 13], as many vibrational signals are[13], which allows for the number of measured time domain data points to be greatly reduced while maintaining the same quality of data. We found that a ~30 fold reduction in data acquisition time accurately reproduces the 2DIR measurements, which suggests that CS is an ideal method for measuring IVR and chemical exchange experiments.

8.4 chol-BCT Synthesis and Characterization

Chapters two and three are devoted to the development of data acquisition and processing techniques that accelerate spectral diffusion measurements while chapter four demonstrates a synthesis protocol for the labeling of a lipid membrane allowing these data acquisition and processing techniques to probe the lipid membrane's interfacial water. The synthesis of chapter four is of the (cholesteryl benzoate)

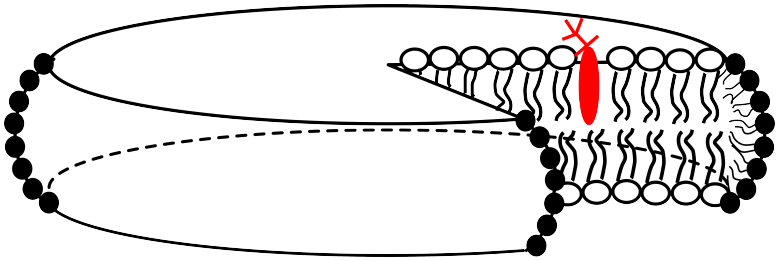

Figure 8.1. The (cholesteryl benzoate) chromium tricarbonyl (red) is embedded in a lipid bicelle such that the tricarbonyl complex is at the interface of the water and lipid bilayer.

chromium tricarbonyl complex (chol-BCT), which we then embed into the lipid membrane (**Fig. 8.1**). We characterize the location of the chromium tricarbonyl motif and its orientation in the lipid membrane through FTIR spectroscopy and polarized ATR methods, which indicate that the chromium tricarbonyl motif is located at the interface between the membrane and the water and is oriented such that the vector normal to the benzene ring is 46˚ from the vector normal to the lipid membrane. The work of chapter four is centered on the synthesis of chol-BCT but preliminary work suggests that these methods could be a ubiquitous labeling method of biological macromolecules.

8.5 Nanoconfinement

The work of chapter five set out to standardize the effect nanoconfinement has on spectral diffusion by confining a small metal carbonyl compound, cyclopentadienyl manganese tricarbonyl (CMT), in a simple organic complex, β-cyclodextrin. We measured the spectral diffusion time constant in a series of linear alcohol solvents and found that the time scales of CMT confined in β-cyclodextrin are consistently faster than

that of CMT in a neat alcohol. These results are surprising because molecular dynamic (MD) simulations of β-cyclodextrin in methanol measured the orientational correlation function of methanol to slow near the β-cyclodextrin complex. We attribute the measured spectral diffusion trends to the β-cyclodextrin causing the number of solvating alcohol molecules to be reduced, which will then reduce the size of the conformational space of the available microenvironments. We tested this hypothesis by comparing the spectral diffusion time constants of CMT and CMT complexed with β-cyclodextrin to another metal carbonyl compound, dimanganese decacarbonyl (DMDC), and performing a Monte Carlo simulation. Both comparisons agree with the hypothesis that the number of solvating alcohol molecules is indeed altering the spectral diffusion timescales. These results indicate that there is an inherent correlation between spectral diffusion time scales and conformational space, which suggests that the spectral dynamics could be used as a measurement of the local entropy.

8.6 Measuring Interfacial Water Dynamics

The work of this thesis is the development of novel techniques to measure the dynamics of a biological macromolecule's interfacial water. To test the ability of these techniques, in particular the use of RASD and synthesis of chol-BCT, we compare the spectral diffusion time constants of the chromium tricarbonyl motif in bulk water and at the water-membrane interface. Although the chol-BCT complex has a low solubility in water, a similar chromium tricarbonyl complex (benzoate acid) chromium tricarbonyl is water soluble (**Fig. 8.2**). Utilizing the RASD technique, we measure the (benzoate)

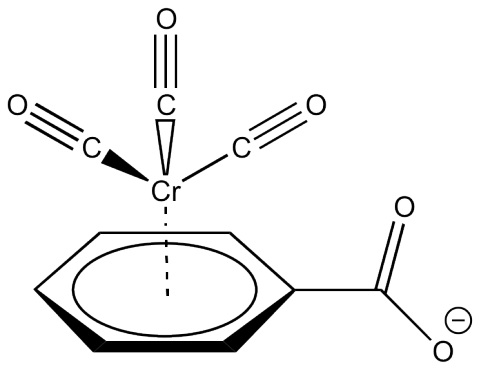

Figure 8.2. The (benzoate acid) chromium tricarbonyl complex is water soluble due to the deprotonated carboxylic acid. We use (benzoate acid) chromium tricarbonyl in bulk water to calibrate the spectral diffusion time scales of a chromium tricarbonyl motif and find that the spectral diffusion time constants of (benzoate acid) chromium tricarbonyl match that of water's OH stretch in bulk water.

chromium tricarbonyl complex to have a spectral diffusion time constant of 1.55 ± 0.25 ps, which compares favorably to the spectral diffusion time scale of the OH stretch in D_2O, 1.6 ps[14], suggesting that the spectral diffusion time constant of chromium tricarbonyl motif, as is the OH stretch, is a direct measure of the hydrogen bond network reorganization[15, 16]. It is not surprising to find the spectral diffusion time scales of a metal carbonyl motif in D_2O to match that of OH stretch in D_2O; previous 2DIR experiments measured the spectral diffusion time constants of metal carbonyl complexes CORM-2 and PI-CORM in D_2O to be 1.5 ± 0.3 ps and 1.6 ± 0.4 ps respectively[6]. With the RASD technique, we measured the spectral diffusion time constant of chol-BCT embedded in a bicelle to be more than a factor of two slower, 3.8 ± 0.08 ps, than the chromium tricarbonyl motif in bulk D_2O. This matches the spectral diffusion time constant of the OH stretch in a reverse micelle, 3.5 ± 0.5 ps, confirming chromium tricarbonyl's ability to measure the hydrogen bond network reorganization (**Fig. 8.3**). These experiments demonstrate the utility of chol-BCT as a

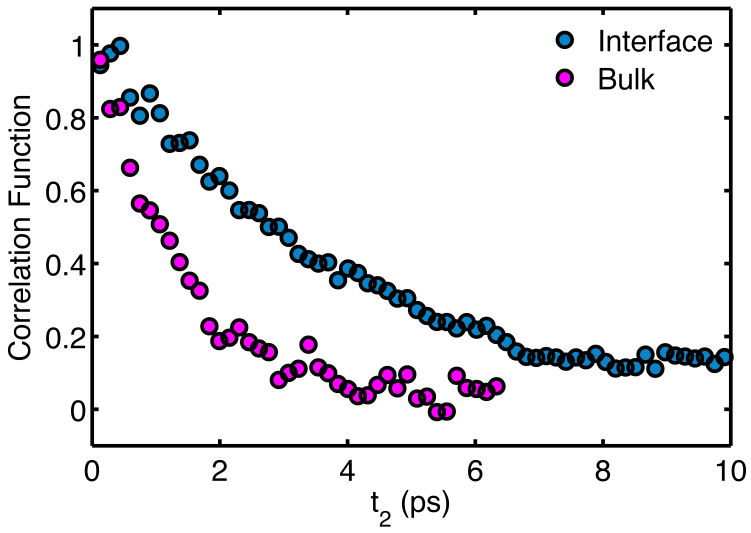

Figure 8.3. Using the chromium tricarbonyl motif to measure the frequency-frequency correlation function of interfacial and bulk water with RASD. The black lines are the exponential fits from Matlab. Due to the excess number of data points, we only plot one in 30 data points.

probe of a lipid membrane's interfacial water and the RASD technique as a rapid and accurate method of measuring the spectral diffusion.

8.7 Future Work

The work of this thesis focuses on the development of techniques to improve the use of ultrafast vibrational spectroscopy as a tool in biophysical research. This work includes the development of both spectroscopic techniques to accelerate the data acquisition process (chapters two and three) and a synthesis protocol to label biological macromolecules (chapter four). Previously in this manuscript, we demonstrated that these techniques together are capable of measuring the dynamics of interfacial water of a DMPC/DHPC bicelle, but these techniques are not limited to a simple bicelle. Further work will be required to fully utilize the techniques used in this thesis including: determining the interfacial water dynamics of complex lipid membranes, exploring the phase diagram of lipids, measuring the aggregation of the lipid subunits, and imaging

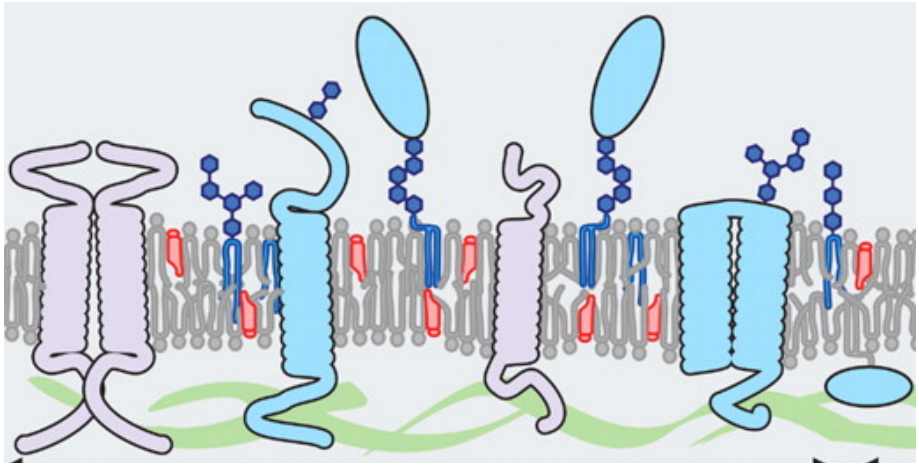

Figure 8.4. The lipid membrane of a living cell is a complex space with a variety of subunits including proteins, carbohydrates, and cholesterol. Future work is required to fully explore how these subunits alter the interfacial water dynamics. Adapted from ref. 17

the function of a cell *in vivo*.

8.7.1 Bicelle experiments. The structure of a lipid membrane *in vivo* is complex containing a variety of functional groups and macromolecules – *e.g.* cholesterol, proteins, carbohydrates, and a variety of lipid head groups (**Fig. 8.4**) – making the study of interfacial water of a cell's lipid membrane complex, but the abilities of the techniques presented here allow for the systematic study of the lipid membrane's interfacial water. For example, consider the phosphatidylcholine (PC) and phosphatidylglycerol (PG) head groups; the choline group of PC is positively charged while the phosphate group is negatively charged creating a zwitterionic head group while the glycerol group of PG is neutrally charged causing the PG head group to be negatively charged. The charge difference between the PC and PG head groups could cause the interfacial water to have different hydrogen bond networks and therefore different hydration dynamics. Using the chol-BCT as a label and RASD as a measure of the hydration dynamics, it would be possible to measure the hydration dynamics of

bicelle containing only PC head groups (as presented in this manuscript), and only PG head groups. If the PC and PG head groups induce the interfacial water to have different dynamics, the additive nature of these dynamics could be determined by measuring the dynamics of interfacial water in a series of PC-PG mixtures. For example, does a 50/50 ratio of phosphatidylcholine to phosphatidylglycerol exhibit hydration dynamics corresponding to the average of the PC and PG? Because the living cell's lipid membrane is complex, multiple experiments similar to that of the phosphatidylcholine-phosphatidylglycerol described here are possible by systematically increasing the membrane's complexity by, for example, incorporating carbohydrates, cholesterol, and proteins to the bicelle.

A bicelle can also be used to determine how the size of a solute will alter the dynamics of interfacial water. The size of a bicelle is determined by the ratio of short alkane chain lipids to long alkane chain lipids in the sample. It would therefore be simple to measure the interfacial water dynamics at a series of bicelle sizes ranging from 3 to 20 nm. Because the head group has the ability to alter the hydration dynamics of interfacial water, it is important to design this experiment with a non-perturbative head group (*e.g.* bis(2-ethylhexyl) succinate).

8.7.2 Monoolein. A lipid-water mixture can be found in multiple phases that are dependent on the concentration of the lipid and the temperature of the sample. These phases are based on simple topologies that include layers, tubes, spheres or more complex topologies that are based the mathematical minimal surfaces. Monoolein is a simple amphiphilic lipid that can form many topological phases and is often studied

due to its many industrial applications. The structure of the monoolein throughout these phases is well studied but the dependence of the interfacial water dynamics on these phases has not yet been studied. Currently in the Kubarych laboratory, efforts are being made to label the hydroxyl group of the monoolein with the chromium tricarbonyl motif using the same esterification used to synthesize the chol-BCT complex in chapter four. Using the labeled monoolein complex, the interfacial water dynamics can be measured for each phase by simply adjusting the lipid concentration or the temperature. Because a change in the temperature by itself could alter the water dynamics, it is important to use (benzoate) chromium tricarbonyl in bulk solution as a control for how temperature alters the water dynamics near the chromium tricarbonyl.

8.7.3 Multiple Labels. Metal carbonyl complexes are ideal labels for ultrafast vibrational spectroscopy due to their large transition dipole moments at frequencies in a relatively uncluttered region of the spectrum. In this thesis, we have utilized the piano stool metal carbonyl motif of the (benzyl) chromium tricarbonyl complex (BCT) because the organic benzyl group allows for the use of standard organic chemistry in a labeling protocol, but BCT is not the only piano stool metal carbonyl motif. Two, of the many, alternative piano stool metal carbonyl motifs are the cyclopentadienyl manganese tricarbonyl (CMT) and cyclopentadienyl rhodium tricarbonyl (CRT) complexes whose linear vibrational spectra have the same two peaks spectrum of BCT, but are slightly shifted relative to that of BCT. If the organic rings of CMT and CRT were to be functionalized with a carboxylic acid, presumably they could be used to label hydroxyl groups as is BCT. Preliminary data suggest that the simple esterification presented in

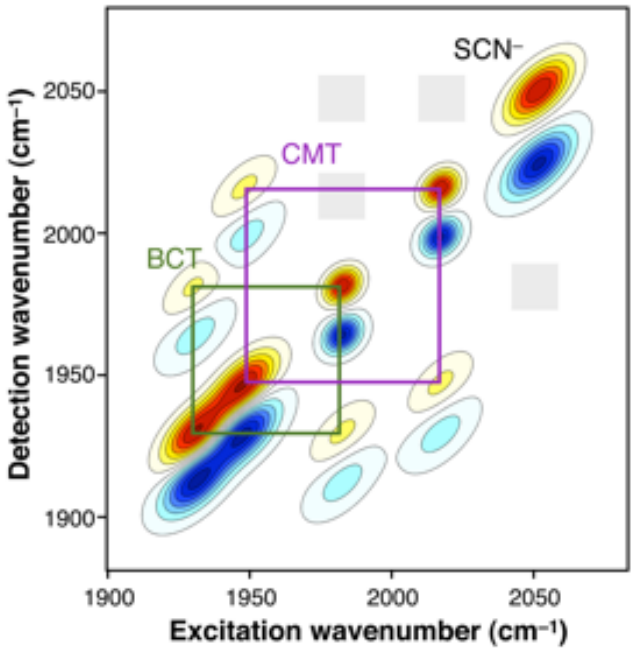

Figure 8.5. The diagonal of a 2DIR spectrum containing BCT and CMT will have four peaks; two peaks from CMT and two from BCT. If BCT and CMT are near each other, BCT and CMT will exchange energy creating cross peaks between the BCT and CMT peaks. The t_2 dependence of these cross peak amplitudes will indicate the distance between the molecules.

chapter four could be used to label the hydroxyl groups of 1-palmitoyl-2-oleoyl-sn-glycero-3-phosphoglycerol and 1,2-dipalmitoyl-sn-glycerol with the chromium tricarbonyl motif and therefore could also be labeled with the similar piano stool molecules of CMT and CRT, allowing for a more complex experiments where a variety of lipid components could be labeled with different piano stool molecules.

One possible experiment utilizing this multiple labeled lipid would be the aggregation of a lipid's components. If two components of a lipid that are known to aggregate are labeled with two different piano stool labels, the rate of intermolecular energy transfer could be used as a measure of distance between the two different labels. In a 2DIR spectrum, the energy transfer between two labels can be determined through the cross peak between the modes (**Fig. 8.5**), while the t_2 dependence of the cross peak

volume is a measure of the rate of energy transfer and therefore the distance between labels. Also, piano stool metal carbonyl complexes have been used as labels for *in vivo* Raman imaging. With these multiple piano stool complexes and the esterification presented in chapter four, the use of piano stool complexes in Raman imaging can be greatly enhanced.

8.7.4 Photo bleaching. Lastly, the use of UV light to photodissociate a carbonyl could be used to site specifically probe a region of a sample. In previous experiments not presented in the thesis, we confined the BCT molecule in β-cyclodextrin and found the linear spectrum of the carbonyls to have duplicate peaks slightly shifted in the spectrum that we attributed to a portion of the complexes oriented with the carbonyls exposed to the solvent while the others had the carbonyls confined in the β-cyclodextrin. Illuminating this heterogeneous sample with UV light, one set of the peaks in the linear spectrum was bleached. Although all of the BCT molecules are photobleached, the carbonyls confined in the β-cyclodextrin rebind because of their inability to diffuse away from the chromium metal. Potentially, if a vesicle (with both an exterior and confined interior) were labeled and then photobleached, the carbonyls on the interior would rebind while the exterior carbonyls would be permanently bleached allowing for the interior to be exclusively labeled.

8.7 Closing

Despite the measurements of interfacial water's hydrogen bond network reorganization discussed above, further experiments are required to explore the

interfacial water dynamics in more biologically relevant environments. These experiments should include: additional head groups varieties, varying concentrations of cholesterol, bound polypeptide chains, multiple pHs, and many more. It is my hope that future generations of graduate students will be able to utilize the methods outlined in this thesis to explore the nature of the interfacial water solvating biological macromolecules.

8.8 References

1. Zimmerman, S. B.; Trach, S. O., "Estimation of macromolecule concentrations and excluded volume effects for the cytoplasm of Escherichia coli". *Journal of Molecular Biology* **1991,** *222* (3), 599-620.

2. Chandler, D., "Interfaces and the driving force of hydrophobic assembly". *Nature* **2005,** *437* (7059), 640-647.

3. Zhou, H. X.; Rivas, G. N.; Minton, A. P., Macromolecular crowding and confinement: Biochemical, biophysical, and potential physiological consequences. In *Annual Review of Biophysics*, Annual Reviews: Palo Alto, 2008; Vol. 37, pp 375-397.

4. Ellis, R. J., "Macromolecular crowding: obvious but underappreciated". *Trends in Biochemical Sciences* **2001,** *26* (10), 597-604.

5. Minton, A. P., "How can biochemical reactions within cells differ from those in test tubes?". *Journal of Cell Science* **2006,** *119* (14), 2863-2869.

6. King, J. T.; Kubarych, K. J., "Site-Specific Coupling of Hydration Water and Protein Flexibility Studied in Solution with Ultrafast 2D-IR Spectroscopy". *Journal of the American Chemical Society* **2012,** *134* (45), 18705-18712.

7. King, J. T.; Ross, M. R.; Kubarych, K. J., "Water-Assisted Vibrational Relaxation of a Metal Carbonyl Complex Studied with Ultrafast 2D-IR". *J. Phys. Chem. B* **2012,** *116* (12), 3754-3759.

8. Khalil, M.; Demirdoven, N.; Tokmakoff, A., "Coherent 2D IR spectroscopy: Molecular structure and dynamics in solution". *Journal of Physical Chemistry A* **2003,** *107* (27), 5258-5279.

9. Kumar, S. K. K.; Tamimi, A.; Fayer, M. D., "Comparisons of 2D IR measured spectral diffusion in rotating frames using pulse shaping and in the stationary frame using the standard method". *Journal of Chemical Physics* **2012,** *137* (18).

10. King, J. T.; Anna, J. M.; Kubarych, K. J., "Solvent-hindered intramolecular vibrational redistribution". *Physical Chemistry Chemical Physics* **2011,** *13* (13), 5579-5583.

11. Anna, J. M.; Kubarych, K. J., "Watching solvent friction impede ultrafast barrier crossings: A direct test of Kramers theory". *Journal of Chemical Physics* **2010,** *133* (17).

12. Donoho, D. L., "Compressed sensing". *Ieee Transactions on Information Theory* **2006,** *52* (4).

13. Ori Katz, J. M. L., and Yaron Silberberg, "Compressive Fourier Transform Spectroscopy". **2011**.

14. Park, S.; Fayer, M. D., "Hydrogen bond dynamics in aqueous NaBr solutions". *Proc. Natl. Acad. Sci. U. S. A.* **2007,** *104* (43), 16731-16738.

15. Eaves, J. D.; Loparo, J. J.; Fecko, C. J.; Roberts, S. T.; Tokmakoff, A.; Geissler, P. L., "Hydrogen bonds in liquid water are broken only fleetingly". *Proc. Natl. Acad. Sci. U. S. A.* **2005,** *102* (37), 13019-13022.

16. Nicodemus, R. A.; Ramasesha, K.; Roberts, S. T.; Tokmakoff, A., "Hydrogen Bond Rearrangements in Water Probed with Temperature-Dependent 2D IR". *The Journal of Physical Chemistry Letters* **2010,** *1* (7), 1068-1072.

17. Lingwood, D.; Simons, K., "Lipid Rafts As a Membrane-Organizing Principle". *Science* **2010,** *327* (5961), 46-50.